Physical basis of morphogenesis : Coupling between mechanics and growth of plants and yeast

Jean-Daniel Julien

THÈSE

en vue de l'obtention du grade de

Docteur de l'Université de Lyon, délivré par l'École Normale Supérieure de Lyon

Discipline: **Physique**

Laboratoire de Physique

Laboratoire Reproduction et Développement des plantes

Laboratoire Joliot-Curie

École Doctorale Physique et Astrophysique de Lyon (PHAST)

présentée et soutenue publiquement le 18/12/2015

par Monsieur Jean-Daniel JULIEN

Bases physiques de la morphogenèse: Couplage entre mécanique et croissance des plantes et de la levure

---

Directeur de thèse : M. Arezki BOUDAOUD

Après l'avis de :

M. Yoël FORTERRE

M. Raphaël VOITURIEZ

Devant le jury composé de :

Mme Karen ALIM, MPI DSO, Invitée

M. Arezki BOUAOUD, RDP, Directeur

M. Yoël FORTERRE, IUSTI, Rapporteur

M. Michel LABOUESSE, IGBMC, Membre

M. Jacques PROST, Institut Curie, Président

M. Alain PUMIR, Laboratoire de Physique, Co-encadrant

M. Raphaël VOITURIEZ, LPTMC, Rapporteur

Acknowledgements

First I would like to thank Arezki Boudaoud for his support during these three years. He is a brilliant researcher and a fantastic person, and I was really fortunate to have such an awesome director.

I thank Alain Pumir, my co-supervisor, for his advice and for introducing me to biophysics. With such another talented scientist and a nice person, I was twice as lucky.

I thank the collaborators I worked with: Daria Bonazzi and Nicolas Minc for the work on spores, and Marion Louveaux and Olivier Hamant for the work on cell divisions. Those projects were fascinating and I enjoyed the interplay between experimental and computational approaches.

I thank the members of the committee for evaluating my work: the president Jacques Prost, the reviewers Yoël Forterre and Raphaël Voituriez, the examiner Michel Labouesse, and our guest Karen Alim.

I thank all the people in the team Biophysics and Development. The past three years would not have been so enjoyable without a friendly atmosphere and so many interesting discussions.

More generally I thank all the people I interacted with in my three laboratories. The list would be quite long, so just thank you everybody!

Many thanks must go to the staff of those labs for taking care of us so efficiently.

I thank all the friends from the ENS. This list would also be long, but they will recognize themselves. Thank you guys for making the ENS my “second house”. Studying and working here have truly changed my life.

I also thank the friends outside of the ENS, particularly my former flatmates, with whom I had (and still have) so much fun, and my “childhood buddies”, still close after all these years.

I thank my family for their support and for making me eager to reach this level.

Finally I thank my girlfriend Alix. I love you!

Bases physiques de la morphogenèse:
Couplage entre mécanique et croissance
des plantes et de la levure

Mots-clés: morphogenèse, mécanique, croissance, biochimie, levure, plante, phyllotaxie, division

Résumé

"Comment se fait-il que l'on comprenne tellement moins la manière donc les cellules se façonnent que leur métabolisme et leur génétique?"

Franklin M. Harold

Les scientifiques sont depuis toujours fascinés par la multitude des formes observées dans la nature. En 1917, D'Arcy Thompson reconnaissait déjà l'importance de la mécanique lorsqu'il montra que de nombreuses formes adoptées par les systèmes biologiques étaient comparables aux formes générées par la tension de surface dans un fluide sous certaines contraintes géométriques [9]. De même, Turing lui-même, dans son célèbre article sur l'établissement de motifs biochimiques, soulignait l'importance de "l'interdépendance des données chimiques et mécaniques". Il décida néanmoins de se focaliser sur les systèmes où les aspects mécaniques pouvaient être ignorer [10].
Au milieu du 20ième siècle, le rapide développement de la génétique a mené à

une description détaillée de la biochimie du développement. Par conséquent, malgré le fait que le rôle important de la mécanique ait été reconnu très tôt, la morphogénèse est apparue comme régulée essentiellement par les processus biochimiques [4].

Mais bien que la forme d'un organisme repose en effet sur des interactions biochimiques complexes, celles-ci sont insuffisantes pour passer de l'information génétique à la forme. Les différentes parties d'un organisme interagissent mécaniquement et le contrôle de leur croissance et de leur changement de forme implique nécessairement des contraintes mécaniques. L'amélioration des techniques d'imagerie et de calcul a favorisé un regain d'intérêt pour la mécanique, avec des pionniers comme Paul B. Green, qui souligna que les cellules de plantes contrôlent leur forme par le renforcement anisotrope de leur paroi par la cellulose [1].

Les cellules à parois, telles que les plantes et les levures, sont particulièrement adaptées à l'étude de la mécanique de la morphogénèse. En effet, les forces générées par leur rigidité et leur très grande pression interne sont plusieurs ordres de grandeurs plus grandes que les forces observées dans les tissus animaux. Dans ces cellules, la croissance correspond à la déformation plastique de la paroi cellulaire sous l'effet de la tension mécanique résultante de la pression [6, 7]. La pression étant isotrope, les propriétés mécaniques de la paroi cellulaire doivent être régulées spatialement afin de déclencher la brisure de symétrie et de générer des formes anisotropes. Plus précisément, la création de formes dans ces organismes repose sur les concepts d'hétérogénéité et d'anisotropie mécanique. Comme l'écrit Franklin M. Harold en 1990, "les formes de nombreuses cellules à paroi peuvent être comprises comme [...] une flexibilité localisée avec une force globale" [3].

À présent, il est clair que le rôle de la mécanique ne se limite pas à l'orientation passive de la croissance par l'intermédiaire des propriétés des matériaux. Pour reprendre l'exemple de la cellulose, son orientation guide en effet la croissance, mais la croissance à son tour rétro-agit sur son orientation: les microtubules se réorientent le long de la contrainte maximale, puis contrôlent la déposition d'une nouvelle couche de cellulose dans cette direction [2, 5]. Ce mécanisme peut réinforcer une anisotropie pré-existante dans la paroi, ou la générer *de novo*, comme par exemple dans l'hypocotyle de *Arabidopsis* où il a été démontré récemment que la brisure de symétrie est déclenchée par le ramollissement des parois cellulaires longitudinales, ce qui a pour effet d'augmenter la contrainte transverse et d'orienter la déposition de cellulose auparavant aléatoire [8].

Le travail présenté ici est l'aboutissement de trois différents projets sur le couplage entre la mécanique et la croissance. Le premier chapitre est une revue concernant la mécanique et l'élongation des cellules à parois, où l'accent est placé sur les travaux numériques. Le deuxième chapitre présente quelques modèles de la mécanique du développement avec plus de détails techniques. Le troisième chapitre est une étude de l'établissement et de la stabilisation de la polarité chez les spores de la levure à fission, un phénomène qui repose sur un couplage entre mécanique, polarité, et croissance. Le quatrième chapitre est une étude numérique d'un modèle chimio-mécanique de phyllotaxie chez les plantes. Les motifs d'hormone de croissance sont créés par l'intermédiaire d'une rétro-action entre la mécanique des cellules et le transport polaire de cette hormone. Nous nous sommes demandé si le champ à l'origine de la rétro-action est la déformation ou la contrainte, une question ignorée dans la plupart des travaux sur le couplage entre mécanique et biochimie. Le

cinquième chapitre concerne aussi un couplage entre polarité et mécanique. Nous étudions la manière dont la contrainte générée par la croissance ou la courbure des tissus peut se substituer aux indications géométriques qui orientent les divisions cellulaires à l'apex de la tige.

Références

[1] Paul B. Green. Mechanism for plant cellular morphogenesis. *Science*, 138(3548):1404–1405, 1962.

[2] Olivier Hamant, Marcus G. Heisler, Henrik Jönsson, Pawel Krupinski, Magalie Uyttewaal, Plamen Bokov, Francis Corson, Patrik Sahlin, Arezki Boudaoud, Elliot M. Meyerowitz, and others. Developmental patterning by mechanical signals in Arabidopsis. *science*, 322(5908):1650–1655, 2008.

[3] Franklin M. Harold. To shape a cell: an inquiry into the causes of morphogenesis of microorganisms. *Microbiological Reviews*, 54(4):381–431, 1990.

[4] U. Henning. Determination of cell shape in bacteria. *Annual Reviews in Microbiology*, 29(1):45–60, 1975.

[5] Benoît Landrein and Olivier Hamant. How mechanical stress controls microtubule behavior and morphogenesis in plants: history, experiments and revisited theories. *The Plant Journal*, 75(2):324–338, July 2013.

[6] J. A. Lockhart. An analysis of irreversible plant cell elongation. *Journal of Theoretical Biology*, (8):264–275, 1965.

[7] Joseph K.E. Ortega. governing equations for plant cell growth. *Physiologia Plantarum*, 79:116–121, 1990.

[8] Alexis Peaucelle, Raymond Wightman, and Herman Höfte. The Control of Growth Symmetry Breaking in the Arabidopsis Hypocotyl. *Current Biology*, 25(13):1746–1752, June 2015.

[9] D'Arcy Thompson. *On Growth and Form*. 2nd edition, 1942.

[10] Alan Mathison Turing. The chemical basis of morphogenesis. *Philosophical Transactions of the Royal Society of London B: Biological Sciences*, 237(641):37–72, 1952.

Physical basis of morphogenesis:
Coupling between mechanics and growth
of plants and yeast

Key-words: morphogenesis, mechanics, growth, biochemistry, yeast, plant, phyllotaxis, division

Summary

"Why is it that we understand so much less about the manner in which cells shape themselves than we do of their metabolism or genetics?"

Franklin M. Harold

The diversity of forms observed in biological systems have fascinated scientists for a long time. In 1917, D'Arcy Thompson already recognized the importance of mechanics by showing that many shapes observed in biological systems are similar to the shapes generated by surface tension in a fluid possessing some geometrical constraints [9]. Similarly, Turing himself, in his famous work on chemical patterning, recognized the importance of "the interdependence of the chemical and mechanical data". Nevertheless he chose to focus on systems where the mechanical aspects could be ignored [10].
But despite the fundamental role of mechanics being acknowledged for so long, the middle of the 20th century, with the rapid development of biochemistry and the subsequent knowledge of the molecular actors of development

in great details, led to the a view of morphogenesis driven mostly by biochemical processes [4].

But although the shape of an organism does rely on complex biochemical interactions, they are not sufficient to understand the translation of the genetic information into shape. The different part of an organism interact mechanically and the control of their growth and shape changes necessarily involves mechanical constraints. With the improvement of imaging and computational tools, the interest for mechanics grew back, carried by pioneers such as Paul B. Green, who pointed out the role of the anisotropic reinforcement of plant cell wall by cellulose in order to control cell form [1].

Walled cells, such as plants and yeasts, are particularly well suited to study the mechanics of morphogenesis, since their stiffness and huge internal pressure generate forces, which are larger than the forces involved in animal tissues by several orders of magnitude. In these cells, growth corresponds to the yielding of the cell wall under to the tension generated by the internal pressure [6, 7]. Pressure being isotropic, the mechanical properties of the cell wall needs to be spatially regulated in order to break the symmetry and generate anisotropic shapes. More precisely, the formation of shapes in these organisms relies on mechanical heterogeneities and anisotropies. As Franklin M. Harold wrote in 1990, “the forms of many walled cells can be understood as [...] localized compliance with global force” [3].

Since then, it has become clear the role of mechanics is not just to passively orient growth via the properties of the material. To take the aforementioned example of cellulose, its orientation does guide growth, but growth in turn feeds back on orientation: the microtubules reorient along the direction of maximal mechanical stress, then control the deposition of new cellulose in the

same direction [2, 5]. This mechanism can reinforce a pre-existing anisotropy in the cell wall properties, or generate it *de novo*, for instance in the *Arabidopsis* hypocotyl where growth symmetry breaking has been recently showed to be triggered by the softening of the longitudinal cell walls that in turn increase transverse stress and switch from isotropic to anisotropic cellulose orientation [8].

The work presented here is the result of three different projects about the coupling of mechanics and growth. The first chapter is a review about mechanics and elongation of walled cells, focused on the computational studies. The second chapter presents some models of the mechanics of development with more technical details. The third chapter is a study of the establishment and stabilization of polarity in fission yeast spores, a phenomenon that relies on a coupling between mechanics, polarity, and growth. The fourth chapter is the computational study of a chemomechanical model of plant phyllotaxis. Patterns of growth hormone are achieved thanks to a feedback with cell mechanics and polar transport. We focused our attention on the question of stress- or strain-sensing, ignored in most other studies of the interaction between biochemistry and mechanics. The fifth chapter is also about a coupling between polarity and mechanics. We investigate how the mechanical stress generated by growth or curvature of the tissues can override the geometrical cues to orient the cell divisions in the shoot apical meristem.

References

[1] Paul B. Green. Mechanism for plant cellular morphogenesis. *Science*, 138(3548):1404–1405, 1962.

[2] Olivier Hamant, Marcus G. Heisler, Henrik Jönsson, Pawel Krupinski, Magalie Uyttewaal, Plamen Bokov, Francis Corson, Patrik Sahlin, Arezki Boudaoud, Elliot M. Meyerowitz, and others. Developmental patterning by mechanical signals in Arabidopsis. *science*, 322(5908):1650–1655, 2008.

[3] Franklin M. Harold. To shape a cell: an inquiry into the causes of morphogenesis of microorganisms. *Microbiological Reviews*, 54(4):381–431, 1990.

[4] U. Henning. Determination of cell shape in bacteria. *Annual Reviews in Microbiology*, 29(1):45–60, 1975.

[5] Benoît Landrein and Olivier Hamant. How mechanical stress controls microtubule behavior and morphogenesis in plants: history, experiments and revisited theories. *The Plant Journal*, 75(2):324–338, July 2013.

[6] J. A. Lockhart. An analysis of irreversible plant cell elongation. *Journal of Theoretical Biology*, (8):264–275, 1965.

[7] Joseph K.E. Ortega. governing equations for plant cell growth. *Physiologia Plantarum*, 79:116–121, 1990.

[8] Alexis Peaucelle, Raymond Wightman, and Herman Höfte. The Control of Growth Symmetry Breaking in the Arabidopsis Hypocotyl. *Current Biology*, 25(13):1746–1752, June 2015.

[9] D'Arcy Thompson. *On Growth and Form*. 2nd edition, 1942.

[10] Alan Mathison Turing. The chemical basis of morphogenesis. *Philosophical Transactions of the Royal Society of London B: Biological Sciences*, 237(641):37–72, 1952.

Contents

Chapter 1

Modeling the interplay between growth and mechanics in elongated walled cells

1.1 Summary

Symmetry breaking is a fundamental step of morphogenesis. All organisms have to be shaped from an isotropic cell or tissue, and the generation of elongated structures is a common feature across all the kingdoms. Mechanics is necessarily involved in the emergence of such structures, especially in walled cells, on which this review is focused. We show that bacteria, fungi and plants rely on two strategies to create rod-shape: tip-growth and diffuse anisotropic growth. In the first case, the softening of the cell wall and the deposition of new material is localized at the tip. In the second case, growth is not spatially restricted, but it is oriented by an anisotropic material allowing the elongation in only one direction. We present how these organisms regulate the mechanics of their wall to achieve these two modes of growth. Then we show that elaborate feedbacks involving curvature, growth or forces stabilize the cell elongation.

I wrote the review with some input from Arezki.

1.2 Paper

Modeling the interplay between growth and mechanics in elongated walled cells

Jean-Daniel Julien[1,2,3] and Arezki Boudaoud[1,2]

[1]Laboratoire Joliot-Curie, [2]Laboratoire Reproduction et Développement des Plantes, and [3]Laboratoire de Physique, ENS Lyon, 46 allée d'Italie, Lyon Cedex 07, France

Abstract

The generation of anisotropic shapes participates in the morphogenesis of almost all organisms. With the recent renewal of the interest for the mechanical aspects of development, it has become clear that mechanics contribute to this issue in a subtle interaction with various chemical actors. Here, we focus on plants, fungi, and bacteria, and we look at the mechanisms by which elongated cells are generated. We review how the interplay between growth and mechanics in their morphogenesis has been modeled.

1.3 Introduction

Symmetry breaking is a fascinating feature of the development of all living organisms. It is observed in contexts such as the directional growth of single cells [6] or the branching of multicellular organisms [46].

Here we focus on walled cells: plants, fungi, and bacteria. In these cells, the osmotic pressure, resulting from the concentration of solutes in the cytosol, drives growth and has to be counterbalanced by a rigid shell that prevents their burst [33]. This cell wall is also fundamental in determining the shape of the cell, as it is proven by the consequences that its disruption has on the morphology of those cells. Although for these different organisms they are not composed of the same polymers [45, 18, 55], they have common mechanical properties and their mechanics are regulated to facilitate the shaping of the cells. In particular, pressure being a global and isotropic force, mechanical or biochemical heterogeneities and anisotropies are fundamental to establish and maintain asymmetric shapes.

For this reason, we present in this review the links between mechanics and growth of elongated cells. We focus our discussion on computational modeling, which is a powerful tool to validate hypotheses by setting aside all but the fundamental actors of the studied phenomena and to pave the way for the future experimental effort.

1.4 Systems of interest

Rod-shaped bacteria. All kinds of shapes are found amongst bacteria and shape have long been an important criterion for their classification [12]. It

has been shown to be fundamental for many bacterial functions [63, 56, 15]. The rod is a very common shape, Escherichia Coli being probably the most famous example, and thus bacteria are perfect systems to study the establishment of elongated shapes.

The bacterial cell wall is made of peptides and glycans, with an additional layer of lipopolysaccharide in the case of Gram-negative bacteria [11, 55]. The glycan strands are oriented circumferentially and give to the bacteria cell wall anisotropic mechanical properties [15]. A detailed model of the outer wall, where the peptidoglycan network is simulated like a network of spring [38], is able to reproduce several bacterial cell shapes, like curved, helical, snake-like, and lemon shapes. The different results are obtained by adding various defects in the network. Whereas this model does not take into account growth, it has been the starting point for more recent studies that go further into the understanding of cell shape in bacteria and that are discussed in the next section.

Fungal hyphae and yeasts. Among fungi, hyphae and yeasts are good examples of elongated cells. Hyphae are very long filamentous structures, collectively organized as the mycellium. They grow at their tip, and new cell walls can eventually be formed orthogonally to the tubular part to divide the hypha into several cells. Yeasts are unicellular fungus. In particular, the fission yeast *Schyzosaccharomyces pombe* has long been a perfect system for studying symmetry breaking and tip growth. Indeed, it is able to display a two-folds increase in length while maintaining a constant diameter.

The cell wall of fungi is made mostly of glucans, mannoproteins, and chitin [45]. Although some of those components are fibrous, because of their lack

of preferential orientation the fungal cell wall does not have anisotropic mechanical properties [15]. Despite its composition being well known, no model has tackled the question of its building.

Single cells in plants, pollen tubes and root hairs. Plants will provide two other systems to our study, the pollen tube and the root hairs. The pollen tube is a tubular protuberance formed from the pollen grain [24, 42]. In order to fertilize a flower, its growth is fast and highly directional. Root hairs are long tubular outgrowths from the epidermal cells of the root. They are important for the acquisition of nutrients and the anchorage of the plant [14, 28]. As most plant cells, their cell wall is made of cellulose microfibrils and hemicellulose embedded in a matrix of pectin [61]. Many different kind of cellulose organization are observed in single plant cells, ranging from the highly directional circumferential alignment to random orientations [18]. A preferential orientation of cellulose microfibrils can give anisotropic properties to the plant cell wall and therefore it is very important in the context of directional elongation. In pollen tubes and root hairs, cellulose usually displays a helical arrangement that could help resist bending forces and invade the external medium. It could also reinforce the transition region between the tip and the cylindrical part, which is known to bear the highest stress [24]. A model has been implemented, where the orientation of cellulose emerges from geometrical constraints. The condition of optimal packing of cellulose microfibrils restraints their direction and the movement of their synthesizing complexes along the axis of the cell can generate various kind of alignments [21, 48].

A multicellular case, the shoot apical meristem. Our last system of interest, which is multicellular, also comes from plants. The shoot apical meristem is the above-ground tip of the plant. It is the site of most of the organogenesis. The organs are initiated around the central zone and emerge as protuberances from the apical dome. Thus they are a good example of symmetry breaking on a multicellular scale. As for single cells, the deposition of cellulose microfibrils in a preferential direction can provide anisotropic mechanical properties to the meristem.

1.5 Generating elongated shapes

Using local growth. Although the systems described here seem very different, their strategy to make elongated cell is the same: growth is restricted to the tip. The importance of mechanics leaded to the development of several models describing tip-growth and not focusing on a particular organism. A general mechanical has been inspired from the inflating of rubber balloons [4]. The rubber balloons are modeled as elastic shells whose stiffness is heterogeneous. More precisely, the extensibility of the material is large on a small annular region around the tip and small on the cylindrical part of the shell. Such profile of stiffness is able to reproduce the observed deformation of some cells. Despite the system being very different from a living cell, this work highlights the importance of regulating the global force that is pressure with the local supply of the cell wall material or with the local modification of the cell wall properties. The spatial extent of the wall deposition, and more precisely how it depends on the size of the cell, has been proven theoretically to change the shape of the growing tip [13]. In this model, the cell is modeled

as a shell whose viscosity is finite only at the tip. Growth is compensated by material addition at this tip. The temporal evolution of the shape of the cell is studied depending on its size and of the extents of the material addition and of the viscosity. It is shown that the supply in new material has to verify precise scaling relations for the shape of growing tips to be independent of their size.

In hyphae, the delivery of new material is thought to be organized thanks to a structure called the vesicle supply center (VSC) and from which vesicles emanate randomly. The movement of the VSC in a preferential direction makes the delivery of new cell wall heterogeneous and leads to the emergence and growth of the tip. This phenomenon was first simulated in two dimensions with a linear displacement of the VSC that releases vesicles moving in any random direction. The movement of the VSC creates a self-similar tip once the proper distance from the cell wall is reached [2]. Later the model has been improved to make it more realistic. It has been adapted into 3D simulations to show that during its expansion, the cell wall moves orthogonally to its plan [25]. This result fits with the general idea that the driving force of tip growth is the internal pressure. A second improvement was to replace the ballistic motion of the vesicles by diffusion [58], which modifies slightly the shapes generated by the model. The mechanics of hyphal growth have been also investigated with the nonlinear elasticity theory of shells, thus allowing the computation of large deformations [26]. Importantly, an assumption of this model is that the tip of the hypha is softer than the cylindrical part. Growth is simulated by computing the deformation of the hypha due to turgor pressure then taking the deformed shape as a new initial shape that can be deformed further. So in this model growth appears to be local thanks to

this softening of the tip. More recently, the same model was used to study the effect of the friction between the growing tip and the external medium. This friction leads to a flattening of the tip that is consistent with experimental data [27]. The study of such effects emphasizes the evolution of the computational approaches to tackle more and more complex questions.

In yeasts, the local delivery of new cell wall is driven by microtubules and actin filaments. They can be necessary for growth, or just define the location where growth takes place. For instance, chemical treatments and mutants have proved that disruption of microtubules leads to major geometrical defects in the fission yeast [30]. Application of actin inhibitors can modify the timing of growth or completely arrest it depending on the concentrations involved. Consequently, the microtubules and actin filaments must efficiently target the cell tips [52, 57] to deliver the new material to the proper location, where the deformation is supposed to be plastic, that is irreversible. A model has showed that the tip of microtubules are used as landmarks by a diffusing growth signal to generate the shapes of fission yeasts [19]. In this work, microtubules are modeled as growing and shrinking flexible rods attached to the nucleus of the yeast. Simulations where the growth signal is directly linked to the likelihood of microtubule tip contact are not able to generate rods with a stable width. The model was improved with the assumption that microtubules control the deposition of landmark proteins that will in turn attract the growth signal. This model initiates the description of the molecular regulation of fission yeast cell shape.

In plant cells, root hairs and pollen tubes are quite similar to yeasts in the way they control their polar growth. Plant cells have two kind of microtubules: the cortical microtubules, which form a dense network just beneath

the plasma membrane and can be oriented in many different ways, and the endoplasmic microtubules, which are located in the cell cytoplasm similarly to what is observed in yeasts. As in yeast, endoplasmic microtubules and actin filaments are oriented toward the cell tip and are involved in its targeting during the supply of new material [54, 29, 17]. In root hairs, they are organized thanks to the nucleus [1]. Detailed measurements of the surface expansion of root hairs have proven that their growth takes place mostly in a ring just below the tip, on which it is isotropic. Farther from the tip, the expansion becomes mostly radial and vanishes [53]. A computational model is able to reproduce the strain and stress that is measured on several tip growing cells, amongst which root hairs [20]. This viscoplastic model is used to study the relationship between the shape of the tip and some mechanical properties such as its extensibility profile or its anisotropy. Growth is simulated via the yielding of the material when the stress reaches a threshold. In addition, the stretching of the material is compensated by a deposition that keeps its thickness constant. The main result is that the cell has to have anisotropic mechanical properties to display the same strains and stresses that are observed experimentally. More precisely, the material has to be transverse isotropic, meaning that its properties in its thickness are different from its properties in its tangent plane. Such anisotropy can be explained by the deposition of cellulose with a random orientation in the plane of the cell wall.

A similar softening is observed in the tip of pollen tubes [64, 35]. Their shapes are reproduced with an elastic model that includes the existence of a sharp gradient of stiffness at the tip [22]. In the simulations, growth is simply obtained by considering that the shape of the tube deformed by the turgor

pressure is its new undeformed shape, thus allowing further elongation. The best fitting of the shapes was achieved with an isotropic material. Interestingly, the gradient of stiffness used in the simulation is consistent with the gradients that are observed in the fluorescence of various cell wall components, such as pectin, cellulose, and callose, that are known to determine its mechanical properties.

The importance of local softening in plants morphogenesis is known also at the multicellular scale of the shoot apical meristem. Measurements of the stiffness of the cell wall proves that it decreases on the organs that emerge from the apical dome [47]. This softening is induced by the presence of the growth hormone auxin and is necessary to the emergence of the organ [10]. A model is able to reproduce, amongst other things, the shape of a meristem with its emerging organs [36]. A chemical patterning system of equations is implemented on a surface. Then growth is achieved by the normal movement of the surface according to the concentration of a growth catalyst. This work does not model the mechanics of the tissue but is able to generate complex shapes just thanks to various chemical patterns. More recently, efforts have been made to model the mechanics of multicellular tissues more realistically [7]. In the simulations, every cell wall is modeled as a surface with elastic, plastic and viscous properties. By tuning the stiffness and/or growth rate of the cells, the model is able to simulate the emergence of one or several organs around the meristem. To do so, it is necessary to finely tune the softening of the tissue where the organ will be located. This work shows how stiffness heterogeneities are able to generate complex shapes, and interestingly, several solutions are sometimes possible for creating a given shape. For this reason, the comparison of the computational outputs with the real tissues cannot be

limited to their shapes and more complex observations have to be made.

Using anisotropies. Several organisms use another mechanism to create cylindrical cells. Although growth is diffuse, it is made anisotropic thanks to the mechanical properties of the cell wall. Indeed, the stiffness of a material is not just a scalar number. The material can have different properties in different directions, that is being anisotropic, as for instance a fiber-reinforced medium that is harder to stretch in the direction of the fibers.
In rod-shaped bacteria, growth usually does not take place at the tips but on the cylindrical region [15]. The insertion of new material occurs on small patches on the cylindrical part of the cell, and is coordinated by MreB filaments. A study of the insertion of new material in the outer wall of Gram-negative bacteria has proven that this insertion does not need to be spatially coordinated in order to fit with experimental measurements [60]. More precisely, the outer wall of the bacteria is modeled like an incompressible viscous fluid, and the simulations assume that insertion events occur at a fixed rate, are randomly distributed in space, have an exponentially distributed duration, and lead to the addition of a fixed amount of material. These assumptions, which were chosen for simplicity, were sufficient to explain the observed growth patterns. Despite the growth being distributed on their cylindrical part, bacteria still grow as elongated cells because their walls are reinforces circumferentially, thus preventing radial growth. A model of this elongation by anisotropic reinforcement has been able to reproduced rod-like shapes, divisions and bulging of *E. coli* cells [40]. In this work the cells are modeled as a continuous material whose growth is driven by the minimization of a mechanochemical energy. Growth occurs on a temporal scale much

larger that the scale involving MreB movement, thus the mechanical effect of helical MreB filaments is averaged and modeled as a radial force resisting turgor pressure. Without this force, *E. coli* cells grow spherically. In addition this work shows that the disappearance of MreB filaments is necessary both for divisions and reproduction of bulging shapes.

A more detailed model of the outer wall, where the peptidoglycan network is simulated like a network of spring, is able to reproduce several bacterial cell shapes, like curved, helical, snake-like, and lemon shapes [38]. The various results are obtained by adding defects in the network, such as removal, substitution or relaxation of springs. A second work is based on the same model and take also growth into account as the insertion of new peptidoglycan strands into the network [23]. The mechanical anisotropy of the cell wall is maintained by the circumferential orientation of the glycan strands, which are much stiffer than the longitudinal peptide crosslinks. Then this work goes further by challenging a role of mechanical forces and cell wall density in the regulation of bacterial shape. The result is that the probability to insert a new strand to the network has to be independent of the local density of peptide crosslinks. Otherwise, the insertion of new strands leads to a local increase of this density, that will in turn increase the probability of insertion. This positive feedback loop is unable to generate robust rod-like shapes. An attempt to bias the insertion of new wall towards region of high mechanical stress generates the same kind of feedback loop, thus showing that only the simplest hypothesis of uniform insertion is able to generate shape-preserving growth. Moreover, it shows that the condition of uniform insertion can be verified if it occurs on a fixed helical pattern that could be created by a MreB helix.

In the multicellular context of the shoot apex, the strategy of local softening discussed above is combined with stiffness anisotropy. Thanks to their ability to orient the deposition of cellulose, the plant cell wall can be very anisotropic. This is the case on the boundary between an emerging organ and the meristem[31]. Such mechanical properties provide an additional mechanism for the directional growth of an organ. The model discussed earlier also includes mechanical anisotropy to reach a greater agreement with the simulations [7]. Interestingly, the optimal mechanical properties are not the intuitive ones. For instance, the lower part of the flower bud grows faster, so that the flower grows upward. This observation leads to the first hypothesis that its stiffness has to be reduced. Nevertheless, for the best agreement, it is necessary to include its anisotropic stiffening compared with the rest of the flower bud. Additionally, the different regions that were defined, and on which the mechanical properties are tuned, are inspired by the patterns of expression of some genes. Finally, this study paves the way for a better understanding of genetic regulation of the mechanical properties of the tissue.

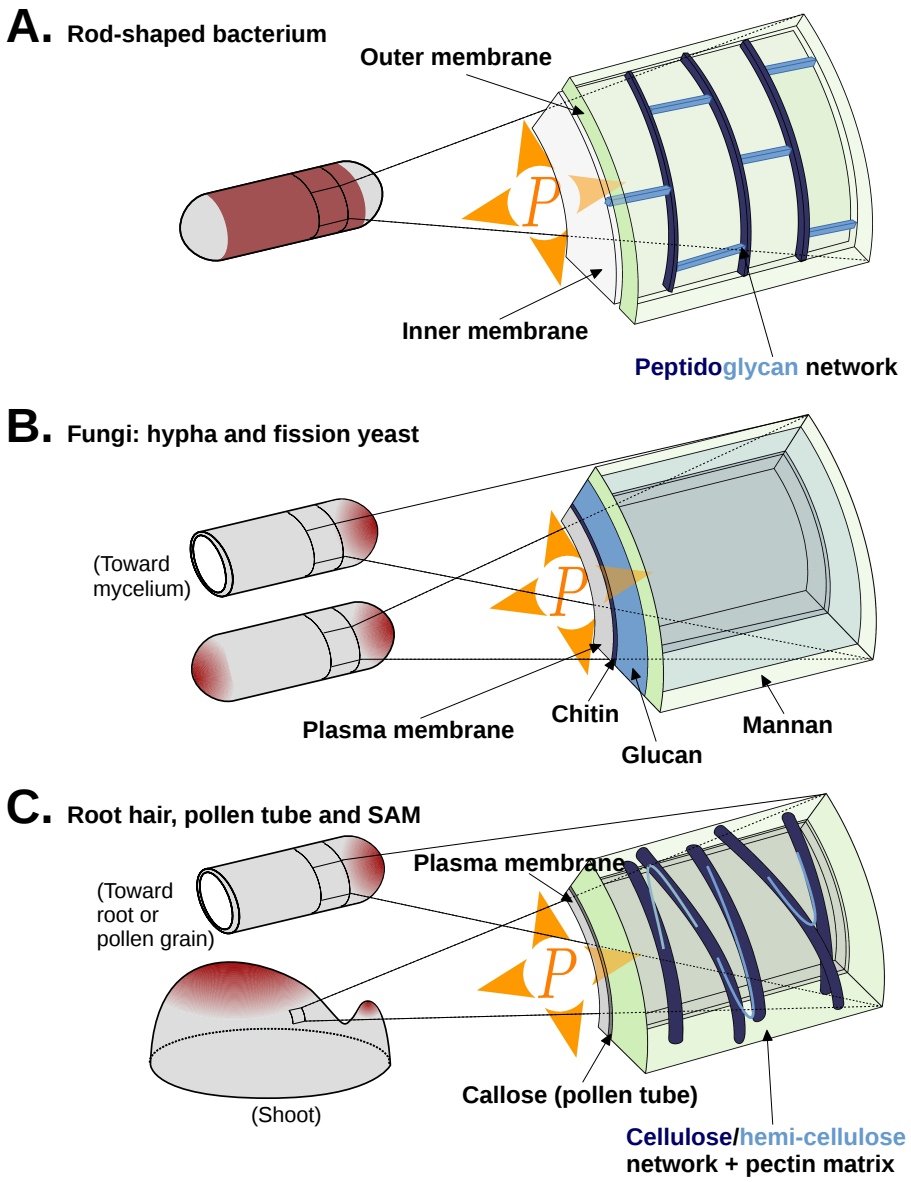

Figure 1.1: **Systems of interest: growth mode and composition of the cell wall.** (A) In many rod-shaped bacteria, such as *E. Coli*, growth is diffuse, localized on the whole cylindrical part on the cell. The cell wall of *E. Coli* and others gram-negative bacteria is composed of a stiff layer of peptides and glycans surrounded by two lipid membranes [55, 15]. (B) Tip growth is observed in fungal hyphae and fission yeasts. Over the plasma membrane are found three layers, made respectively of chitin, glucan and mannan [45, 8]. (C) In plants, pollen tubes and root hairs are tip-growing cells. On a larger scale, growth has to be focused on the tip of emerging organs around the shoot apical meristem. The plant cell wall is made a network of cellulose and hemi-cellulose embedded in a matrix of pectin [18]. An additional layer of callose can be found in the pollen tubes [16]. In the three systems the relative quantities of the different components can vary, for instance between species or even inside a single cell depending on the precise part of the cell.

1.6 Feedbacks that stabilize elongated shapes

Sensing curvature. A recent geometrical model, where material deposition and curvature are coupled, has successfully reproduced the cell shapes of several organisms [39]. In this model, the spatial extent of the deposition is not intrinsically restricted. Deposition is directly assumed to be an increasing function of the curvature. Thus local growth is a result of this feedback and a consequence of the pre-established shape of the cell.

There is evidence for the existence of such a feedback in bacteria. In the previous section, we mentioned the modeling of the bacterial as a network of springs mimicking the peptidoglycans [38] and able to grow via the insertion of new strands in the network [23]. A second work based on this model, shows that the role of MreB is not limited to the orientation of growth by mechanical reinforcement [59]. The spatial and temporal correlation of growth and MreB localization indicates that MreB directly controls the location of the previously mentioned bursts of growth on the cylindrical part of the cell. This results is confirmed by the disruption of growth heterogeneity upon depolymerization of MreB. Additionally this work suggests the existence of a feedback between the curvature of the cell wall and growth distribution. Indeed, simulations where the insertion of material is biased toward the regions of negative curvature are able not only to maintain a cylindrical shape but also to recover from a initial bended shape. Thus, sensing curvature is a way to stabilize the shape of the cell and even to restore it after some disruptions. Recent observations of the preferential localization of MreB in regions of negative curvature confirm the existence of this feedback mechanism [5].

Sensing forces In fission yeasts, a recent work have showed that the transition from unstable to stable polarity is triggered mechanically by the breaking of the protective shell of the spore [6]. Interestingly, the ratio between the volume at the transition and the initial volume of the spore is constant, despite the initial sizes of the spore being quite different. Simulations leads to the same result, assuming that the transition coincides with the breaking of the shell. The outer wall is modeled as an elastic stiff shell. The inside of the spore is also elastic and the supply in new material is modeled by giving plastic properties to the spore. Growth takes place on a patch moving randomly, mimicking the displacement of the polarity proteins that is observed experimentally. When it is intact, the outer shell prevents the outgrowth and keeps the spore roughly spherical. The tension stored in the shell increases, up to a threshold over which its rupture initiates the polar growth. Thanks to this mechanism of stress-sensing via mechanical breaking, the spore starts its outgrowth with a precise increase in its volume.

We mentioned in the previous sections that the morphogenesis of the shoot apical meristem relies both on local softening and mechanical anisotropies. The two mechanisms are tuned thanks to a feedback from mechanics. Indeed, the local softening that triggers the emergence of the organs is achieved by the increase in the concentration of the growth hormone auxin. It is well known that the patterns of auxin are generated thanks to its feedback with its transporters, the PIN1 protein: by pumping the auxin towards the cells having a higher concentration, PIN1 reinforces auxin heterogeneities. This so-called “up the gradient” model has been well studied [41] and recent experimental evidence suggests that the transporters indirectly “measure” the auxin concentrations via the mechanics of the cell walls [34, 49, 10]. More

precisely, they are preferentially inserted in the walls that are more mechanically stressed. A local increase of auxin concentration leads to softening of the cell. The neighboring cells, having to compensate for the weakness of the soft cell, are locally more stressed and therefore orient their transporters toward it. This chemomechanical model has been implemented using the finite elements method for the mechanics coupled with a system of differential equation for the auxin dynamics [34]. It is able to generate some patterns of auxin and to reproduce the radial PIN1 reorientation observed around a cell ablation.

In many tissues, particularly in the meristem, mechanics also regulate the orientation of cellulose microfibrils. Indeed, cellulose and microtubules are often observed to be aligned. It has led to the hypothesis that microtubules could also control the deposition of cellulose, and not only geometry [3]. Additionally, microtubules are known to orient along the direction of maximal mechanical tension. Consequently, the preferential orientation of cellulose microfibrils reinforces the material in the direction of mechanical stress, thus increasing the stress anisotropy and stabilizing the microtubules [43]. Several computational model simulated this feedback loop between mechanical stress and anisotropy. In a first work [31], the meristem is modeled as 3-dimensionnal elastic surface, thus limited to the first layer of cells. The mechanics is computed thanks to a vertex model, meaning that the cell walls are mimicked by 1-dimensionnal springs. The stiffnesses of these springs increases as their angle with the local stress decreases, thus mimicking the orientation of the microtubules and their feedback on the mechanical properties of the tissue. Growth is driven by the turgor pressure coming from the internal tissue. Above a stress threshold, the cell walls yield and thus deform

plastically. By initiating the emergence of an organ via the local softening of a group of cells, the cellulose reorientation leads to a circumferential pattern around the organ, reinforcing the boundary with the apical dome and thus making the symmetry breaking more effective. Another model leads to similar results using two other methods to compute the mechanics of the tissue [9]. The paper first shows the results from simulations based on the finite element method, then the results relying on triangular biquadratic spring, a more recent technique, simpler even though less general.

Sensing growth rate. In fission yeasts, an additional result from the mechanical model discussed above is that a positive feedback between growth and polarity can explain the polarity stabilization during spore germination and outgrowth [6]. The first assumption that the displacement of the polarisome is random can be replace by a motion toward the location of maximal surface expansion of the spore. Feedback based on curvature or mechanical stress were tested, but the growth-based was the only one able to generate cylindrical shapes. Future effort should unravel the precise biochemical regulation of this feedback, which is still unclear.

A model coupling the deposition of new material and the mechanics of the cell wall has reproduced the morphologies of pollen tubes and is able to explain the growth oscillations that are observed in the rapidly growing tubes [51]. In this model, the rate of deposition of wall material decreased with the speed of elongation of the cell. Consequently, the cell oscillates between phases of high deposition and slow elongation and phases of low deposition and fast elongation. Depending on the strength of the negative feedback, this simple mechanism can lead both to oscillatory or steady growth and gener-

ate smooth or pearled pollen shapes. This negative feedback could come from the cell wall stretching that activates the entrance of cytosolic calcium that itself downregulates the polymerization of the actin cytoskeleton and thus slow down the delivery of vesicles [62].

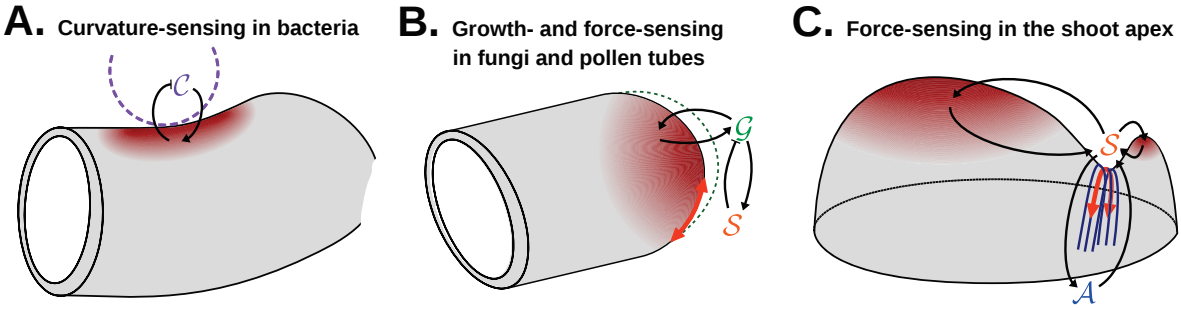

Figure 1.2: **Feedbacks that stabilize elongation.** (A) In *E. Coli*, the insertion of new cell wall is increased on the region of negative curvature. Thanks to this feedback the rod shape is stabilized and can even be recovered from initially curved shapes [59, 5]. (B) In pollen tubes and fission yeasts, surface expansion at the tip is coupled with the mechanics of the cell wall. In Pollen tubes this feedback leads to oscillatory tip growth [51] whereas in fission yeast it is coupled with a positive feedback between surface expansion and polarity proteins position. It prevents this feedback to stabilize the growth axis and leads to the random movement of the polarity proteins cluster in the spore. After the breaking of the outer spore wall, the positive feedback can take place and promotes tip-growth [6]. (C) In the plant shoot apex, two loops involving mechanics are coupled. Through the enhancement of growth hormone transport, mechanical stress focus growth at the tip of the organ. It also increase the mechanical anisotropy of the cell wall via the deposition of cellulose oriented by stress-sensing microtubules. Then both growth heterogeneity and mechanical anisotropy feedback on stress [31, 34].

1.7 Conclusion

The generation of anisotropic shapes in walled cells relies mainly on two strategies. Many cells, such as hyphae, yeasts, root hairs or pollen tubes grow directionally via the supply of new material to the cell wall on a precise

and restricted location [58, 19]. Various models for this local growth have been implemented and are able to reproduce most of the shapes that are observed. These computational approaches can give some information about the mechanics of the cell wall [20, 22] or about its behavior with respect to certain perturbations [27]. Rod-shapes bacteria use a very different strategy, based on the mechanical reinforcement of their lateral part, whose growth has to be restricted to maintain their shapes. This reinforcement is achieved thanks to the circumferential alignment of the glycan strands on the cell wall, deposited along the curved filaments of the MreB protein [38, 23]. On a multicellular scale, plants combine those two approaches to initiate the growth of their organs. Simulations have proven that both mechanisms are necessary to induce the massive shape change required for organogenesis. The major actors of this mechanical control of morphogenesis, each corresponding to one of the strategies discussed here, is the hormone auxin, whose is involved in the softening of the plant cell wall [50], and cellulose, a stiff polymer whose oriented deposition leads to stiffness anisotropy [3].

Several feedbacks have been identified that regulate growth. Bacteria, thanks to a simple mechanism of curvature-sensing based on the MreB protein, are able to maintain and even to generate *de novo* cylindrical shapes [5, 59]. It is remarkable that this feedback provides such an impressive robustness with respect to massive perturbations of the shape and mechanics of the cells. In fission yeast, a precise volume doubling between the germination and the outgrowth is granted by the mechanical breaking of its protective shell [6]. The role of this mechanism of force-sensing is unclear but could be to provide some kind of robust timer for the exit of the protective shell or to regulate the size of the spore at the outgrowth. Force-sensing is also involved in the

organogenesis in the plant shoot apex. Mechanical stress, auxin softening and cellulose anisotropy feedback each other in a complex loop necessary for the generation of precise shapes [31, 34]. Finally, growth-sensing explains both the random movement and the stabilization of polarity before and after the triggering of the outgrowth in fission yeast [6]. Indeed, before the outgrowth, the outer spore wall mechanically inhibits growth and its aforementioned breaking acts like a switch on the growth feedback and consequently on the transition from unstable to stable polarity. Growth-sensing is also relevant for the oscillatory growth in pollen tubes [51]. All these studies show the efficiency of computational approaches to unravel the complex feedbacks that now appear to drive the growth of all organisms and to explain the remarkable robustness of developmental processes. Simulations allow to test alternative hypotheses that can be difficult to differentiate experimentally. They can predict experiments likely to lead to shed light on the relevant actors.

The molecular actors behind many of these feedbacks are unknown. Curvature-sensing in bacteria could be due to a curvature-dependent binding energy of the targeting machinery MreB. Negative curvature and MreB localization could also be driven by a common signal such as proteins involved in cell wall synthesis [5]. In fission yeasts, mechanisms similar to the oscillatory growth of pollen tubes could explain the stabilization of polarity by surface expansion [62, 51]. Alternatively, polarity could be diluted and destabilized in the absence of sufficient growth [44]. The outer spore wall could also restrict the space for new material deposition. Finally, growth could be involved in the monitoring of cellular dimensions by intracellular gradient [37]. Identifying the actors behind mechanosensing at the shoot apex is still a chal-

lenging questions, both for the orientation of microtubules and the insertion of auxin transporters. Stretching of the cell membrane could activate some ion channels or modify the conformation of some protein, thus leading to the activation or relocation of some biochemical factors that would impact on microtubules or PIN1 proteins [43]. In the case of auxin transporters, another hypothesis is the activation of exocytosis and inhibition of endocytosis by the tension in the cell membrane [32]. All these hypotheses lack evidence, but new insights can be expected with the improvement of the techniques of cellular and developmental biology.

References

[1] C. Ambrose and G. O. Wasteneys. Microtubule Initiation from the Nuclear Surface Controls Cortical Microtubule Growth Polarity and Orientation in Arabidopsis thaliana. *Plant and Cell Physiology*, 55(9):1636–1645, September 2014.

[2] S. Bartnicki-Garcia, F. Hergert, and G. Gierz. Computer simulation of fungal morphogenesis and the mathematical basis for hyphal (tip) growth. *Protoplasma*, 153(1-2):46–57, 1989.

[3] Tobias I. Baskin. On the alignment of cellulose microfibrils by cortical microtubules: a review and a model. *Protoplasma*, 215(1-4):150–171, 2001.

[4] Roberto Bernal, Enrique Rojas, and Jacques Dumais. The mechanics of tip growth morphogenesis: what we have learned from rubber balloons. *Journal of Mechanics of Materials and Structures*, 2(6):1157–1168, 2007.

[5] Gabriel Billings, Nikolay Ouzounov, Tristan Ursell, Samantha M. Desmarais, Joshua Shaevitz, Zemer Gitai, and Kerwyn Casey Huang. *De novo* morphogenesis in L-forms via geometric control of cell growth: *De novo* morphogenesis in bacterial L-forms. *Molecular Microbiology*, 93(5):883–896, September 2014.

[6] Daria Bonazzi, Jean-Daniel Julien, Maryse Romao, Rima Seddiki, Matthieu Piel, Arezki Boudaoud, and Nicolas Minc. Symmetry Breaking in Spore Germination Relies on an Interplay between Polar Cap Stability and Spore Wall Mechanics. *Developmental Cell*, 28(5):534–546, March 2014.

[7] Frédéric Boudon, Jérôme Chopard, Olivier Ali, Benjamin Gilles, Olivier Hamant, Arezki Boudaoud, Jan Traas, and Christophe Godin. A Computational Framework for 3d Mechanical Modeling of Plant Morphogenesis with Cellular Resolution. *PLoS Computational Biology*, 11(1):e1003950, January 2015.

[8] Shaun M. Bowman and Stephen J. Free. The structure and synthesis of the fungal cell wall. *BioEssays*, 28(8):799–808, August 2006.

[9] Behruz Bozorg, Pawel Krupinski, and Henrik Jönsson. Stress and Strain Provide Positional and Directional Cues in Development. *PLoS Computational Biology*, 10(1):e1003410, January 2014.

[10] Siobhan A. Braybrook and Alexis Peaucelle. Mechano-Chemical Aspects of Organ Formation in Arabidopsis thaliana: The Relationship between Auxin and Pectin. *PLoS ONE*, 8(3):e57813, March 2013.

[11] M. T. Cabeen and C. Jacobs-Wagner. Skin and bones: the bacterial cytoskeleton, cell wall, and cell morphogenesis. *The Journal of Cell Biology*, 179(3):381–387, October 2007.

[12] Matthew T. Cabeen and Christine Jacobs-Wagner. Bacterial cell shape. *Nature Reviews Microbiology*, 3(8):601–610, August 2005.

[13] Otger Campàs and L. Mahadevan. Shape and Dynamics of Tip-Growing Cells. *Current Biology*, 19(24):2102–2107, December 2009.

[14] R. J. Carol and L. Dolan. Building a hair: tip growth in Arabidopsis thaliana root hairs. *Philosophical Transactions of the Royal Society B: Biological Sciences*, 357(1422):815–821, June 2002.

[15] Fred Chang and Kerwyn C. Huang. How and why cells grow as rods. *BMC biology*, 12(1):54, 2014.

[16] Youssef Chebli and Anja Geitmann. Gravity Research on Plants: Use of Single-Cell Experimental Models. *Frontiers in Plant Science*, 2, 2011.

[17] Youssef Chebli, Jens Kroeger, and Anja Geitmann. Transport Logistics in Pollen Tubes. *Molecular Plant*, 6(4):1037–1052, July 2013.

[18] Daniel J. Cosgrove. Growth of the plant cell wall. *Nature Reviews Molecular Cell Biology*, 6(11):850–861, November 2005.

[19] Tyler Drake and Dimitrios Vavylonis. Model of Fission Yeast Cell Shape Driven by Membrane-Bound Growth Factors and the Cytoskeleton. *PLoS Computational Biology*, 9(10):e1003287, October 2013.

[20] Jacques Dumais, Sidney L. Shaw, Charles R. Steele, Sharon R. Long, and Peter M. Ray. An anisotropic-viscoplastic model of plant cell mor-

phogenesis by tip growth. *The International Journal of Developmental Biology*, 50(2-3):209–222, 2006.

[21] Anne Mie C. Emons and Bela M. Mulder. The making of the architecture of the plant cell wall: How cells exploit geometry. *Proceedings of the National Academy of Sciences*, 95(12):7215–7219, 1998.

[22] P. Fayant, O. Girlanda, Y. Chebli, C.-E. Aubin, I. Villemure, and A. Geitmann. Finite Element Model of Polar Growth in Pollen Tubes. *The Plant Cell*, 22(8):2579–2593, August 2010.

[23] Leon Furchtgott, Ned S. Wingreen, and Kerwyn Casey Huang. Mechanisms for maintaining cell shape in rod-shaped Gram-negative bacteria: Rod-shape maintenance in Gram-negative bacteria. *Molecular Microbiology*, 81(2):340–353, July 2011.

[24] Anja Geitmann. How to shape a cylinder: pollen tube as a model system for the generation of complex cellular geometry. *Sexual Plant Reproduction*, 23(1):63–71, March 2010.

[25] Gerhard Gierz and Salomon Bartnicki-Garcia. A Three-Dimensional Model of Fungal Morphogenesis Based on the Vesicle Supply Center Concept. *Journal of Theoretical Biology*, 208(2):151–164, January 2001.

[26] Alain Goriely and Michael Tabor. Biomechanical models of hyphal growth in actinomycetes. *Journal of Theoretical Biology*, 222(2):211–218, May 2003.

[27] Alain Goriely and Michael Tabor. Mathematical modeling of hyphal tip growth. *Fungal Biology Reviews*, 22(2):77–83, May 2008.

[28] Claire Grierson, Erik Nielsen, Tijs Ketelaarc, and John Schiefelbein. Root Hairs. *The Arabidopsis Book*, 12:e0172, January 2014.

[29] Fangwei Gu and Erik Nielsen. Targeting and Regulation of Cell Wall Synthesis During Tip Growth in Plants: Cell Wall Synthesis and Targeting during Tip Growth. *Journal of Integrative Plant Biology*, 55(9):835–846, September 2013.

[30] Iain M. Hagan. The fission yeast microtubule cytoskeleton. *Journal of Cell Science*, 111(12):1603–1612, 1998.

[31] Olivier Hamant, Marcus G. Heisler, Henrik Jönsson, Pawel Krupinski, Magalie Uyttewaal, Plamen Bokov, Francis Corson, Patrik Sahlin, Arezki Boudaoud, Elliot M. Meyerowitz, and others. Developmental patterning by mechanical signals in Arabidopsis. *science*, 322(5908):1650–1655, 2008.

[32] Owen P. Hamill and Boris Martinac. Molecular basis of mechanotransduction in living cells. *Physiological reviews*, 81(2):685–740, 2001.

[33] Franklin M. Harold. Force and compliance: rethinking morphogenesis in walled cells. *Fungal Genetics and Biology*, 37(3):271–282, 2002.

[34] Marcus G. Heisler, Olivier Hamant, Pawel Krupinski, Magalie Uyttewaal, Carolyn Ohno, Henrik Jönsson, Jan Traas, and Elliot M. Meyerowitz. Alignment between PIN1 Polarity and Microtubule Orientation in the Shoot Apical Meristem Reveals a Tight Coupling between Morphogenesis and Auxin Transport. *PLoS Biology*, 8(10):e1000516, October 2010.

[35] Peter K. Hepler, Caleb M. Rounds, and Lawrence J. Winship. Control of Cell Wall Extensibility during Pollen Tube Growth. *Molecular Plant*, 6(4):998–1017, July 2013.

[36] D. M. Holloway and L. G. Harrison. Pattern Selection in Plants: Coupling Chemical Dynamics to Surface Growth in Three Dimensions. *Annals of Botany*, 101(3):361–374, December 2007.

[37] Martin Howard. How to build a robust intracellular concentration gradient. *Trends in Cell Biology*, 22(6):311–317, June 2012.

[38] Kerwyn Casey Huang, Ranjan Mukhopadhyay, Bingni Wen, Zemer Gitai, and Ned S. Wingreen. Cell shape and cell-wall organization in Gram-negative bacteria. *Proceedings of the National Academy of Sciences*, 105(49):19282–19287, 2008.

[39] M.Z.A.M. Jaffar and F.A. Davidson. Basic rules for polarised cell growth. *Journal of Theoretical Biology*, 336:44–51, November 2013.

[40] Hongyuan Jiang, Fangwei Si, William Margolin, and Sean X. Sun. Mechanical Control of Bacterial Cell Shape. *Biophysical Journal*, 101(2):327–335, July 2011.

[41] Henrik Jönsson, Marcus G. Heisler, Bruce E. Shapiro, Elliot M. Meyerowitz, and Eric Mjolsness. An auxin-driven polarized transport model for phyllotaxis. *Proceedings of the National Academy of Sciences of the United States of America*, 103(5):1633–1638, 2006.

[42] Jens H. Kroeger and Anja Geitmann. Pollen tube growth: Getting a grip on cell biology through modeling. *Mechanics Research Communications*, 42:32–39, June 2012.

[43] Benoît Landrein and Olivier Hamant. How mechanical stress controls microtubule behavior and morphogenesis in plants: history, experiments and revisited theories. *The Plant Journal*, 75(2):324–338, July 2013.

[44] Anita T. Layton, Natasha S. Savage, Audrey S. Howell, Susheela Y. Carroll, David G. Drubin, and Daniel J. Lew. Modeling Vesicle Traffic Reveals Unexpected Consequences for Cdc42p-Mediated Polarity Establishment. *Current Biology*, 21(3):184–194, February 2011.

[45] Peter N. Lipke and Rafael Ovalle. Cell wall architecture in yeast: new structure and new challenges. *Journal of bacteriology*, 180(15):3735–3740, 1998.

[46] Moritz Mercker, Alexandra Köthe, and Anna Marciniak-Czochra. Mechanochemical Symmetry Breaking in Hydra Aggregates. *Biophysical Journal*, 108(9):2396–2407, May 2015.

[47] Pascale Milani, Maryam Gholamirad, Jan Traas, Alain Arnéodo, Arezki Boudaoud, Françoise Argoul, and Olivier Hamant. In vivo analysis of local wall stiffness at the shoot apical meristem in Arabidopsis using atomic force microscopy: Measuring wall stiffness in meristems with AFM. *The Plant Journal*, 67(6):1116–1123, September 2011.

[48] B. M. Mulder and A. M. C. Emons. A dynamical model for plant cell wall architecture formation. *Journal of Mathematical Biology*, 42(3):261–289, March 2001.

[49] Naomi Nakayama, Richard S. Smith, Therese Mandel, Sarah Robinson, Seisuke Kimura, Arezki Boudaoud, and Cris Kuhlemeier. Me-

chanical Regulation of Auxin-Mediated Growth. *Current Biology*, 22(16):1468–1476, August 2012.

[50] Didier Reinhardt, Therese Mandel, and Cris Kuhlemeier. Auxin regulates the initiation and radial position of plant lateral organs. *The Plant Cell Online*, 12(4):507–518, 2000.

[51] Enrique R. Rojas, Scott Hotton, and Jacques Dumais. Chemically Mediated Mechanical Expansion of the Pollen Tube Cell Wall. *Biophysical Journal*, 101(8):1844–1853, October 2011.

[52] Kenneth E. Sawin and Paul Nurse. Regulation of cell polarity by microtubules in fission yeast. *The Journal of cell biology*, 142(2):457–471, 1998.

[53] Sidney L. Shaw, Jacques Dumais, and Sharon R. Long. Cell Surface Expansion in Polarly Growing Root Hairs ofMedicago truncatula. *Plant Physiology*, 124(3):959–970, 2000.

[54] Björn J. Sieberer, Tijs Ketelaar, John J. Esseling, and Anne Mie C. Emons. Microtubules guide root hair tip growth: Tansley review. *New Phytologist*, 167(3):711–719, July 2005.

[55] T. J. Silhavy, D. Kahne, and S. Walker. The Bacterial Cell Envelope. *Cold Spring Harbor Perspectives in Biology*, 2(5):a000414–a000414, May 2010.

[56] Shailendra P. Singh and Beronda L. Montgomery. Determining cell shape: adaptive regulation of cyanobacterial cellular differentiation and morphology. *Trends in Microbiology*, 19(6):278–285, June 2011.

[57] Courtney R. Terenna, Tatyana Makushok, Guilhem Velve-Casquillas, Damien Baigl, Yong Chen, Michel Bornens, Anne Paoletti, Matthieu Piel, and Phong T. Tran. Physical Mechanisms Redirecting Cell Polarity and Cell Shape in Fission Yeast. *Current Biology*, 18(22):1748–1753, November 2008.

[58] Simon H. Tindemans, Norbert Kern, and Bela M. Mulder. The diffusive vesicle supply center model for tip growth in fungal hyphae. *Journal of Theoretical Biology*, 238(4):937–948, February 2006.

[59] T. S. Ursell, J. Nguyen, R. D. Monds, A. Colavin, G. Billings, N. Ouzounov, Z. Gitai, J. W. Shaevitz, and K. C. Huang. Rod-like bacterial shape is maintained by feedback between cell curvature and cytoskeletal localization. *Proceedings of the National Academy of Sciences*, 111(11):E1025–E1034, March 2014.

[60] Tristan S. Ursell, Eliane H. Trepagnier, Kerwyn Casey Huang, and Julie A. Theriot. Analysis of Surface Protein Expression Reveals the Growth Pattern of the Gram-Negative Outer Membrane. *PLoS Computational Biology*, 8(9):e1002680, September 2012.

[61] Joseph E. Varner and Liang-Shiou Lin. Plant cell wall architecture. *Cell*, 56(2):231–239, 1989.

[62] An Yan, Guanshui Xu, and Zhen-Biao Yang. Calcium participates in feedback regulation of the oscillating ROP1 Rho GTPase in pollen tubes. *Proceedings of the National Academy of Sciences*, 106(51):22002–22007, 2009.

[63] K. D. Young. The Selective Value of Bacterial Shape. *Microbiology and Molecular Biology Reviews*, 70(3):660–703, September 2006.

[64] Rabah Zerzour, Jens Kroeger, and Anja Geitmann. Polar growth in pollen tubes is associated with spatially confined dynamic changes in cell mechanical properties. *Developmental Biology*, 334(2):437–446, October 2009.

Chapter 2

An introduction to the modeling of mechanics in development

In the previous chapter I talked mostly of the generation of shape at the cellular scale. In this one, I review some models used to study mechanical effects in development at the multicellular scale, on which the present PhD work rests. More technical details are provided. I start with the models studying the mechanical basis of morphogenesis. I also present two models where the impact of cell divisions is precisely investigated. Finally, I present some recent models that combine the mechanical and biochemical fields. These two parts are particularly relevant for my work on the cell divisions in the shoot apex and on the mechanical regulation of auxin transport.

This chapter does not aim at being an exhaustive summary of all the models, but rather presents some fundamental principles of the mechanics of development.

2.1 Cellular mechanical models of development

The investigation of morphogenesis, and of its mechanical aspects, using computational approaches, dates back to the pioneering work of Odell et al. [14]. In this work, they consider an annulus of cell, whose edges are modeled as simple linear viscoelastic element obeying:

$$\frac{dl}{dt} = -\frac{k}{\mu}\left(l - l^0\right)$$

where l and l^0 are the length and rest length of the cell edge, μ is viscosity and k the elastic constant. Cells are under tension, due to hydrostatic pressure. The symmetry breaking of the annulus is caused by the ability of a group of cells to actively contract upon stretching. When the elongation of these edges reaches a threshold, the rest length l^0 is reduced. With this simple mechanism, the model is able to reproduce several kind of invaginations (see Fig. 2.1). It is therefore an inspiring work for the study of morphogenesis.

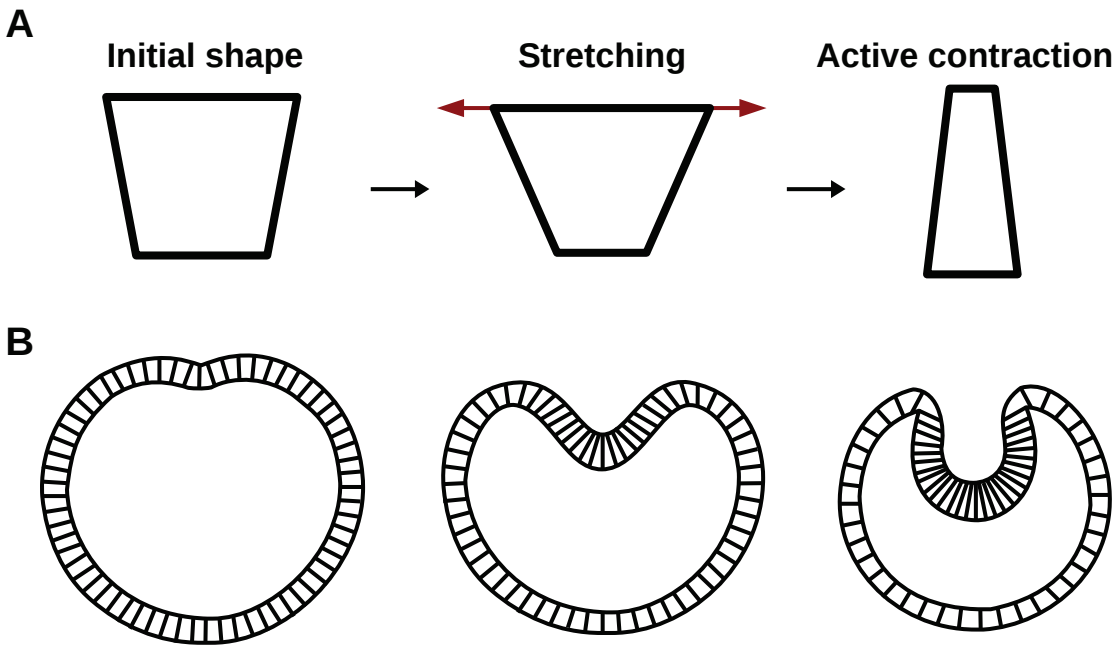

Figure 2.1: **Model of invagination:** (A) When the apical surface of an active cell is stretched upon a threshold, its active cortical filaments contract it to a much shorter equilibrium. (B) In an annulus of cells, only the cells in the upper hemisphere are active. The contraction of one cell then trigger a wave of contraction that leads ultimately to the invagination.

Another important development was due to Nagai et al. [12], who started from the vertex model for the evolution of soap froths and added a term that represents the resistance of the cells against deformation:

$$E = \sum_{j \in \text{edges}} \Lambda_j l_j + \sum_{i \in \text{cells}} \rho_i \left(h_i^0\right)^2 \left(A_i - A_i^0\right)^2 \tag{2.1}$$

where Λ_j is the line tension of the edge j, l_j its length, ρ_i characterizes the resistance against deformation of the cell i, h_i^0 its rest height, A_i its area and A_i^0 its rest area. As a result of the change of topology due to T1 transitions, a pattern with large variations evolves toward a realistic honeycomb-like pattern,

with symmetric cells, regular in size and number of neighbors. By giving a simple form for the energy that reproduces animal cell tissues, this work has paved the way for numerous mechanical models.

Farhadifar et al. developed a similar model [5], for the wing disk epithelium of the fly, that has been later extensively used. The mechanical energy is given by:

$$E = \sum_{i \in \text{cells}} \frac{K_i}{2} \left(A_i - A_i^0\right)^2 + \sum_{j \in \text{junctions}} \Lambda_j l_j + \sum_{i \in \text{cells}} \frac{\Gamma_i}{2} L_i^2 \tag{2.2}$$

where A_i and A_i^0 are the area and preferred area of the cell i, L_i its perimeter, and l_j the length of the junction j. K_i, Λ_j and Γ_i measure the importance of each contribution. This energy is very similar to the one defined by Nagai et al. (see Eq. 2.1), with the addition of the third term that stands for the contractility of each cell. In addition, growth is implemented by the doubling of the preferred area of a cell A^0, followed by its division and the mechanical relaxation of the tissue. The repetition of this process allows cell proliferation. This model is able to reproduce quantitatively the geometry of the cells. Importantly, very different cell shapes and topologies can be generated, depending on the relative contribution of the different terms in the energy, and thus showing that different tissues can rely on the same mechanisms.

The same mechanical model has been used by Aegerter-Wilsen et al. and combined with a more elaborate model for growth [2]. The major assumption is that the volume of a cell per time step increases either at a fixed rate or with an additional contribution proportional to the apical area of the cell. The main result is that a feedback from cell size is necessary to reproduce the experimental geometry of the cell. As more complex models has to account

for growth, its regulation by the cells properties is a fundamental question. Using still the same mechanical model, Osterfield et al. [15] have been able to reproduce the emergence of the tubular eggshell respiratory appendages from a two-dimensional epithelium. The symmetry breaking is achieved by increasing the stiffness and contractility (K and Γ in Eq. 2.2) of a patch of neighboring cells by a constant factor. Additionally, to mimic myosin cables that are observed in the tissue, the line tension (Λ in Eq. 2.2) in some junctions at the periphery of this patch is also increased. These modifications in the mechanics of the system are sufficient to generate the out-of-plane bending of the tissue. Further emergence of the tube is achieved by increasing even more the tension at the center of the myosin cables, still consistently with the experimental observation of myosin distribution. Then cells intercalation occur that tend to fuse the junctions with a higher line tension and thus lower the mechanical energy. The generation of a very anisotropic 3D structure with an initially 2D sheet using only patterns of apical tension is remarkable.

These works show that computational models, in particular vertex models, are powerful tools to study the mechanics of epithelial morphogenesis in animal. But although the mechanics of animal and plant cells are fundamentally different, similar models have been used to study their mechanics (See Eq. 2.2 and 2.4 for instance). In their book *The algorithmic beauty of plants* [16], first published in 1990, Przemyslaw Prusinkiewicz and Aristid Lindenmayer have implemented a vertex model for the mechanics of plant tissues. In this model, cell walls are linear springs, each cell exerts a 2D pressure on its cell walls, and a viscous damping force acts on the vertices. Cells grow because the pressure is inversely proportional to their area. Cell divisions are mod-

eled using L-systems, meaning that a certain number of cell types is defined (for instance apical cells or segment cells) and that it is sufficient to determine how it divides (see Fig. 2.2). This work is most certainly a milestone in the computational study of plant patterns.

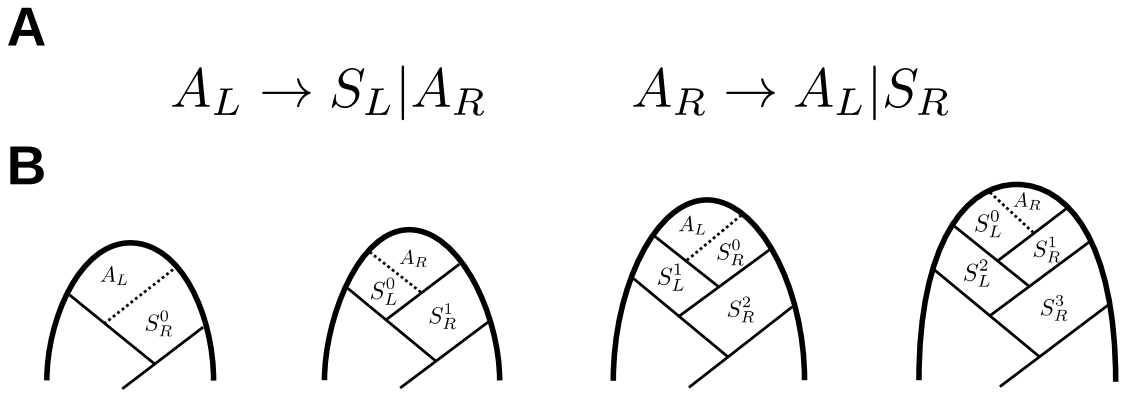

Figure 2.2: **Division system:** (A) Example of L-system for cell division. A and S stand for apical and segment cell. R and L stand for left or right and describe the position with respect to the division that has created the cell. An apical cell that appears on the left of the last cell wall is divided in one segment cell and one apical cell. An apical cell that appears on the right of the last cell wall is divided in one apical cell and one segment cell. Segment cells do not divide. (B) Application of the rule on a tissue. The superscript stands for the age of the cell.

Since the epidermal tissue of the plant is much thicker that the internal tissue, many models have been based on the assumption that the mechanics of the first layer of cells is sufficient to describe the dynamics of the shoot apex. A major contribution to this field comes from Hamant et al. [7] who have combined such a model with experiments to understand one of the fundamental feedback loop that links mechanical stress and mechanical anisotropy via the orientation of cellulose deposition. This feedback loop is one of the core mechanisms for the shoot apex morphogenesis. Hamant et al. model one layer of cells able to deform in the 3D space. The mechanical energy of the system

is given by the balance between the turgor pressure and the elasticity of the cell walls:

$$E = \sum_{j \in \text{walls}} \frac{k_j}{2} \left(\frac{l_j - l_j^0}{l_j^0} \right)^2 - \sum_{i \in \text{cells}} (pA_i + p_{int} V_{i,int}) \tag{2.3}$$

where k_j takes into account the stiffness of the cell wall, its depth and its thickness, l_j and l_j^0 its length and rest length, p is the 2D pressure in this layer of cells, A_i the area of the cell wall perpendicular to the cell layer, p_{int} the effective pressure resulting from the internal tissue and $V_{i,int}$ the internal volume. The anisotropic properties of the cell walls are taken into account by assuming a dependence of their stiffness, induced by the orientation of the microtubules:

$$k_j = k_{min} + k_{max} \cos(\theta_j)$$

where k_{min} and k_{max} define the isotropic and anisotropic contribution and θ_j the angle between the wall direction and the microtubules direction. The direction of the microtubules θ_i in a cell i is itself given at the scale of each cell by the average stress over its walls:

$$\theta_i = \frac{1}{2} \arctan \left(\frac{\sum_{j \in \text{walls}} F_j \sin(2\theta_j)}{\sum_{j \in \text{walls}} F_j \cos(2\theta_j)} \right)$$

Additionally, this orientation θ_i is computed with a temporal delay, microtubules reorientation and cellulose deposition being slower than mechanical processes. This model is able to reproduce the elongation of a stem and the emergence of a organ. More importantly it proves that cellulose deposition if regulated by mechanical cues, a mechanism involved in the generation of many anisotropic structures in plants.

Another major contribution comes from Uyttewaal et al., who showed that mechanics regulates cell growth and have a non-monotonic effect, where growth heterogeneity can be either dampened or amplified depending of the strength of the feedback [19]. In this approach, the mechanical anisotropy of the cells is accounted more directly through the energy of the tissue:

$$E = \sum_{i \in \text{cells}} \left(\alpha P_i + \beta \mathbf{Tr}^2 \left(M_i - M_i^0 \right) + \chi \mathbf{Det}^2 \left(M_i - M_i^0 \right) \right) \tag{2.4}$$

where P_i is the perimeter of the cell i, M_i and M_i^0 its shape and rest shape, and α, β, χ the mechanical parameter of the cell walls. The shape of a cell is measured as the second moment of area of its vertices (see [3] for the details). The key assumption, that is the regulation of growth by mechanics, is expressed in the growth equation:

$$\frac{dM_i^0}{dt} = \gamma(1 \pm \sigma) M_i^0 - \frac{\eta}{2} \left(M_i^0 D_i - D_i M_i^0 \right) \tag{2.5}$$

where γ is the growth rate, σ the amplitude of the fluctuations in growth rate, and η the strength of the feedback of mechanical stress on mechanical anisotropy, discussed earlier. This model predicts that increasing the strength of the mechanical feedback η first decreases growth variability, then increases it back for the higher strength. It is a remarkable insight on the mechanical regulation of growth, especially because the effect of mechanics is not monotonic, contrary to the first intuition one can have.

More recently, vertex models have been used to implement more elaborate mechanical behavior, with a description of the behavior of the cell walls using an approach of continuum mechanics. Fozard et al. implemented a model

of root growth including anisotropic non-linear viscoelastic mechanical properties [6]. The mechanical stress is divided into three different contributions: an isotropic viscous contribution including strain-softening $\boldsymbol{\sigma}_y$, an anisotropic linear contribution $\boldsymbol{\sigma}_a$ to represent the higher resistance of a fiber-reinforced material with respect to extension and shear in the direction of the fibers, and a usual elastic contribution. These terms $\boldsymbol{\sigma}_y$ and $\boldsymbol{\sigma}_a$ are expressed as:

$$\boldsymbol{\sigma}_y = 2\left(\mu_1 + \frac{\tau_w}{\varepsilon^*}\left(1 - \exp\left(-\frac{\varepsilon^*}{\varepsilon}\right)\right)\right)\boldsymbol{E}$$

$$\boldsymbol{\sigma}_a = \sum_{k=1,2}\left(\mu_2\left(\overrightarrow{a_k}.\boldsymbol{E}\overrightarrow{a_k}\right)\overrightarrow{a_k}\overrightarrow{a_k}^t + \mu_3\left(\overrightarrow{a_k}\left(\boldsymbol{E}\overrightarrow{a_k}\right)^t + \left(\boldsymbol{E}\overrightarrow{a_k}\right)\overrightarrow{a_k}^t\right)\right)$$

where μ_1 is the isotropic viscosity associated with the pectin matrix of the cell wall, τ_w sand ε^* the yield stress and yield strain rate of the cell wall, $\boldsymbol{E}$ the stiffness tensor, $\varepsilon = \sqrt{\sum_{i=1,2}\sum_{j=1,2} E_{ij}^2}$, $\overrightarrow{a_1}$ and $\overrightarrow{a_2}$ the principal directions of the cellulose microfibrils, and μ_2 and μ_3 the additional viscosity to elongation and shear of the fibers. These contributions are then attributed in different proportions to the three types of cell walls in the simulations: the cell walls in the plane of the simulation, and the transverse and the longitudinal cell walls in the plane of simulation. Additionally, the elongation of the root is allowed by a diffusing growth inhibitor produced only at tip that increases the yield stress of the cell walls. The advantage of this model is that the cell wall properties responsible for the anisotropic growth can be directly included. It also show that stiffening of the epidermal tissues tends to promote straight growth of the root. It is unclear whether this effect is biologically relevant or an artifact of the 2D approximation. Additionally, other feedback mechanisms could be required to stabilize the axis of growth. Nevertheless the growth of very anisotropic structure is challenging and this work gives

important insights on the improvement of computational techniques.
A lot of effort has been put into the modeling of plant mechanics in 2D, but ultimately 3D modeling would lead to a deeper understanding of morphogenesis. Recently, Boudon et al. developed a framework to model growth and mechanics in 3D at the cellular scale [4]. In this work the material is assumed to be linear, and any anisotropy can be taken into account. Growth is computed as the irreversible deformation of the 3D tissue above a strain threshold. See [4] for more details about the equations. The major insight of this work is that different mechanical properties can lead to the same shape, thus pointing out the importance for computational predictions upon mechanical perturbations and for measurements of the properties of the mechanical properties of the tissues.

2.2 Impact of the cell divisions

Divisions is a direct consequence of tissue growth, and several models have investigated specifically their impact on the topology, growth, and mechanics of the tissue. In the mechanical model of Sahlin et al. [17], the movement of the vertices is given by the balance of the forces exerted by the three cell walls of which it is the intersection:

$$\frac{d\overrightarrow{x_i}}{dt} = k \sum_{j \in \text{neighbours}} \frac{\overrightarrow{l_{ij}}}{l_{ij}} \left(\frac{l_{ij} - l_{ij}^0}{l_{ij}^0} \right) + k_r \overrightarrow{x_i}$$

where $\overrightarrow{x_i}$ is the position of the vertex i, $\overrightarrow{l_{ij}} = \overrightarrow{x_i} - \overrightarrow{x_j}$ and l_{ij}^0 the length and the rest length of the wall between the vertices i and j, and k the stiffness

of the cell wall. The second term mimic the effect of turgor pressure with a radial force determined by k_r. The notation has been slightly modified to be closer to the previous ones. From the energetic point of view, the first term is almost the same as the in the energy defined by Hamant et al. mentioned above (see Eq. 2.3). The growth of the cell wall is then described by:

$$\frac{dl_{ij}^0}{dt} = k_g \Theta \left(\frac{l_{ij} - l_{ij}^0}{l_{ij}} \right)$$

where k_g is the growth rate and Θ the ramp function $\Theta(x) = x$ if $x \geq 0$ and $\Theta(x) = 0$ if $x < 0$. This equation represents the fact that growth corresponds to the yielding of the cell wall upon stretching. Cell division could follow several rules, which have been tested with the model. The direction of the new cell wall can be determined by the shortest axis of the cell, randomly, orthogonal to the previous division, or orthogonal to the maximal deformation of the cell (averaged on its different walls). Once the direction is determined, the new wall can go through the center of mass of the cell or be positioned randomly. The conclusion of this work is that in order to get the best fit, the new wall must go through the center of mass of the cell and along the shortest path.

Later, Alim et al. showed that not only cell division rules affect the topology of the tissue, but also its growth [3]. The model is the same as in [19], which is described by the equations 2.4 and 2.5. The result of this study is that cell division rules based on the shortest path or the maximal stress of the cell wall release more stress and reduce the growth variability. In contrast, randomly oriented divisions, whether going through the center of the cell or not, generate equally large fluctuations in stress and growth and more

asymmetric cells. In conclusion, divisions are fundamental not only to control the topology and the shape of the cells, but also for the mechanics and the growth of the tissue.

2.3 Coupling mechanical and biochemical signals

Both mechanical and biochemical approaches are powerful to describe morphogenesis, but the coupling of the two fields, which as recently been the focus of many studies, opens promising perspectives.

Newell et al. [13] have showed that the continuous equations of shell buckling and auxin transport are similar and can be coupled either to cooperate or to compete in determining the patterns of auxin and deformations. The corresponding equation for the auxin concentration being itself derived from the discrete model used in [8] and involving many parameters, so we refer the reader to the papers for more details. The mechanics is described by the Föppl-von Karman-Donnell equations for the large deformations of thin shells. Depending on the parameters, auxin transport and mechanical constraints can compete, in which case the pattern is set by the dominant mechanism, while the other just match it linearly. If the cooperation takes place, the relationship between the mechanical constraint and the auxin concentration is non-linear. If the cooperation appears through the non-linear effects, the system displays patterns of the well-known Fibonacci class, whereas cooperation through the linear terms gives rise to concentric rings, with a constant number of peaks N and offset by an angle π/N .

Vertex models, because of their cellular resolution, are also well-suited to

study the interaction between mechanics and polarly distributed proteins. Salbreux et al. have used [18] a mechanical energy similar to the energy in Nagai et al. (see Eq. 2.1) to study the regular patterns in the Zebrafish retina. The mechanical model is coupled with two polar proteins that inhibit each other inside the cells and activate each other across the cell junctions. These proteins modify the mechanics of the system by decreasing line tension whereas mechanics affects the proteins through their preferential collection on the short junctions (see [18] for details). The distribution of cone photoreceptors during growth and regeneration is finally reproduce by applying an anisotropic stress on the tissue. The model is validated by the observation of polarly-distributed protein and with a mutant whose mechanical stress in perturbed. Interestingly, their model is able to generate short-range correlations in the polarity and shapes of the cells, but a large-scale anisotropic stress is necessary to get long-range correlations and very regular tissues, similar to the real ones.

Because of the vast knowledge we have about many molecular actors of development, more complex biochemical processes studied, jointly with mechanics. The mechanical model of Farhadifar et al. [5] (see Eq. 2.2) was used more recently [1], coupled with the regulatory network of the wing imaginal disc (See [1] for details on the biochemical system). By adding to the network the hypothetical activation or inhibition of some protein activities by mechanical compression, the model is able to account for some observations that were left unexplained so far. In addition the predictions about cell shapes and sizes were confirmed experimentally. This work emphasizes how combining both morphogenetic fields can overcome the limit of the previous models.

Mercker et al. showed that the coupling between morphogen expression and

curvature of the tissue can generate patterns of gene expression without relying on the still debated Turing systems [11]. The tissue is considered as a thin membrane, whose energy is computed via a Helfrich energy:

$$E = \int_{\Gamma} \kappa(\phi) \left(H - H_0(\phi)\right)^2 dS$$

where Γ is the surface of the tissue, κ is the bending rigidity of the surface, H and H_0 the mean curvature and the preferred curvature of the tissue. The energy has been modified so that κ and H_0 depends on the morphogen concentration ϕ. The production of the diffusing morphogen is assumed to increase with the curvature, whereas its concentration in turn feedback the mechanics of the tissue by increasing κ and H_0. This feedback loop is able to generate isotropic patterns of various wavelengths. Additionally, the biological relevance of this model can be investigated by deforming the tissue and observing the modification of the morphogen distribution. Although the relevance of reaction-diffusion systems is accepted for some biological systems, it is still strongly debated in some cases [9, 10]. Consequently, model suggesting new and simple patterning mechanisms are promising, especially when their relevance is easy to test experimentally.

References

[1] T. Aegerter-Wilmsen, M. B. Heimlicher, A. C. Smith, P. B. de Reuille, R. S. Smith, C. M. Aegerter, and K. Basler. Integrating force-sensing and signaling pathways in a model for the regulation of wing imaginal disc size. *Development*, 139(17):3221–3231, September 2012.

[2] T. Aegerter-Wilmsen, A. C. Smith, A. J. Christen, C. M. Aegerter, E. Hafen, and K. Basler. Exploring the effects of mechanical feedback on epithelial topology. *Development*, 137(3):499–506, February 2010.

[3] Karen Alim. Regulatory role of cell division rules on tissue growth heterogeneity. *Frontiers in Plant Science*, 3, 2012.

[4] Frédéric Boudon, Jérôme Chopard, Olivier Ali, Benjamin Gilles, Olivier Hamant, Arezki Boudaoud, Jan Traas, and Christophe Godin. A Computational Framework for 3d Mechanical Modeling of Plant Morphogenesis with Cellular Resolution. *PLoS Computational Biology*, 11(1):e1003950, January 2015.

[5] Reza Farhadifar, Jens-Christian Röper, Benoit Aigouy, Suzanne Eaton, and Frank Jülicher. The Influence of Cell Mechanics, Cell-Cell Interactions, and Proliferation on Epithelial Packing. *Current Biology*, 17(24):2095–2104, December 2007.

[6] John A. Fozard, Mikaël Lucas, John R. King, and Oliver E. Jensen. Vertex-element models for anisotropic growth of elongated plant organs. *Frontiers in Plant Science*, 4, 2013.

[7] Olivier Hamant, Marcus G. Heisler, Henrik Jönsson, Pawel Krupinski, Magalie Uyttewaal, Plamen Bokov, Francis Corson, Patrik Sahlin,

Arezki Boudaoud, Elliot M. Meyerowitz, and others. Developmental patterning by mechanical signals in Arabidopsis. *science*, 322(5908):1650–1655, 2008.

[8] Henrik Jönsson, Marcus G. Heisler, Bruce E. Shapiro, Elliot M. Meyerowitz, and Eric Mjolsness. An auxin-driven polarized transport model for phyllotaxis. *Proceedings of the National Academy of Sciences of the United States of America*, 103(5):1633–1638, 2006.

[9] P. K. Maini, T. E. Woolley, R. E. Baker, E. A. Gaffney, and S. S. Lee. Turing's model for biological pattern formation and the robustness problem. *Interface Focus*, 2(4):487–496, August 2012.

[10] H. Meinhardt. Turing's theory of morphogenesis of 1952 and the subsequent discovery of the crucial role of local self-enhancement and long-range inhibition. *Interface Focus*, 2(4):407–416, August 2012.

[11] Moritz Mercker, Dirk Hartmann, and Anna Marciniak-Czochra. A Mechanochemical Model for Embryonic Pattern Formation: Coupling Tissue Mechanics and Morphogen Expression. *PLoS ONE*, 8(12):e82617, December 2013.

[12] Tatsuzo Nagai and Hisao Honda. A dynamic cell model for the formation of epithelial tissues. *Philosophical Magazine Part B*, 81(7):699–719, July 2001.

[13] Alan C. Newell, Patrick D. Shipman, and Zhiying Sun. Phyllotaxis: Cooperation and competition between mechanical and biochemical processes. *Journal of Theoretical Biology*, 251(3):421–439, April 2008.

[14] G. Odell, G. Oster, B. Burnside, and P. Alberch. A mechanical model for epithelial morphogenesis. *Journal of mathematical biology*, 9(3):291–295, 1980.

[15] Miriam Osterfield, XinXin Du, Trudi Schüpbach, Eric Wieschaus, and Stanislav Y. Shvartsman. Three-Dimensional Epithelial Morphogenesis in the Developing Drosophila Egg. *Developmental Cell*, 24(4):400–410, February 2013.

[16] Przemyslaw Prusinkiewicz and Aristid Lindenmayer. *The algorithmic beauty of plants*. Springer Science & Business Media, 2012.

[17] Patrik Sahlin and Henrik Jönsson. A Modeling Study on How Cell Division Affects Properties of Epithelial Tissues Under Isotropic Growth. *PLoS ONE*, 5(7):e11750, July 2010.

[18] Guillaume Salbreux, Linda K. Barthel, Pamela A. Raymond, and David K. Lubensky. Coupling Mechanical Deformations and Planar Cell Polarity to Create Regular Patterns in the Zebrafish Retina. *PLoS Computational Biology*, 8(8):e1002618, August 2012.

[19] Magalie Uyttewaal, Agata Burian, Karen Alim, Benoît Landrein, Dorota Borowska-Wykręt, Annick Dedieu, Alexis Peaucelle, Michał Ludynia, Jan Traas, Arezki Boudaoud, Dorota Kwiatkowska, and Olivier Hamant. Mechanical Stress Acts via Katanin to Amplify Differences in Growth Rate between Adjacent Cells in Arabidopsis. *Cell*, 149(2):439–451, April 2012.

Chapter 3

SYMMETRY BREAKING IN SPORE GERMINATION RELIES ON AN INTERPLAY BETWEEN POLAR CAP STABILITY AND SPORE WALL MECHANICS

3.1 Summary

The fission yeast, because of its rod-like shape, has been a perfect system for the study of morphogenesis. However, most studies focused on its vegetative growth phase, during which the yeast grows by tip elongation and divides in its middle. Here, we are interested in the germination of the spores, an intriguing process during which polarity is *de novo* established and stabilized. The spherical cells regain its cylindrical shape during a phase called outgrowth.

Time-lapse phase-contrast microscopy of germination show that spores first grow isotropically. A quantitative analysis shows that the onset of the outgrowth is associated with a very robust fold change in their volumes, independent of the absolute size of the spores or their cell-cycle progression. To investigate the establishment of the polarity, we then turned our attention to several polarity markers. They appear to be co-localized in a small cap, the polarisome. Before the outgrowth, it disassembles and reassembles at several locations, thus making growth to look isotropic. Interestingly, each new formation of the polarisome is accompanied by a small localized growth, suggesting that the polar growth machinery is already effective. Moreover, measurements of concentrations of the polarity factors do not show any saturation or threshold corresponding to the outgrowth. Finally, electron microscopy of the spore shows that the protective shell that gives them their typical resistance is broken when the outgrowth starts, and that the outgrowth takes place at the position of this rupture. Because of all these observations, we formulate the hypothesis that mechanics could be the core mechanism of triggering and stabilization of the polarity.

I implemented a finite element model of spore growing under the action of turgor pressure, surrounded by a shell that cannot grow but is able to break when its stress reach a threshold. A random movement of the polarisome is sufficient to reproduce the volume fold change, confirming our hypothesis before the outgrowth. Mutants with defective outer cell walls display outgrowth at smaller fold changes, confirming this hypothesis. Additionally, mutants with diffuse polarity show multiple simultaneous ruptures, which also support our model. Finally, breaking the shell with a laser triggers the outgrowth if and only if the breaking is performed on the position of the polarisome.

In order to extend the model to the stabilization, I tried to bias this random movement towards what seems to be typical from the tip of the spore, that is the minimal stress, the maximal curvature or the maximal surface expansion rate. It appears that the third hypothesis is the only one able to reproduce the stabilization. It also explains the movement of the polarisome before the rupture: the positive feedback loop between growth and polarity is hindered by the mechanical inhibition of growth. Finally, artificially hindering blocking growth by putting the spores in microchambers, thus mimicking the mechanical constraint of the outer spore wall, delays the stabilization and fits with the feedback we formulated.

For this project I developed the model with some input from Arezki and implemented it. I analyzed the simulations and wrote the description of the model.

3.2 Paper

D. Bonazzi*, JD. Julien*, M. Romao, R. Seddiki, M. Piel, A. Boudaoud, and N. Minc

Symmetry Breaking in Spore Germination Relies on an Interplay between Polar Cap Stability and Spore Wall Mechanics

Developmental Cell 28 , 534–546, March 10, 2014

Developmental Cell
Article

Symmetry Breaking in Spore Germination Relies on an Interplay between Polar Cap Stability and Spore Wall Mechanics

Daria Bonazzi,[1,2,6] Jean-Daniel Julien,[3,4,5,6] Maryse Romao,[2] Rima Seddiki,[1] Matthieu Piel,[2] Arezki Boudaoud,[3,5,*] and Nicolas Minc[1,*]
[1]Institut Jacques Monod, 15 rue Hélène Brion, 75205 Paris Cedex 13, France
[2]Institut Curie, UMR 144 CNRS/IC, 26 rue d'Ulm, 75248 Paris Cedex 05, France
[3]Laboratoire Joliot-Curie, CNRS, ENS de Lyon, Université de Lyon, 46 Allée d'Italie, 69364 Lyon Cedex 07, France
[4]Laboratoire de Physique, CNRS, ENS de Lyon, UCBL Lyon I, 46 Allée d'Italie, 69364 Lyon Cedex 07, France
[5]Reproduction et Développement des Plantes, INRA, CNRS, ENS de Lyon, UCBL Lyon I, 46 Allée d'Italie, 69364 Lyon Cedex 07, France
[6]These authors contributed equally to this work
*Correspondence: arezki.boudaoud@ens-lyon.fr (A.B.), minc@ijm.univ-paris-diderot.fr (N.M.)
http://dx.doi.org/10.1016/j.devcel.2014.01.023

SUMMARY

The morphogenesis of single cells depends on their ability to coordinate surface mechanics and polarity. During germination, spores of many species develop a polar tube that hatches out of a rigid outer spore wall (OSW) in a process termed outgrowth. However, how these awakening cells reorganize to stabilize this first growth axis remains unknown. Here, using quantitative experiments and modeling, we reveal the mechanisms underlying outgrowth in fission yeast. We find that, following an isotropic growth phase during which a single polarity cap wanders around the surface, outgrowth occurs when spores have doubled their volume, concomitantly with the stabilization of the cap and a singular rupture in the OSW. This rupture happens when OSW mechanical stress exceeds a threshold, releases the constraints of the OSW on growth, and stabilizes polarity. Thus, outgrowth exemplifies a self-organizing morphogenetic process in which reinforcements between growth and polarity coordinate mechanics and internal organization.

INTRODUCTION

Organisms ranging from bacteria to fungi and plants can produce spores. These are dehydrated cells adapted for survival in harsh environments over very long periods of time ranging from weeks to thousands of years in some bacteria (Cano and Borucki, 1995; McKenney et al., 2013; Neiman, 2005). Spore resistance is associated with a rigid protective extracellular shell deposited at sporulation, called the outer spore wall (OSW) or spore coat (Arellano et al., 2000; García et al., 2006; Klobutcher et al., 2006; Wallace et al., 2011). Once conditions are favorable, spores germinate to exit dormancy, resume growth, and develop a single polarized tube that hatches out of the OSW, in a process termed outgrowth (Hatanaka and Shimoda, 2001; Kono et al., 2005; Pandey et al., 2013). Because of its particular cell cycle, de novo protein synthesis, and exit from prolonged period of dormancy, outgrowth poses an outstanding morphogenetic puzzle, which is to understand how these awakening symmetric cells may reorganize their interior to stabilize their very first polarized growth axis.

Polarized growth involves the formation of cortical polar caps of the GTP-bound form of a GTPase, such as Cdc42p in yeast (Drubin, 1991). These caps may be spatially stabilized by extrinsic cues, or can self-assemble at random positions by positive feedback (Drubin, 1991; Howell et al., 2012; Wedlich-Soldner et al., 2003; Wu and Lew, 2013). Yet, it becomes increasingly clear that mechanisms regulating cap establishment and/or stabilization may largely vary between different periods of cellular life cycles, even in a single given organism (Bendezú and Martin, 2013; Das et al., 2012; Dyer et al., 2013; Wu and Lew, 2013). In yeast and fungal cells, polar caps serve as platforms to direct local membrane addition and cell-wall remodeling, needed for surface expansion (Chang and Martin, 2009; Drubin, 1991). Growth itself involves mechanical work from high internal osmotic pressure that allows deforming newly synthesized cell wall (Bastmeyer et al., 2002; Boudaoud, 2003; Minc et al., 2009a). Thus, the morphogenesis of these single cells ultimately relies on an integration of biochemical and biomechanical signals (Harold, 1990; Slaughter and Li, 2006).

Here, we use quantitative time-lapse microscopy to understand how single spores break symmetry to become rod shaped in the model fission yeast *Schizosaccharomyces pombe*. We show that germination is followed by a long period of near-isotropic growth during which a single polar cap of active-cdc42p wanders around and drives small local growth sites that fail to progress, disassemble, and reform at a new position. We demonstrate that this unstable behavior is associated with the presence of the rigid OSW, which acts as a mechanical barrier that hinders growth and destabilizes polarity, and that cap stabilization occurs at outgrowth when the OSW ruptures. We develop a computational model that fully reproduces spore development in silico. This work demonstrates that the switch in polar cap stability at outgrowth can be explained by a simple positive-feedback loop between growth and polar cap stabilization.

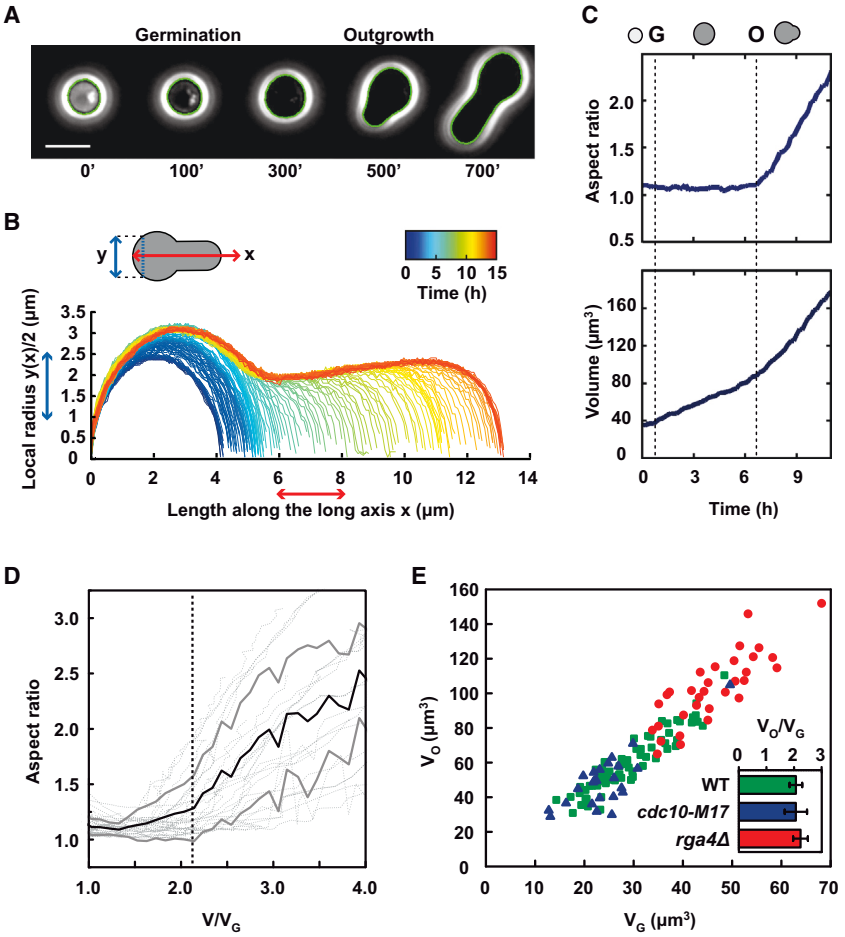

Figure 1. Spore Outgrowth Onset Correlates with a Robust Size-Increase Threshold

(A) Phase-contrast time-lapse superimposed with automated shape contour detection of a wild-type fission yeast spore germinating and outgrowing.

(B) Morphogenetic plot representing the temporal evolution of cell morphogenesis.

(C) Evolution of single-cell aspect ratio and volume as a function of time.

(D) Integrated morphogenesis at the population level (n = 25 spores). The black line depicts the averaged cell aspect ratio as a function of the averaged cell volume normalized with the volume at germination. Thick gray lines delimit the SD, and thin gray lines are plots arising from individual spore morphogenesis tracking.

(E) Volume at the onset of outgrowth, V_0 plotted as a function of the volume at germination, V_G. These volumes are measured from time-lapse phase images. The onset of outgrowth is defined as the inflexion point of the aspect ratio curve. Green, blue, and red data points, respectively, correspond to single WT, *cdc10-M17* at restrictive temperature (37°C), and *rga4Δ* spores. Error bars represent SDs. Scale bars, 5 µm. See also Figure S1 and Movies S1 and S2.

RESULTS

The Developmental Morphogenesis of Single Fission Yeast Cells

We quantitated the morphogenetic development of single fission yeast spores by performing long (over 10 hr) time-lapse phase-contrast microscopy with frequencies down to 5 min (Figure 1A; Movie S1 available online). Spores were rapidly transferred from starvation media to agar pad containing rich media. Phase contrast allowed delineating germination onset, which is characterized by a bright-phase to dark-phase transition (Figure S1A) (Hatanaka and Shimoda, 2001). Spores then grew in a near-isotropic manner for about 6–8 hr and entered outgrowth, which corresponds to the definition and stabilization of the first polarized growth axis characterizing the rod-shaped fission yeast cell (Hatanaka and Shimoda, 2001) (Figure 1A). The cells then kept on growing for another 3–4 hr before entering mitosis. Outgrowing cells kept their bottle-like shape and remained monopolar, growing away from the spore body for several cell cycles (Movie S2). Phase images were segmented and analyzed to quantitate single spore dimensions, aspect ratios, and volumetric growth rates (Figures 1B–1D; Experimental Procedures). At outgrowth, the aspect ratio depicted a sharp increase, which marked the extension of the polarized tube, and single-cell growth rates also increased abruptly by a factor of 2.4 ± 0.4 on average (Figure S1B).

Outgrowth Onset Is Associated with a Robust Fold Change in Cell Size

We used this approach to investigate whether outgrowth could correlate with an internal timer, a size increase, or a specific spore size (Mitchison and Nurse, 1985). The absolute time from germination to outgrowth depicted cell-to-cell variation of around 30% in the same field of observation. Not surprisingly, this timing was also largely dependent on temperature, humidity, as well as strain background (data not shown). We thus used cell volume as an indicator of spore developmental progression, to generate an averaged morphogenetic development at the cell population level (Figure 1D). This analysis revealed that the onset of outgrowth correlated with a fixed spore volume increase. We thus computed the volume at germination (V_G) and at the onset of outgrowth (V_O) for individual spores. This showed that the volume at outgrowth can vary up to 3- to 4-fold in a wild-type (WT) population and revealed a linear scaling between V_O and V_G (R^2 = 0.87) with a slope of 2.07 ± 0.12 (n = 67). This scaling was similar in spores with larger initial volumes like those produced by the fat mutant *rga4Δ* (volume ratio, $< V_O/V_G > =$ 2.22 ± 0.13, n = 32) (Figure 1E) (Das et al., 2007; Tatebe et al., 2008). This size increase was also independent on G1/S cell-cycle transition, which is known to occur around these stages of spore development (Hatanaka and Shimoda, 2001; Mitchison and Nurse, 1985), as spores of the *cdc10-M17* mutant, which arrest in G1 at restrictive temperature (Nurse et al., 1976), depicted similar volume ratios ($<V_O/V_G> = 2.07 \pm 0.20$, n = 23) (Figures 1E, S1C, and S1D). Thus, outgrowth correlates with spore

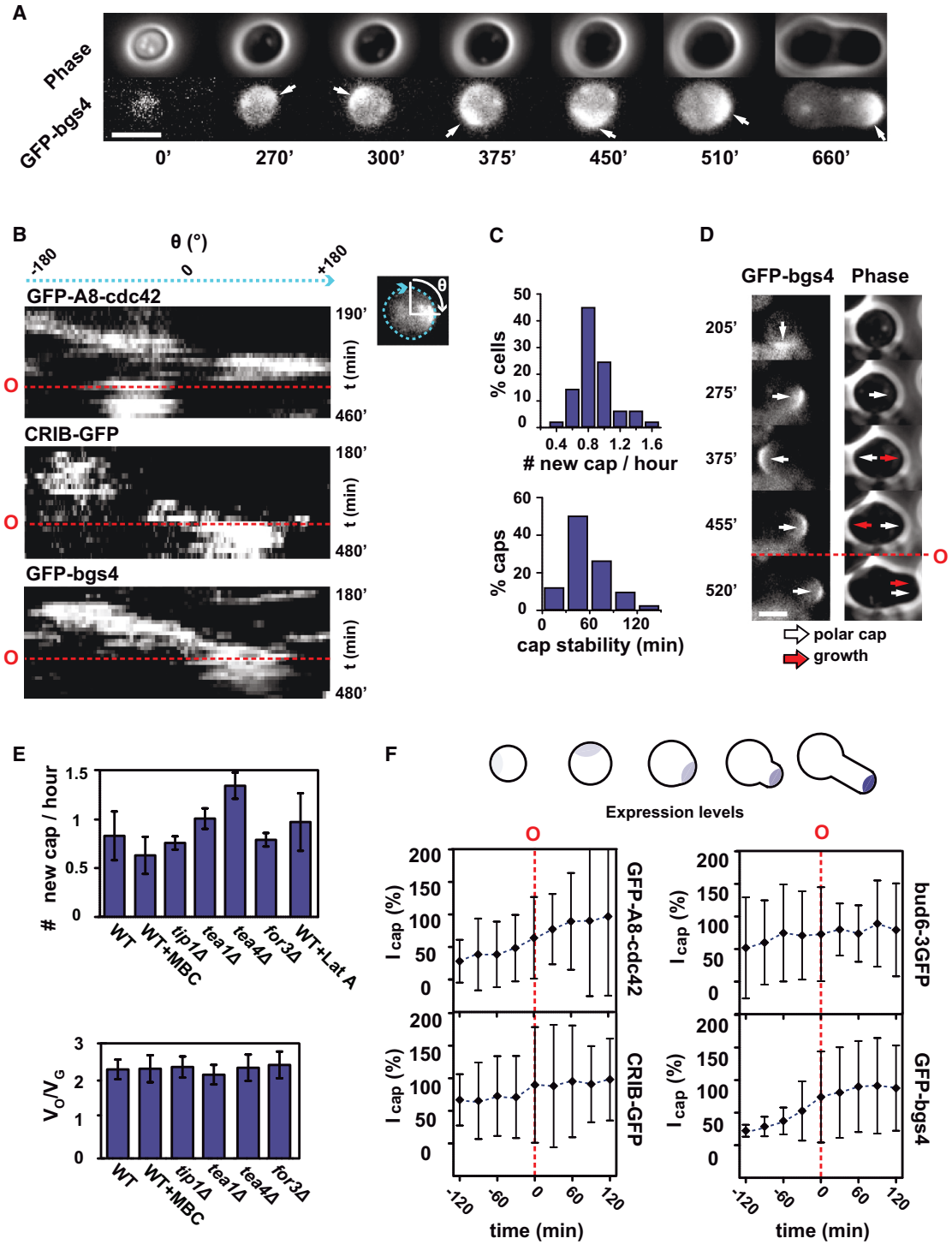

Figure 2. A Polarity Cap Wanders around the Symmetric Spore and Finally Stabilizes to Promote Outgrowth

(A) Time-lapse phase-contrast and epifluorescence images of a developing spore expressing the polarized growth marker GFP-bgs4. White arrows point at newly assembled caps.

(B) Cell kymographs representing the changes of localization over time of the polarity factors GFP-A8-cdc42, CRIB-GFP (a marker for active GTP-cdc42), and GFP-bgs4. Kymographs for GFP-bgs4 and GFP-A8-cdc42 are computed from epifluorescence time lapse, whereas those for CRIB-GFP are computed from confocal single midslices.

(C) Quantification of polar cap frequency and stability in time (n = 50 spores). A new polar cap is defined as a newly assembled cap at a different location than the previous one. Final stable outgrowth caps are not counted. Cap stability corresponds to the time between assembly and disassembly.

(legend continued on next page)

volume doubling, independently of absolute size or cell-cycle progression.

A Wandering Polar Cap Becomes Stable at Outgrowth

To understand polarity establishment and stabilization in spores, we then imaged fluorescently tagged canonical polarity markers throughout spore development. For polarized growth, vegetative fission yeast cells assemble clusters of polarity proteins into a polar cap at their growing tips (Chang and Martin, 2009). This cluster includes the small GTPase cdc42p, actin regulators, and cell-wall remodeling factors, which promote tip growth. We followed the localization of GFP-tagged cdc42p (Rincón et al., 2009) and its active GTP-bound form using the CRIB-GFP fusion (Tatebe et al., 2008), the actin-associated marker bud6-3GFP (Glynn et al., 2001) and the membrane glucan synthase GFP-bsg4, which marks sites of cell-wall synthesis (Cortés et al., 2005). Strikingly, all these factors assembled into a single cap long before outgrowth (first visible between 1 and 3 hr after germination), which disassembled and reassembled at successive locations, yielding a stochastic wandering motion around the spore surface, and finally stabilized to promote outgrowth (Figures 2A, 2B, S2A, and S2B; Movie S3). In some cases, the polar cap completely disassembled to reform at a new location, whereas, in other cases, the cap displayed local sliding or rearrangement in a restricted area of the spore surface (Movie S3). This unstable behavior was reminiscent of oscillating states of polarity in budding yeast, vegetative fission yeast, and in adherent mammalian cells (Bendezú and Martin, 2012, 2013; Das et al., 2012; Fink et al., 2011; Howell et al., 2012; Wedlich-Soldner et al., 2003). However, in these spores, a large fraction of caps appeared to be stable for a comparatively longer time period (ranging from 30 to 90 min) (Figure 2C). This yielded an average frequency of about 0.75 newly assembled caps per hour and a total of three to four transient unstable caps visible in the plane of focus between germination and outgrowth. We did not note dampening of cap wandering behavior before stabilization. Rather, the transition between wandering and definitive docking of the cap appeared to be abrupt in most cases (Figures 2B and S2A).

Importantly, all these polarity components colocalized two by two, and cowandered together (Figure S2C). In addition, transient cap formation led in ~65% of cases to small localized growth sites that extended out of the rounded spore and failed to progress (Figure 2D; Movie S4). Local growth followed the assembly of a new GFP-bgs4 polar cap with a time delay ranging from 5 to 20 min typically (Figure 2D; Movie S4). Thus, the upstream polarity machinery appears to be properly assembled and competent for polar growth soon after germination, but destabilizing elements may hinder polarity maintenance until the spore has increased its volume sufficiently.

Cap Stabilization Does Not Involve NETO Factors, Memory Cues, or Polarity Protein Levels

We next tested if elements that spatially stabilize polarity in vegetative cells could contribute to cap maintenance at outgrowth. One class of such characterized factors are those that promote polarity establishment at the new end (NETO, New End Take Off) in vegetative cells, such as microtubules (MTs) and MT + TIP factors (Chang and Martin, 2009). MTs in spores were short and disorganized until after outgrowth, and treatment with a microtubule-inhibitory drug (MBC), which blocks MT polymerization in spores and cells neither blocked wandering nor altered volume-doubling required for stabilization. In addition, mutants in MT-based polarity pathways defined by tip1p, tea1p, and tea4p and mutants defective in actin cables assembly such as in the formin for3p all showed similar behavior as WT (Figures 2E, S3A, S3C, and S3E). Complete depolymerization of actin with Latrunculin A halted spore growth but did not block wandering, as seen in other cell types exhibiting polarity oscillations (Figures 2E, S3B, and S3D) (Howell et al., 2012).

Cap stabilization did not appear to involve fixed spatial cues in the spore (Chang and Martin, 2009; Drubin, 1991). Spores that remained attached to each other assuming the shape of the mother ascus outgrew along an axis independent of the previous meiotic division axis (Figure S3F; Movie S5). Additionally, in a subset of time lapses we saw the polar cap exploring several times the incipient site of outgrowth, before stabilizing (see Movie S4, for an example). These data suggest that outgrowth involves different polarity stabilizing elements than in vegetative cells.

We also quantified the concentration of these polarity factors in the cap with confocal microscopy, to test a hypothesis in which polarity proteins that are being de novo synthesized in spores may need to reach a saturating level to stabilize. This showed that the expression levels were noisy with 5- to 10-fold variations in protein concentration at the cap between different spores at a given time, so that some outgrowing spores could display concentrations lower than spores at earlier stages. Also, the overall increase in expression did not obviously saturate at outgrowth and continued to rise until the first mitosis (Figure 2F). Although these data do not rule out the existence of a concentration threshold in an uncharacterized cytoplasmic factor that may stabilize the cap, they do not support a cap maturation model needed for stabilization.

The Outer Spore Wall Encases the Spore and Displays a Singular Rupture at Outgrowth

We thus turned our attention to factors that are specific to this spore-to-cell transition. One specific feature of spores is the encasing OSW. The fission yeast OSW is deposited onto the inner cell wall during sporulation, and is also composed of polysaccharides, but it features different crosslinking and the

(D) Time-lapse phase-contrast and fluorescence images of GFP-bgs4 cap wandering and corresponding local growth site.
(E) Frequency of newly assembled successive GFP-bgs4 polar caps, in the indicated conditions and mutants, and corresponding outgrowth volume ratio V_0/V_G ($n > 25$ spores for each condition).
(F) Quantification of changes in fluorescence levels of different polarity factors (see Experimental Procedures): GFP-A8-cdc42, CRIB-GFP, bud6-3GFP, and GFP-bgs4 from 2 hr before to 2 hr after outgrowth ($n > 10$ spores for each marker). Error bars represent SDs.
Scale bars, 5 μm. See also Figures S2 and S3 and Movies S3 and S4.

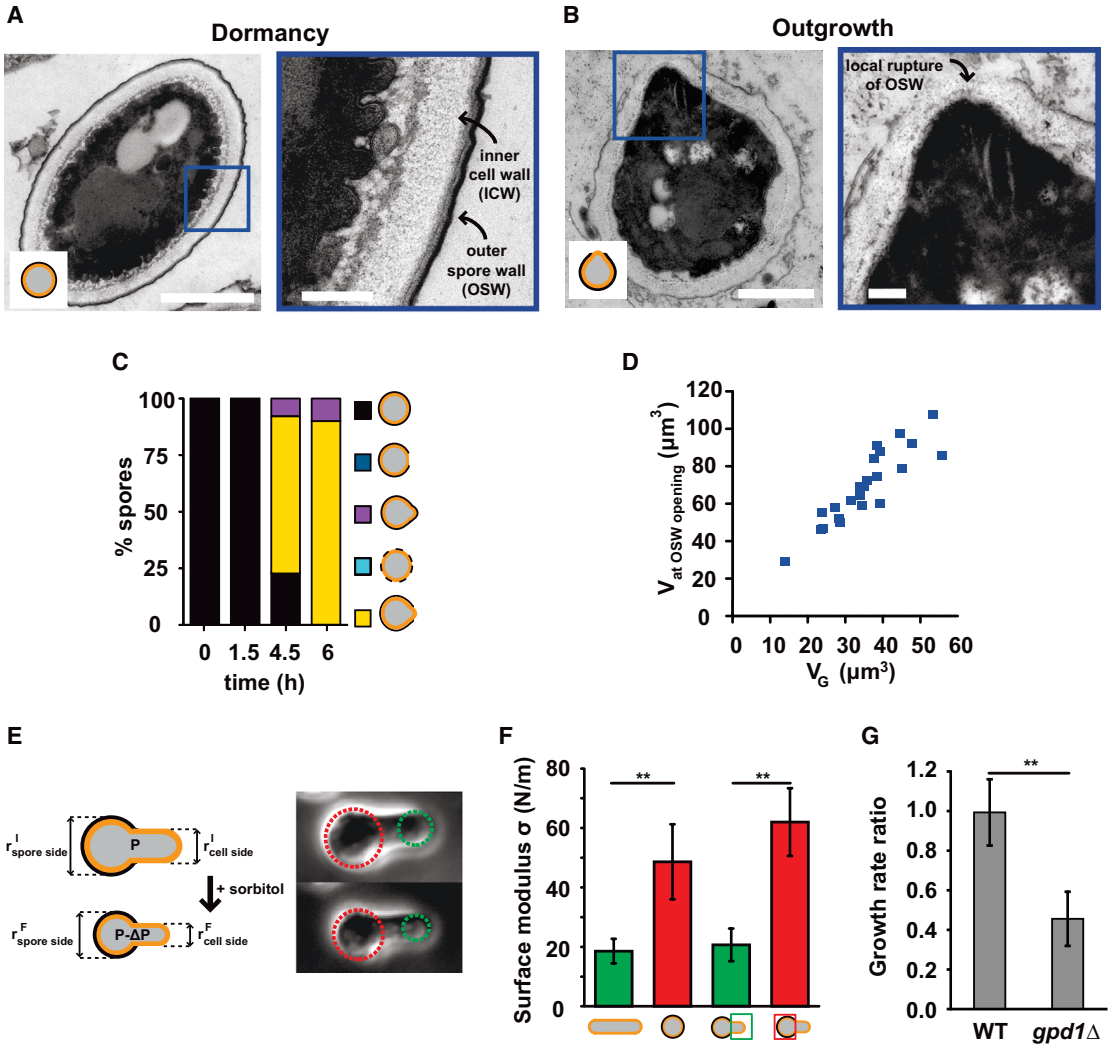

Figure 3. The Outer Spore Wall Is Rigid and Displays a Singular Rupture at the Time and Location of Outgrowth

(A) Transmission electron microscopy picture of a dormant spore and corresponding close-up view on OSW.

(B) Outgrowing spore after 6 hr of incubation at 30°C and corresponding close-up view on the outgrowth site, which displays a local rupture in the OSW (scale bars in large view, 1 μm; and in close-ups, 200 nm).

(C) Quantification of the phenotypes of outer wall rupture at different times from germination (n = 52 spores).

(D) Volume at the moment of OSW rupture, as assayed by growing spores in medium supplemented with an inner/vegetative cell-wall digestion mix, plotted as a function of the volume at germination for WT spores.

(E) Stress-strain approach used to measure the elastic properties of the inner and outer wall.

(F) Cell-wall surface moduli for vegetative cells, spores, and the two sides of an outgrown spore (n > 10 cells or spores).

(G) Ratio between growth rate before and after treatment with sorbitol measured in WT and *gpd1Δ* spores (n = 7 spores for each condition). Error bars represent SDs.

**p < 0.01, Student's t test. See also Figure S3.

presence of chitin, both of which may confer atypical properties that allow this layer to protect spores from harsh environment (Arellano et al., 2000; García et al., 2006; Tanaka and Hirata, 1982). We visualized the OSW at gradual time intervals using transmission electron microscopy (TEM). In dormant spores, the OSW was visible as a homogeneous electron-dense multilayered structure, about 15–20 nm thick. This thickness remained nearly constant throughout development (data not shown). Yet, we noted that the OSW often appeared wrinkled at early stages and flatter at later stages (Figures 3A and S4A), suggesting that these wrinkles may unfold as a result of spore growth, without drastic remodeling of the OSW.

Interestingly, at timing corresponding to outgrowth, we observed a local rupture/dissolution of the OSW at the site of tip emergence (Figures 3B, 3C, and S4A). Rupture of the wall was only obvious in spores with an outgrowing tip, and we did not note major opening at earlier time points, or at sites away from the growth zone. At later time points, the OSW appeared

to remain intact at the back of the outgrown cell (Figure S4A). By contrast, the inner cell wall appeared to be continuous with the emerging vegetative cell wall. To monitor the opening of the OSW in live spores, we grew spores in medium supplemented with an inner/vegetative wall digestion enzyme mix, which rapidly causes the death of outgrown spores and vegetative cells but does not affect spores protected by an intact OSW (Figure S4B). Spores developed normally in the enzyme mix and abruptly died at a volume ratio of $< V_{OSW\ opening}/V_G > = 1.97 \pm 0.22$ (n = 24) (Figures 3D and S4B), suggesting that the OSW opens when spores have doubled their volume. Thus, outgrowth is concomitant with a singular rupture in the OSW at the site of polar tube emergence.

The Outer Spore Wall Is Very Stiff and May Hinder Growth

To understand how the OSW may influence spore development, and how it may rupture at outgrowth, we assessed its mechanical properties using cellular stress-strain experiments (Figures 3E and S4C). This assay consists in applying a dose-dependent negative osmotic pressure by rinsing cells placed in microfluidic chambers with different concentrations of sorbitol and measuring the consequent changes in local curvature (see Experimental Procedures) (Misra et al., 2013). This assay showed that the OSW behaves as an elastic material whose surface modulus is approximately 2.3 times larger than that of the inner cell wall, yielding a bulk modulus 30 times larger (Figures 3E and 3F; Experimental Procedures). These properties remained nearly constant even after rupture (Figure 3F). Thus, the OSW is much stiffer than the inner/vegetative cell wall.

The presence of this rigid structure encasing the spore may influence growth, by reducing the effective stress generated by internal turgor pressure on the remodeling inner wall (Minc et al., 2009a). To test this, we reduced turgor by changing external osmolarity in a *gpd1Δ* mutant, which impairs osmoadaptation and found that this led to a significant reduction in growth rate, suggesting that growth in spores is powered by internal turgor as in vegetative cells (Minc et al., 2009a) (Figure 3G). We note that the simplest model for pressure-driven growth in walled cells predicts that growth rates are proportional to the surface modulus of the wall (Minc et al., 2009a). The changes in growth rate at outgrowth (increase by a factor 2.4; Figure S1B) are indeed comparable to the ratio between OSW and inner/vegetative cell-wall surface moduli ($\sigma_o/\sigma_i \approx 2.3$). Thus, these data suggest that the OSW may act as a mechanical barrier that slows down growth.

A Computational Model Reproduces Spore Morphogenesis and Predicts Variations in Outgrowth Onset with Changes in Wall Mechanics

Because the OSW is not majorly remodeled during spore development and behaves as an elastic material, it may accumulate elastic strain (equivalently mechanical stress) as the spore volume increases. As for most materials, the OSW may rupture if this strain exceeds a threshold that corresponds to the local failure stress (also known as ultimate strength of the material), and the volume increase needed to rupture it at outgrowth may relate to this threshold in strain (Figure 4A). To test this hypothesis, we developed numerical simulations of growing spores, using the following assumptions: (1) growth is powered by turgor pressure, (2) the inner wall is viscoelastic over the polarity cap because of remodeling, and elastic outside the cap (Minc et al., 2009a), (3) the OSW is elastic but may rupture when elastic strain (equivalently mechanical stress) exceeds a threshold, and (4) the cap center undergoes a random walk, which we use as a proxy for cap wandering by successive assembly/disassembly (Figure 4A; Supplemental Model). In simulations, we observed that spores remained roughly spherical until the OSW ruptured at a specific location, after which a polar tube began to elongate (Figures 4B and S5A; Movies S6 and S8). Starting from various initial conditions (n = 50 simulations), we found that the OSW ruptured when the ratio of spore volume to initial volume exceeded a well-defined threshold, thus reproducing experimental behavior (Figure 4C). In the model, this outgrowth threshold increased with the elastic strain (equivalently mechanical stress) threshold for OSW rupture and with the ratio of elastic moduli between OSW and inner wall (Figures 4D and S5B).

Mutants with Defective Spore Wall Hasten Outgrowth

A direct prediction of this mechanical model is that spores with defective spore wall structure or mechanical properties should outgrow at smaller volume ratio than wild-type spores. To test these aspects, we characterized spore wall mechanics and spore development in two mutants specifically defective in spore wall synthesis: *mok13Δ*, a mutant in an α-glucan synthase (García et al., 2006) and *chs1Δ*, a mutant in a chitin synthase (Arellano et al., 2000). These mutants depicted a marked reduction in the surface modulus of the OSW but no major difference in inner wall mechanics (Figure 4E), and indeed did outgrow at volume ratios that were significantly lower than WT: $< V_O/ V_G > = 1.46 \pm 0.10$ (n = 58) for *mok13Δ* and $< V_O/ V_G > = 1.57 \pm 0.11$ (n = 36) for *chs1Δ* (Figure 4F). This suggests that OSW mechanical properties contribute to the timing of outgrowth.

A Single Polar Cap Is Required for Singular Rupture in the OSW

An additional prediction of the model is that the threshold for rupture at outgrowth is first attained at the polar cap location, because mechanical stress in the OSW is enhanced by local growth (Figure 4A). Accordingly, simulations predicted that the OSW should rupture at many sites if growth is diffuse and not restricted to a single cap (Figure 5A). To experimentally test this, we assayed spores of the *orb6-25* mutant, a mutant in the NDR kinase orb6p, which shuts off polarity establishment at a downstream level when grown at restrictive temperature (Das et al., 2009). These spores grew in a perfectly isotropic manner, with polarity factors diffusely distributed around the surface, and remained round many hours after the typical timing corresponding to WT outgrowth (Figures 5B and 5C). We then performed TEM at different time points and indeed observed that, 6 hr after germination, this mutant presented multiple sites of spore wall rupture (Figure 5D). The number and size of holes in the OSW increased over time, as in the simulations (Figures 5E and S5D). Initial opening of the OSW in this mutant appeared at a volume ratio of $< V_{OSW\ opening}/V_G > = 2.18 \pm 0.40$ (n = 24), slightly higher than WT (Figure S5C).

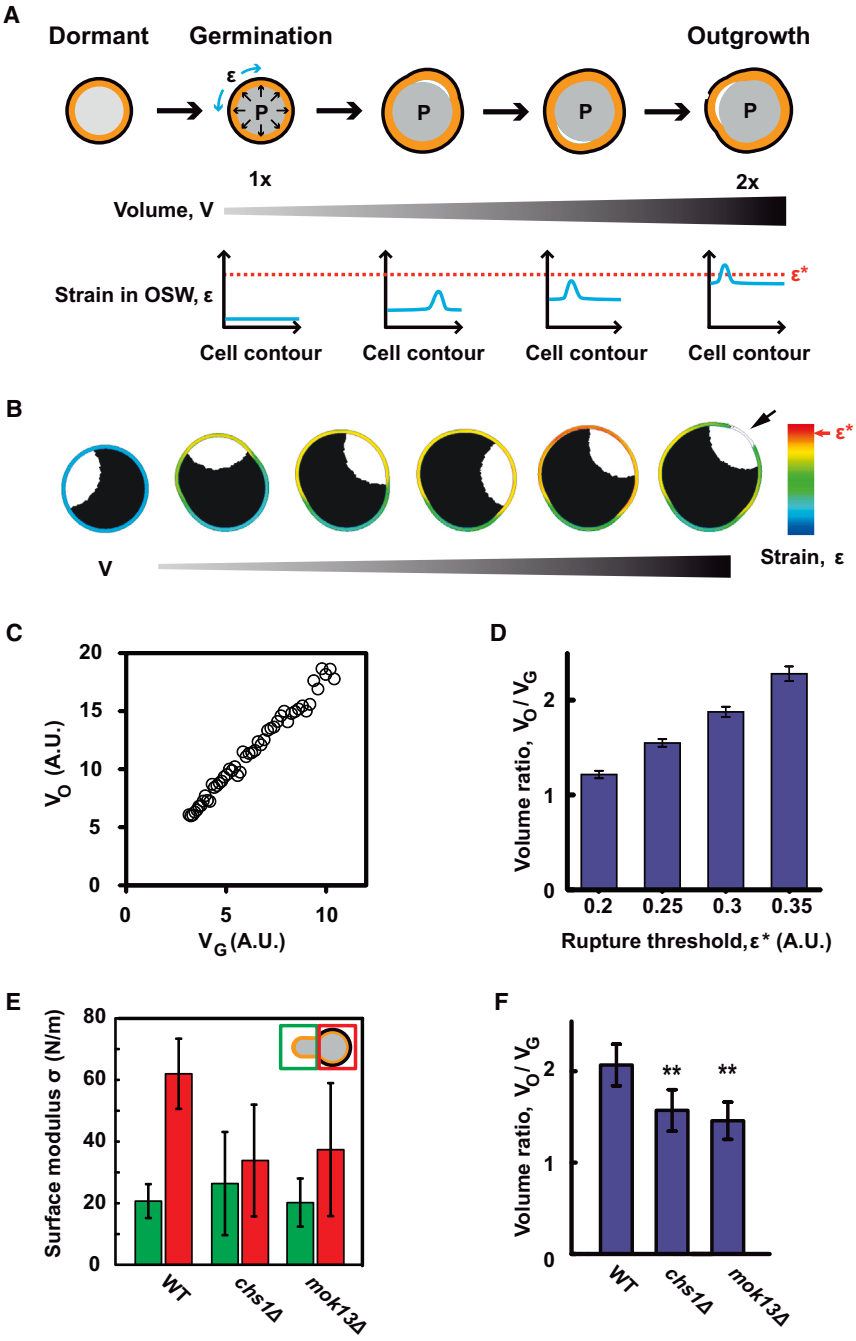

Figure 4. A Mechanical Model of Stress in the Outer Spore Wall Predicts Size-Increase Threshold for Wall Rupture and Outgrowth

(A) Schematic representing the geometry and inputs of the mechanical model. The spore grows under pressure, and is enclosed within the inner wall (orange) and the OSW (black). Growth is restricted to the polar cap. The OSW is under elastic strain ε, which increases globally as the spore grows, and locally at sites of polarized growth. The OSW ruptures above an elastic strain threshold ε^* corresponding to the failure stress of the material.

(B) Spores growing in silico. Colors in the OSW correspond to local strain values. Elastic moduli are assumed to be constant, and therefore the color code for strain also indicates the stress in the OSW.

(C) Theoretical prediction of volume doubling at outgrowth for a specific value of the threshold for rupture (n = 50 simulations).

(D) Dependence of volume ratio on the rupture threshold.

(E) Surface moduli for the walls on the spore (red bars) and cell (green bars) sides in outgrown spores of WT and *chs1Δ* and *mok13Δ* mutants (n > 10 spores for each condition).

(F) Volume ratios between outgrowth and germination for WT, *chs1Δ*, and *mok13Δ* mutants (n > 30 spores for each condition). Error bars represent SDs.

**p < 0.01, Student's t test. See also Figure S5 and Movie S6.

Thus, our mechanical model can predict both temporal and spatial rupture in the OSW at outgrowth and suggests a picture in which local growth at the cap locally increases the stress in the OSW until the failure stress is reached and the OSW ruptures (Figure 4A).

Local Laser-Induced Fragilization of the OSW Is Sufficient to Trigger Polar Cap Stabilization and Outgrowth

We next asked if the rupture in the OSW at outgrowth could influence polar cap stabilization. To directly assess this hypothesis, we developed a UV-laser assay to weaken the OSW with an intense pulse concentrated at a diffraction-limited spot on the spore surface. We optimized this assay to selectively weaken the OSW but not the inner wall (Figures S4B, S5E, and S5F; Experimental Procedures). We then filmed spores expressing GFP-bgs4 at early time points after germination and ablated the OSW either away from the polarity cap or at its exact location. Strikingly, the fragilization of the OSW at the cap caused it to stabilize and promoted the extension of a polarized tube at timings and volumes much smaller than in control nonablated spores in the same field of view (Figures 6A and 6B; Movie S7). Importantly, this effect was likely due to the mechanical fragilization of the OSW and not to a stress-activated recruitment or stabilization of polarity components (Kono et al., 2012). Spores ablated away from the cap did not show obvious recruitment at ablation sites and kept on wandering to stabilize at an independent location at similar timing and volumes as nonablated controls. These data suggest that the OSW has destabilizing effects on polarity, and that rupturing the OSW is sufficient to trigger cap stabilization and outgrowth.

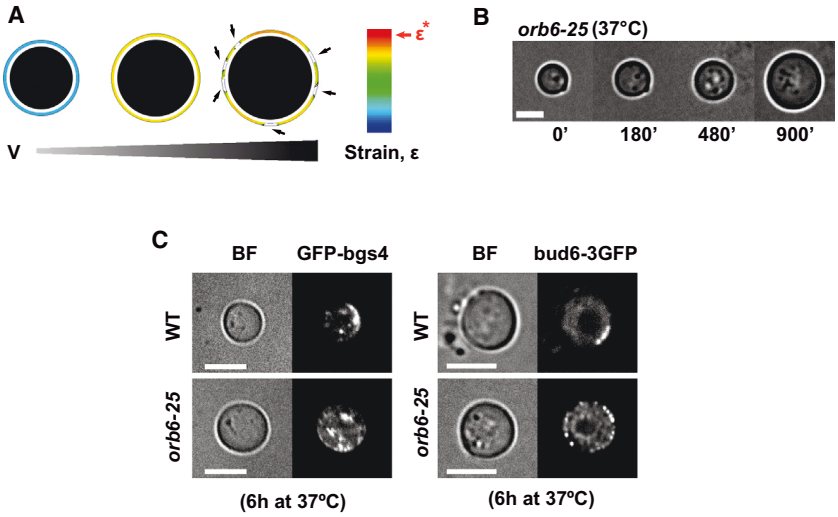

Figure 5. Polar Cap Assembly Is Required for Singular Rupture in the Spore Wall at Outgrowth

(A) Numerical simulations predicting multiple sites of rupture in spores with diffuse polarity.

(B) Time-lapse bright-field images of spore development in an *orb6-25* mutant grown at restrictive temperature (37°C) (scale bars, 5 μm).

(C) Single confocal midslices of WT and *orb6-25* spores expressing the polarity markers GFP-bgs4 or bud6-3GFP, 6 hr after germination at 37°C (scale bars, 5 μm).

(D) TEM of an *orb6-25* mutant spore 6 hr after germination at 37°C (scale bars, 1 μm) and close-up (scale bars, 200 nm). The black arrows point at sites of OSW ruptures.

(E) Quantification of phenotypes of OSW rupture at different times after germination at 37°C (n = 65 spores).

See also Figure S5.

growth while being preferentially stabilized at regions with higher surface growth rate.

DISCUSSION

By dynamically studying the developmental polarity and morphogenesis of single fission yeast spores, we develop and test here a simple quantitative model linking changes in the OSW with the spatial stability of polar caps needed for outgrowth. We propose that the OSW acts as a mechanical barrier, which hinders growth and destabilizes polarity. A rupture in this barrier generated by local polar growth when spores have grown enough releases inhibition by the OSW, stabilizes the cap, and coordinates spatial and temporal aspects of outgrowth. Instead of sensing absolute size (Turner et al., 2012), outgrowth appears to be triggered upon a fold change in volume. A function of this sensing system might be to prevent the reorganizing spores to exit the spore protective shell too early, as well as to regulate the timing and cell sizing at outgrowth in the absence of a tight cell-cycle regulation (Hatanaka and Shimoda, 2001). Through modeling and experimental tests, we demonstrate that a positive feedback between growth and polarity can account for a switch from unstable to stable polar cap behavior. Spatial landmarks from previous cell cycles, or MT-based targeting do not appear to be required at these early stages. MTs are also dispensable for de novo tip growth in rounded fission yeast spheroplasts or in mutants branching from cell sides (Kelly and Nurse, 2011; Sawin and Snaith, 2004). In addition, many cellular systems display transient oscillation of polar caps, which then stabilize at a fixed position even in the absence of directional cues (Bendezú and Martin, 2013; Dyer et al., 2013).

A Positive Feedback between Growth and Polarity Can Account for the Switch in Polar Cap Stability at Outgrowth

To understand how the changes in the OSW could impact changes in polarity behavior, we turned to our numerical simulations to assess different hypotheses of feedbacks on polarity. We biased the random walk of the polar cap toward a location determined by (1) minimal stress, (2) maximal curvature, or (3) maximal surface expansion rate. Although all three hypotheses seem to be qualitatively in agreement with experimental observations, we found that with hypothesis (1) the cap does not stop wandering, whereas with hypothesis (2) the tube is immediately curved. Only hypothesis (3) reproduced observations, yielding the most robust behavior after outgrowth (Figures 7A and 7B; Movie S8). These modeling results thus suggest that a feedback from surface growth on the position of the polarity cap can explain polar cap stabilization at outgrowth.

To experimentally validate this prediction, we halted growth either by depolymerizing actin with Latrunculin A or by confining the growth of single spores in round microchambers. In these experiments, the controls (spores treated with DMSO or in large microchambers) displayed cap wandering and then stabilized, whereas the caps in nongrowing spores kept on wandering for several hours passed the timing of outgrowth in the control, exhibiting a marked increase in the number of unstable caps (Figures 7C and 7D). Thus, growth is required for cap stabilization. Furthermore, the coordinated OSW rupture and cap stabilization at outgrowth may be accounted for by a positive-feedback loop between growth and polarity, in which the cap promotes local

Polarity Cap Oscillations

The initial polarity cap establishment in these spores is likely to involve an interplay between reaction-diffusion-based positive and negative feedbacks that promote the self-assembly of a

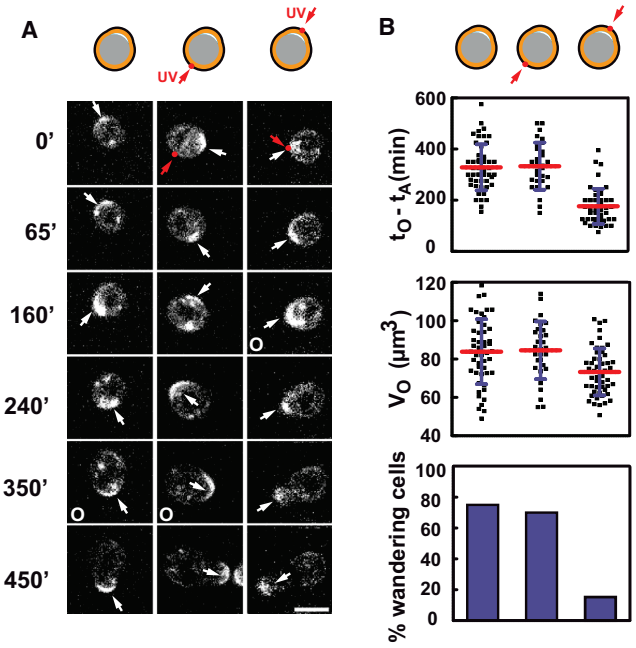

Figure 6. Rupturing the Outer Spore Wall Is Sufficient to Spatially Stabilize the Polar Cap

(A) Time-lapse single confocal midslices of germinating spores expressing GFP-bgs4 in the following conditions: not photoablated, photoablated away from the cap, and photoablated at the cap location with a UV laser. White arrows point at polar cap positions, and red arrows and dots indicate the photoablation site.

(B) Time of outgrowth with reference to laser irradiation, absolute volume at outgrowth, and percentage of spores depicting cap oscillations in the 2 hr following laser irradiation for the same three conditions as in (A).

Red bars: mean values; blue bars: SDs. Scale bars, 5 μm. See also Figure S5 and Movie S7.

single front of active-cdc42p (Bendezú and Martin, 2012; Das et al., 2012; Wu and Lew, 2013). We found that actin-based transport was not required in spores, although we note that actin inhibition caused a reduction in cap size (Figure S3B). The observed cap oscillations could be by-products of intrinsic mechanisms of polarization systems (Bendezú and Martin, 2012; Wu and Lew, 2013). Alternatively, they may function as a search mechanism when polarity needs to be redirected (Bendezú and Martin, 2013). In spores, the stochastic wandering of the cap could serve to identify a "weak spot" in the spore wall. Although our inspection of electron microscopy images of the OSW in fission yeast did not reveal obvious opening in the OSW in dormant spores (Figures 3A and S4A), certain fungal species display germ pores, which are small defects in the OSW from which the polar tube may emerge (Walkinshaw et al., 1967). Similarly, pollen tubes exit from specific apertures in the walls of pollen grains (Furness and Rudall, 2004) and early embryos of the marine brown algae *Fucus* use cues from the cell wall for polarity and outgrowth (Quatrano and Shaw, 1997). Our mechanism, whereby polar cap stability is amplified by growth, could serve to explain how these cells may polarize using mechanical cues from the cell wall.

Crosstalks between Growth and Polarity

Our work directly evidences the requirement of growth to spatially stabilize a polarity front. Similar growth-polarity feedbacks have been recently proposed in plants to regulate auxin-driven patterning of the shoot apex (Nakayama et al., 2012). Different tip-growing walled cells display variation in elongation rate that can range over almost two orders of magnitude (Knechtle et al., 2003; Qin and Yang, 2011). It is thus plausible that they have evolved mechanisms to monitor growth rate and link it to polarity machineries. A failure to do so could yield deleterious variations in cell-wall thickness and risks of cell death by bursting, or growth arrest (Campàs and Mahadevan, 2009). These growth-polarity feedbacks may underlie switching behavior such as oscillatory growth and contact sensing seen in fungal hyphae and pollen tubes (Kumamoto and Vinces, 2005; Qin and Yang, 2011; Rojas et al., 2011). Recent work in *S. cerevisiae* suggests models by which transport and fusion of vesicles may dilute polarity caps thereby causing them to disassemble (Layton et al., 2011). A reduction of surface expansion rate would yield similar dilution effects at a constant vesicle flux, and destabilize polarity. Conversely, the constraining effect of the OSW on surface expansion could restrict the available space needed for sufficient new membrane or inner wall addition necessary to stabilize the polar cap. In addition, we speculate that growth rates could impact polarity stability through a differential monitoring of cellular dimensions by intracellular gradients (Howard, 2012; Moseley and Nurse, 2010). Further work will be needed to fully characterize complex interplays between these essential morphogenetic cellular parameters.

Mechanochemical Coupling in Cell Polarity

Our data in conjunction with others support the existence of self-organizing processes coupling surface mechanics, growth, and internal organization. In animal cells, the micromechanical property of the actin cortex has been proposed to act as an important element to control polarity and shape changes during migration or cytokinesis (Paluch et al., 2006; Salbreux et al., 2012; Sedzinski et al., 2011). In addition, recent studies in migrating neutrophils suggest that membrane tension may have global inhibitory effects on polarity that function to maintain a singular active domain at the cell front (Houk et al., 2012). Thus, our work adds to a growing appreciation of mechanochemical feedbacks that serve to pattern cell shape and polarity (Asnacios and Hamant, 2012; Howard et al., 2011). The steady-state morphogenesis of a cell, like the rod shape of fission yeast, is likely to involve many types of feedbacks (Minc et al., 2009b; Terenna et al., 2008), which cannot be dissected with genetics. Thus, in addition to large-scale studies of gene products regulating cell shape and polarity (Hayles et al., 2013), dynamic studies like the one we performed here promise to pave the way for integrated models of morphogenesis.

EXPERIMENTAL PROCEDURES

Yeast Strains, Media, and Genetic Methods

Standard methods for *S. pombe* media and genetic manipulations were used (http://www-bcf.usc.edu/~forsburg/). Strains used in this study are

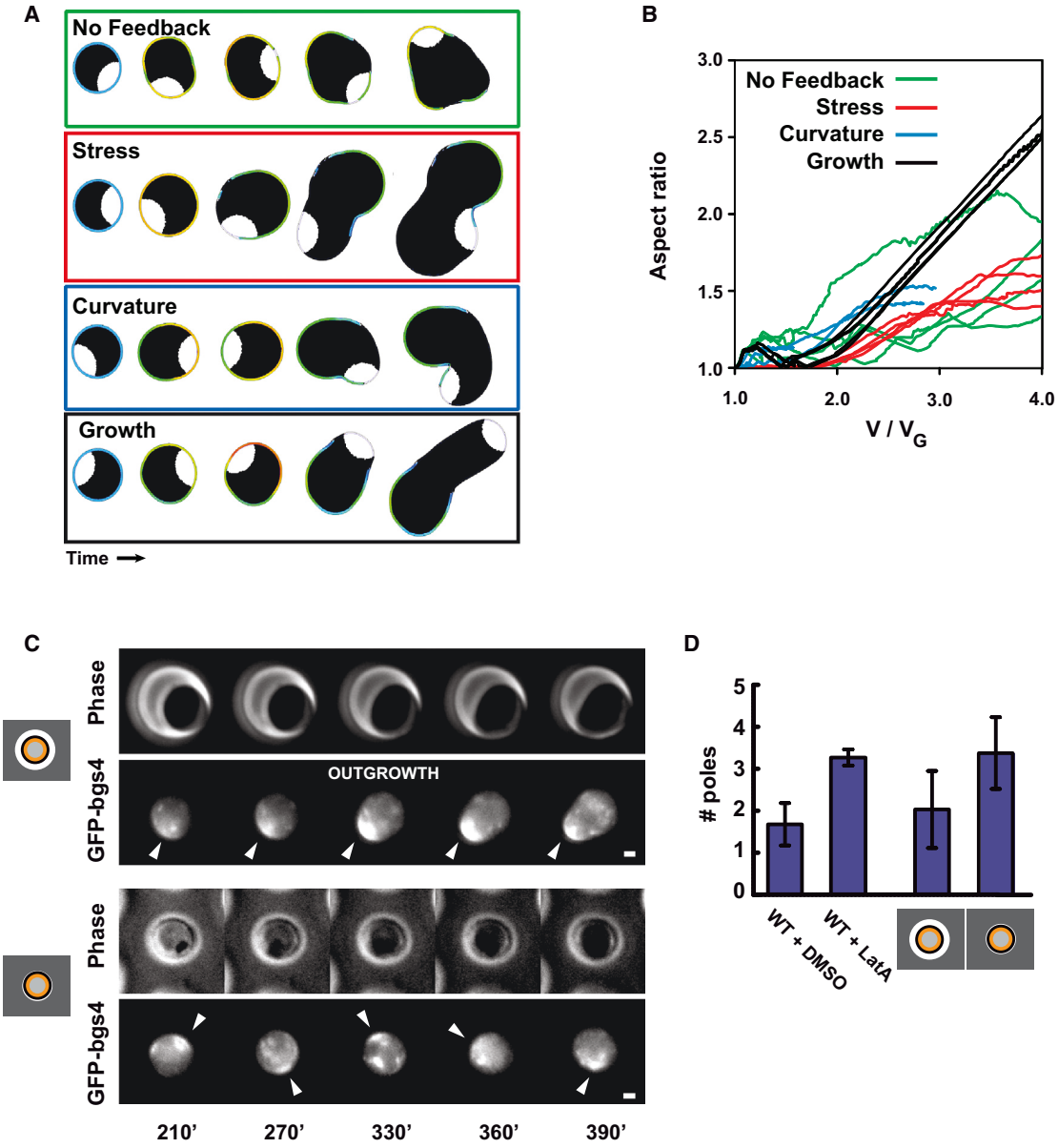

Figure 7. Outgrowth Involves a Positive-Feedback Loop between Growth and Polarity

(A) Numerical simulations testing different sources of feedback for polarity stabilization at outgrowth: no feedback, feedback on minimal mechanical stress, feedback on maximal curvature, feedback on maximal surface expansion rate (growth).

(B) Model prediction for the evolution of the aspect ratio as a function of normalized volume in the same conditions as in (A).

(C) Epifluorescence time-lapse of germinating spores expressing GFP-bgs4 arising from the same population, placed in large (on top) or small confining (on bottom) PDMS microchambers. White arrows point at successive polarity cap positions.

(D) Total number of observed successive polar caps for spores expressing CRIB-GFP treated with DMSO or 100 μM of Latrunculin A, which halts growth, and for spores expressing GFP-bgs4 in large or confining microchambers (n > 15 spores for each condition). Error bars represent SDs.

Scale bars, 1 μm. See also Movie S8.

listed in Table S1. Spores were obtained from homothallic h90 strains, or from diploids when indicated. Freshly growing cells were sporulated on malt extract (ME) solid media for 3 days. Spores were then digested 1 hr at room temperature in 1/200 glusulase solution in water to kill vegetative cells, and the enzyme was washed out three times in water. Digestion with glusulase did not influence morphogenetic and polarity events (size sensing and cap wandering) described in the manuscript (data not shown).

Pharmacological Inhibitors

Methyl-2-benzimidazole carbamate (MBC, Sigma) was used at a final concentration of 50 μg/ml from a 100× stock solution made fresh in DMSO. Latrunculin A (LatA, Sigma) was used at a final concentration of 100 μM from a 100× stock in DMSO. The efficiency of these treatments in rapidly depolymerizing microtubules and actin, respectively, was assessed by treating a mixed population of spores and cells for 10 min and imaging atb2-GFP for microtubules and the actin patch marker crn1-GFP (Figures S3C and S3D).

Microscopy

For long-term imaging, spores in water solution were placed on 2% agar YE5S pads and covered with a coverslip. For some applications, spores were placed in microfluidic chambers between a dialysis membrane and a coverslip, which allowed live fluid exchange (Charvin et al., 2008). Spore development was imaged at room temperature (23°C–25°C), with controlled humidity, with an inverted epifluorescence microscope provided with a motorized stage and automatic focus (Nikon Ti-Eclipse), and an EM-CCD camera (Hamamatsu). Movies were generally acquired at 100× magnification with 5 or 10 min time intervals, using phase contrast and epifluorescence when necessary. GFP-tagged polarity markers were also imaged with a spinning-disk confocal fluorescent microscope (Yokagawa, CSU-X1 spinning head) equipped with an EM-CCD camera (Evolve, Photometrics) and a 100× oil immersion objective (Nikon S Fluor 100× 0.5–1.3 NA). Images were acquired with Micromanager or Metamorph and processed and analyzed with Image J and MATLAB (MathWorks).

Image Analysis

Morphogenetic parameters of single developing spores were extracted from phase-contrast time-lapses using home-built MATLAB scripts (available upon request). Cell contours were segmented from the phase images, at each time point and oriented along the future outgrowth axis, yielding the morphogenesis color plots depicted in Figure 1B. The precision in contour segmentation was calibrated using spores expressing a plasma membrane marker GFP-psy1. The long axis was identified at each time point, and the aspect ratio was computed as the ratio between the length along this axis and the largest perpendicular diameter. Volumes were computed by assuming a prolate geometry (rotational symmetry around the long axis of the cell). The long axis was thus sliced in local diameters y(x) every pixel (Figure 1B, inset) which served to compute the areas of the sections of the prolate $S(x) = \pi^*(y(x)/2)^2$, and the volume was computed as the sum of these areas along all the pixels of the long axis. We estimate imprecisions associated to these methods (including errors in the z, segmentation, and prolate approximation), to be lower than 5% for length and aspect ratio and on the order of 10% for the volume.

The frequency of new caps during the initial phase of near-isotropic growth (Figures 2C and 2E) was visually quantified from time-lapse epifluorescence movies of cells expressing GFP-bgs4. Only fully reassembling new caps were counted, and the number of caps was divided by the time between first cap appearance and outgrowth. The last stable cap-promoting outgrowth was not counted.

Quantification of relative concentration evolution of polarity factors at the cap (Figure 2F) was inferred from computing the mean signal at the polar cap from a merged confocal stack of six z-sections time-lapsed on individual spores. Growing spores were imaged together with vegetative cells, to normalize the concentration in spore caps with the concentration in vegetative bipolar caps. Photobleaching was accounted for by quantifying the loss of signal in fixed cells expressing the same marker, and autofluorescence was accounted for by imaging WT spores and cells with no marker.

Transmission Electron Microscopy

Wild-type spores were grown in liquid YE5S at 30°C for different amounts of time and subsequently fixed in 2% glutaraldehyde in YE5S for 30 min on ice. *orb6-25* mutants spores were grown at 37°C for different amounts of times and fixed in same conditions. Spores were then transferred to 0.1 M PBS + 2% glutaraldehyde and stirred overnight at 4°C. The spore pellet was then dehydrated in ethanol and embedded in Epon resine. Ultrathin sections were made with an ultramicrotome (Leica), deposited onto electron microscopy grids, and contrasted with uranyl acetate in lead citrate. Images were taken using a FEI CM120 electron microscope (FEI Company), equipped with a numeric camera (Keen View; Soft Imaging System, SIS).

Laser Ablation of the Outer Spore Wall

The laser ablation assay uses a pulsed 355 nm ultraviolet laser interfaced with an iLas system (Roper Scientific) in the "Mosquito" mode. This allows irradiating at multiple positions in the field with laser spots having a fixed area of about 500 nm. This system is mounted on a confocal spinning disk (Yokagawa CSU-X1 spinning head on a Nikon Eclipse Ti inverted microscope) equipped with an EM-CCD camera (Evolve, Photometrics) and a 100× oil immersion objective (Nikon S Fluor 100× 0.5–1.3 NA). We calibrated the irradiation time to optimize the selectivity of the assay in fragilizing the spore wall but not the inner wall. To this aim, spores were placed in microfluidic flow chambers, irradiated, and subsequently rinsed with a mix of two vegetative cell-wall (inner wall) digestion enzymes (0.5 mg/ml Zymolase and 10 mg/ml Novozyme). Rinsing with these enzymes yields the death of all vegetative cells and outgrown spores in 10–30 min but does not affect spores (Figure S4B). Using this assay, we identified the laser time of exposure that did not yield spore death without enzyme treatment, but that yielded death of irradiated spores after enzyme treatment. The optimal exposure time in our conditions was found to be 80 ms. The photoablation assay as presented in Figure 6 was then performed in these same conditions on spores expressing the polarity marker GFP-bgs4, that were germinated in YE5S liquid for 3 hr before laser irradiation.

Stress-Strain Experiment to Measure Rigidity of the OSW and Inner Cell Wall

To compute surface moduli of cell walls, spores, outgrown spores, and vegetative cells were placed in microfluidic chambers in YE5S media. The media was then exchanged rapidly and replaced by YE5S with a given concentration of sorbitol. This created a relative change in the internal osmotic pressure computed as $\Delta p = C_s RT$, with C_s the sorbitol concentration, R the gas constant, and T the temperature. This change in osmolarity caused the spores and cells to shrink, which serves as a measure of strain. Local changes in curvature radii, r, (before and 5 min after treatment) were tracked using homemade MATLAB scripts (Figure 3E). This assay was then repeated with dose-dependent addition of sorbitol (C_s = 2 M, 1.5 M, 1 M, 0.5 M), which allowed us to derive a stress-strain curve (Figure S4C). This curve was found to be linear within the regime probed, which reflects elastic behavior of both inner and outer spore wall, on short timescales. The slopes were then extracted to compute the average surface moduli of spores, using the following formula:

$$\frac{\Delta P}{\Delta r} = 4\frac{\sigma}{r^2}$$

This assay was used to derive average surface moduli of spores, vegetative cells, the back of outgrown spores (where the OSW is still encasing the inner wall) and the tip of outgrown spores (which only have vegetative wall) (Figure 3E). In vegetative cells, this analysis led to a value of the surface modulus of the cell wall of $\sigma_{Veg} = 18.6\ N.m^{-1}$, which closely agrees with measurement achieved by other means (Minc et al., 2009a). The surface modulus of the back of the spores was found to be $\sigma_{back} = 62.0\ N.m^{-1}$, and the surface modulus at the tip of the emerging tube was very close to the vegetative value: $\sigma_{tip} = 20.6\ N.m^{-1}$. Because the back of the spore has superimposed inner and outer wall, $\sigma_{back} = \sigma_i + \sigma_o$, whereas $\sigma_{tip} = \sigma_i$. Thus, the ratio between the surface moduli of the outer and the inner wall can be computed from $\sigma_o/\sigma_i = \sigma_{back}/\sigma_{tip} - 1 \approx 2.3$. Because the thickness, h_0, of the outer wall is approximately 15 nm and the thickness of the inner wall, h_i, is around 200 nm, the ratio in bulk moduli $E_o/E_i = (h_O\sigma_o)/(h_i\sigma_i)$ is around 30. The same assay and analysis were then used to characterize rigidity of spore walls in *chs1Δ* and *mok13Δ* mutants defective in spore wall synthesis (Figure 4E).

Assessment of the Role of Turgor Pressure in Spore Growth

Spores of either WT or *gpd1Δ* were first germinated and grown at 30°C for 2 hr in liquid YE5S. Spores were then placed in microfluidic chambers and covered with a semipermeable dialysis membrane. Single spore growth rates were monitored from time-lapse imaging during 2 hr, after which the spores were rinsed with 1 M sorbitol to decrease internal turgor, and growth rates were measured again for another 2 hr. Growth rate ratio before and after treatment was then computed for each single spore and averaged to plot the bar graph presented in Figure 3F.

Microchambers Operation

Microchambers were fabricated by the use of standard soft-lithography methods (Minc et al., 2009a, 2009b). Chambers are round, are 3–4 μm deep, and have diameters varying between 3 and 10 μm. Spores expressing the polarity marker GFP-bgs4 were germinated and grown for 3 hr 30 min, and a

1 μl drop of spore suspension was then placed at the bottom of a round fluorodish (WPI). The polydimethylsiloxane (PDMS) block containing the chambers was activated with a plasma cleaner and subsequently placed, holes facing down, on top of the spores in the dish and let to bind to the glass bottom. This forced many spores into single microchambers, some constraining, and some much larger than the spore diameter, that were used as controls. Time-lapses at different positions were then recorded to monitor polar cap wandering in different conditions.

SUPPLEMENTAL INFORMATION

Supplemental Information includes supplemental model, five figures, one table, and eight movies and can be found with this article online at http://dx.doi.org/10.1016/j.devcel.2014.01.023.

ACKNOWLEDGMENTS

We thank the Coudreuse, Martin, Perez, Ribas, Valdivieso, Sanchez, Chang, Tran, and Paoletti labs for sharing strains and materials. D.B. was supported by an Institut Curie PhD fellowship in the initial period of this work. A.B. is supported by a European Research Council starting grant (PhyMorph, #307387). N.M. acknowledges support from CNRS, FP7 (CIG and ITN programs), ANR (grant 10PDOC00301), FRM (grant AJE20130426890), and a Mairie de Paris "Emergence grant."

Received: September 24, 2013
Revised: January 6, 2014
Accepted: January 23, 2014
Published: March 10, 2014

REFERENCES

Arellano, M., Cartagena-Lirola, H., Nasser Hajibagheri, M.A., Durán, A., and Henar Valdivieso, M. (2000). Proper ascospore maturation requires the chs1+ chitin synthase gene in Schizosaccharomyces pombe. Mol. Microbiol. *35*, 79–89.

Asnacios, A., and Hamant, O. (2012). The mechanics behind cell polarity. Trends Cell Biol. *22*, 584–591.

Bastmeyer, M., Deising, H.B., and Bechinger, C. (2002). Force exertion in fungal infection. Annu. Rev. Biophys. Biomol. Struct. *31*, 321–341.

Bendezú, F.O., and Martin, S.G. (2012). Cdc42 oscillations in yeasts. Sci. Signal. *5*, pe53.

Bendezú, F.O., and Martin, S.G. (2013). Cdc42 explores the cell periphery for mate selection in fission yeast. Curr. Biol. *23*, 42–47.

Boudaoud, A. (2003). Growth of walled cells: from shells to vesicles. Phys. Rev. Lett. *91*, 018104.

Campàs, O., and Mahadevan, L. (2009). Shape and dynamics of tip-growing cells. Curr. Biol. *19*, 2102–2107.

Cano, R.J., and Borucki, M.K. (1995). Revival and identification of bacterial spores in 25- to 40-million-year-old Dominican amber. Science *268*, 1060–1064.

Chang, F., and Martin, S.G. (2009). Shaping fission yeast with microtubules. Cold Spring Harb. Perspect. Biol. *1*, a001347.

Charvin, G., Cross, F.R., and Siggia, E.D. (2008). A microfluidic device for temporally controlled gene expression and long-term fluorescent imaging in unperturbed dividing yeast cells. PLoS ONE *3*, e1468.

Cortés, J.C., Carnero, E., Ishiguro, J., Sánchez, Y., Durán, A., and Ribas, J.C. (2005). The novel fission yeast (1,3)beta-D-glucan synthase catalytic subunit Bgs4p is essential during both cytokinesis and polarized growth. J. Cell Sci. *118*, 157–174.

Das, M., Wiley, D.J., Medina, S., Vincent, H.A., Larrea, M., Oriolo, A., and Verde, F. (2007). Regulation of cell diameter, For3p localization, and cell symmetry by fission yeast Rho-GAP Rga4p. Mol. Biol. Cell *18*, 2090–2101.

Das, M., Wiley, D.J., Chen, X., Shah, K., and Verde, F. (2009). The conserved NDR kinase Orb6 controls polarized cell growth by spatial regulation of the small GTPase Cdc42. Curr. Biol. *19*, 1314–1319.

Das, M., Drake, T., Wiley, D.J., Buchwald, P., Vavylonis, D., and Verde, F. (2012). Oscillatory dynamics of Cdc42 GTPase in the control of polarized growth. Science *337*, 239–243.

Drubin, D.G. (1991). Development of cell polarity in budding yeast. Cell *65*, 1093–1096.

Dyer, J.M., Savage, N.S., Jin, M., Zyla, T.R., Elston, T.C., and Lew, D.J. (2013). Tracking shallow chemical gradients by actin-driven wandering of the polarization site. Curr. Biol. *23*, 32–41.

Fink, J., Carpi, N., Betz, T., Bétard, A., Chebah, M., Azioune, A., Bornens, M., Sykes, C., Fetler, L., Cuvelier, D., and Piel, M. (2011). External forces control mitotic spindle positioning. Nat. Cell Biol. *13*, 771–778.

Furness, C.A., and Rudall, P.J. (2004). Pollen aperture evolution—a crucial factor for eudicot success? Trends Plant Sci. *9*, 154–158.

García, I., Tajadura, V., Martín, V., Toda, T., and Sánchez, Y. (2006). Synthesis of alpha-glucans in fission yeast spores is carried out by three alpha-glucan synthase paralogues, Mok12p, Mok13p and Mok14p. Mol. Microbiol. *59*, 836–853.

Glynn, J.M., Lustig, R.J., Berlin, A., and Chang, F. (2001). Role of bud6p and tea1p in the interaction between actin and microtubules for the establishment of cell polarity in fission yeast. Curr. Biol. *11*, 836–845.

Harold, F.M. (1990). To shape a cell: an inquiry into the causes of morphogenesis of microorganisms. Microbiol. Rev. *54*, 381–431.

Hatanaka, M., and Shimoda, C. (2001). The cyclic AMP/PKA signal pathway is required for initiation of spore germination in Schizosaccharomyces pombe. Yeast *18*, 207–217.

Hayles, J., Wood, V., Jeffery, L., Hoe, K.L., Kim, D.U., Park, H.O., Salas-Pino, S., Heichinger, C., and Nurse, P. (2013). A genome-wide resource of cell cycle and cell shape genes of fission yeast. Open Biol. *3*, 130053.

Houk, A.R., Jilkine, A., Mejean, C.O., Boltyanskiy, R., Dufresne, E.R., Angenent, S.B., Altschuler, S.J., Wu, L.F., and Weiner, O.D. (2012). Membrane tension maintains cell polarity by confining signals to the leading edge during neutrophil migration. Cell *148*, 175–188.

Howard, M. (2012). How to build a robust intracellular concentration gradient. Trends Cell Biol. *22*, 311–317.

Howard, J., Grill, S.W., and Bois, J.S. (2011). Turing's next steps: the mechanochemical basis of morphogenesis. Nat. Rev. Mol. Cell Biol. *12*, 392–398.

Howell, A.S., Jin, M., Wu, C.F., Zyla, T.R., Elston, T.C., and Lew, D.J. (2012). Negative feedback enhances robustness in the yeast polarity establishment circuit. Cell *149*, 322–333.

Kelly, F.D., and Nurse, P. (2011). De novo growth zone formation from fission yeast spheroplasts. PLoS ONE *6*, e27977.

Klobutcher, L.A., Ragkousi, K., and Setlow, P. (2006). The Bacillus subtilis spore coat provides "eat resistance" during phagocytic predation by the protozoan Tetrahymena thermophila. Proc. Natl. Acad. Sci. USA *103*, 165–170.

Knechtle, P., Dietrich, F., and Philippsen, P. (2003). Maximal polar growth potential depends on the polarisome component AgSpa2 in the filamentous fungus Ashbya gossypii. Mol. Biol. Cell *14*, 4140–4154.

Kono, K., Matsunaga, R., Hirata, A., Suzuki, G., Abe, M., and Ohya, Y. (2005). Involvement of actin and polarisome in morphological change during spore germination of Saccharomyces cerevisiae. Yeast *22*, 129–139.

Kono, K., Saeki, Y., Yoshida, S., Tanaka, K., and Pellman, D. (2012). Proteasomal degradation resolves competition between cell polarization and cellular wound healing. Cell *150*, 151–164.

Kumamoto, C.A., and Vinces, M.D. (2005). Alternative Candida albicans lifestyles: growth on surfaces. Annu. Rev. Microbiol. *59*, 113–133.

Layton, A.T., Savage, N.S., Howell, A.S., Carroll, S.Y., Drubin, D.G., and Lew, D.J. (2011). Modeling vesicle traffic reveals unexpected consequences for Cdc42p-mediated polarity establishment. Curr. Biol. *21*, 184–194.

McKenney, P.T., Driks, A., and Eichenberger, P. (2013). The Bacillus subtilis endospore: assembly and functions of the multilayered coat. Nat. Rev. Microbiol. *11*, 33–44.

Minc, N., Boudaoud, A., and Chang, F. (2009a). Mechanical forces of fission yeast growth. Curr. Biol. *19*, 1096–1101.

Minc, N., Bratman, S.V., Basu, R., and Chang, F. (2009b). Establishing new sites of polarization by microtubules. Curr. Biol. *19*, 83–94.

Misra, G., Rojas, E.R., Gopinathan, A., and Huang, K.C. (2013). Mechanical consequences of cell-wall turnover in the elongation of a Gram-positive bacterium. Biophys. J. *104*, 2342–2352.

Mitchison, J.M., and Nurse, P. (1985). Growth in cell length in the fission yeast Schizosaccharomyces pombe. J. Cell Sci. *75*, 357–376.

Moseley, J.B., and Nurse, P. (2010). Cell division intersects with cell geometry. Cell *142*, 184–188.

Nakayama, N., Smith, R.S., Mandel, T., Robinson, S., Kimura, S., Boudaoud, A., and Kuhlemeier, C. (2012). Mechanical regulation of auxin-mediated growth. Curr. Biol. *22*, 1468–1476.

Neiman, A.M. (2005). Ascospore formation in the yeast Saccharomyces cerevisiae. Microbiol. Mol. Biol. Rev. *69*, 565–584.

Nurse, P., Thuriaux, P., and Nasmyth, K. (1976). Genetic control of the cell division cycle in the fission yeast Schizosaccharomyces pombe. Mol. Gen. Genet. *146*, 167–178.

Paluch, E., van der Gucht, J., and Sykes, C. (2006). Cracking up: symmetry breaking in cellular systems. J. Cell Biol. *175*, 687–692.

Pandey, R., Ter Beek, A., Vischer, N.O., Smelt, J.P., Brul, S., and Manders, E.M. (2013). Live cell imaging of germination and outgrowth of individual bacillus subtilis spores; the effect of heat stress quantitatively analyzed with SporeTracker. PLoS ONE *8*, e58972.

Qin, Y., and Yang, Z. (2011). Rapid tip growth: insights from pollen tubes. Semin. Cell Dev. Biol. *22*, 816–824.

Quatrano, R.S., and Shaw, S.L. (1997). Role of the cell wall in the determination of cell polarity and the plane of cell division in Fucus embryos. Trends Plant Sci. *2*, 15–21.

Rincón, S.A., Ye, Y., Villar-Tajadura, M.A., Santos, B., Martin, S.G., and Pérez, P. (2009). Pob1 participates in the Cdc42 regulation of fission yeast actin cytoskeleton. Mol. Biol. Cell *20*, 4390–4399.

Rojas, E.R., Hotton, S., and Dumais, J. (2011). Chemically mediated mechanical expansion of the pollen tube cell wall. Biophys. J. *101*, 1844–1853.

Salbreux, G., Charras, G., and Paluch, E. (2012). Actin cortex mechanics and cellular morphogenesis. Trends Cell Biol. *22*, 536–545.

Sawin, K.E., and Snaith, H.A. (2004). Role of microtubules and tea1p in establishment and maintenance of fission yeast cell polarity. J. Cell Sci. *117*, 689–700.

Sedzinski, J., Biro, M., Oswald, A., Tinevez, J.Y., Salbreux, G., and Paluch, E. (2011). Polar actomyosin contractility destabilizes the position of the cytokinetic furrow. Nature *476*, 462–466.

Slaughter, B., and Li, R. (2006). Toward a molecular interpretation of the surface stress theory for yeast morphogenesis. Curr. Opin. Cell Biol. *18*, 47–53.

Tanaka, K., and Hirata, A. (1982). Ascospore development in the fission yeasts Schizosaccharomyces pombe and S. japonicus. J. Cell Sci. *56*, 263–279.

Tatebe, H., Nakano, K., Maximo, R., and Shiozaki, K. (2008). Pom1 DYRK regulates localization of the Rga4 GAP to ensure bipolar activation of Cdc42 in fission yeast. Curr. Biol. *18*, 322–330.

Terenna, C.R., Makushok, T., Velve-Casquillas, G., Baigl, D., Chen, Y., Bornens, M., Paoletti, A., Piel, M., and Tran, P.T. (2008). Physical mechanisms redirecting cell polarity and cell shape in fission yeast. Curr. Biol. *18*, 1748–1753.

Turner, J.J., Ewald, J.C., and Skotheim, J.M. (2012). Cell size control in yeast. Curr. Biol. *22*, R350–R359.

Walkinshaw, C.H., Hyde, J.M., and van Zandt, J. (1967). Fine structure of quiescent and germinating aeciospores of Cronartium fusiforme. J. Bacteriol. *94*, 245–254.

Wallace, S., Fleming, A., Wellman, C.H., and Beerling, D.J. (2011). Evolutionary development of the plant and spore wall. AoB Plants *2011*, plr027.

Wedlich-Soldner, R., Altschuler, S., Wu, L., and Li, R. (2003). Spontaneous cell polarization through actomyosin-based delivery of the Cdc42 GTPase. Science *299*, 1231–1235.

Wu, C.F., and Lew, D.J. (2013). Beyond symmetry-breaking: competition and negative feedback in GTPase regulation. Trends Cell Biol. *23*, 476–483.

Developmental Cell, Volume *28*

Supplemental Information

Symmetry Breaking in Spore Germination

Relies on an Interplay between Polar

Cap Stability and Spore Wall Mechanics

Daria Bonazzi, Jean-Daniel Julien, Maryse Romao, Rima Seddiki, Matthieu Piel, Arezki Boudaoud, and Nicolas Minc

SUPPLEMENTAL MODEL

The simulations presented in Figures 4,5 and 7 were obtained based on a mechanical model of the growing spore. We accounted for the following hypotheses: (i) growth is powered by turgor, (ii) the inner wall is viscoelastic over the polarity cap because of inner wall remodeling, and elastic outside the cap, (iii) the OSW is elastic but may rupture when elastic strain (equivalently stress) exceeds a threshold, and (iv) the cap center undergoes a walk that is either fully random or biased by specific feedbacks (see below). To easily explore model parameters, we considered a 2D model where a disc of inner wall is initially surrounded by a thin annulus of OSW. In the figures and supplementary movies presented throughout the manuscript, the OSW and the inner wall are superimposed, but have different colors: the OSW is depicted as an opaque colored layer (in which the colors correspond to local values of the strain in the OSW), while the inner wall is shown in white over the polar cap (the growing region) and in black outside of the cap. The initial state in the simulation assumes that both the inner and outer cell walls are homogeneously stressed by internal pressure. To allow the system to grow at the polar cap where the inner cell wall is being remodeled, we assume that this wall behaves as a viscoelastic material whose viscosity is infinite outside the polar cap and finite at the cap. The OSW is on the other hand supposed to behave as a purely elastic, brittle material that breaks when the elastic strain exceeds a fixed threshold ε^*. Above this strain, the OSW can then deform plastically.

The simulations consist of iterative loops; the strain and the position of the polarity cap are computed at each iteration. The polarity cap width is set to a fixed value. In the first set of simulations (Figure 4), the center of the polarity cap is assumed to follow a random walk, of a step length chosen to match the observed frequency of new caps (Figure 2C). In the second set of simulations (Figure 7), the polarity cap was moved according to one of the specific hypotheses of feedback, (i) to the position of maximal curvature (assuming the existence of putative curvature sensors), (ii) to the position of minimal stress (assuming the existence of putative stress sensors, like stretch activated ion channels for instance), or (iii) to the position of maximal growth rate; in this second set, a small noise on polar cap location was added to prevent the simulations from being deterministic. The minimal input parameters needed for the default model, as presented in Figure 4 are thus: the normalized radius of the polar cap r^*, the characteristic time of the random walk, t^*, the normalized Young's modulus of the OSW E_0^*, the normalized Young's modulus of the inner wall Ei^* (the pressure P^* is set as a unit),

the viscosity η of growing regions of the inner wall, the rupture strain threshold of the OSW ε*, which corresponds to the failure stress through the constitutive relation. For prediction of rupture in the OSW, the parameters r* and t* do not influence predictions; the viscosity η influences the absolute timing but not the sizes and morphologies; finally the parameters ε* and the ratio E_0*/Ei* have a strong influence (Figure 4D and Figure S5B).

More specifically, we assumed the cell wall to be viscoelastic, and modeled it as an isotropic Maxwell material. By separating the plastic ε_p and elastic ε_{el} parts of the strain tensor ε, we write:

$$\frac{d\boldsymbol{\epsilon}}{dt} = \frac{d\boldsymbol{\epsilon_p}}{dt} + \frac{d\boldsymbol{\epsilon_{el}}}{dt} = \frac{\boldsymbol{\sigma}}{\eta} + \frac{1}{E}\frac{d\boldsymbol{\sigma}}{dt}$$

where σ is the stress tensor, η the viscosity and E the young modulus of the material. Here, the characteristic timescale of the material, η/E, is assumed to take two values: infinity where no growth occurs, and a constant finite value where growth occurs; this finite value sets the unit of time in the simulations. At each time step, the stress due to internal pressure is computed by solving the stationary Cauchy momentum equation:

$$div(\boldsymbol{\sigma}) = f$$

where f is the body force due to internal pressure. The Hooke's law gives the relationship between the strain tensor and the stress tensor:

$$\boldsymbol{\sigma} = \frac{E\nu}{(1+\nu)(1-2\nu)} tr(\boldsymbol{\epsilon_{el}})\boldsymbol{I} + \frac{E}{(1+\nu)}\boldsymbol{\epsilon_{el}}$$

where ν is the Poisson's ratio and I the identity tensor.

We employ an incremental and discrete approach to growth. After computing the elastic strain, the increment of plastic strain is equated with the elastic strain. In the limit of small strains, this is exactly equivalent to defining a Maxwell material for which the characteristic time scale, η/E, is equal to the time step of the simulation. The inner wall is viscoelastic in the domain corresponding to the polar cap and purely elastic outside of this domain. The OSW deforms elastically as long as the largest eigenvalue of the elastic strain ε is smaller than the threshold strain ε*. When and where this threshold is reached, the OSW is irreversibly ruptured, and then it is assumed to be viscoelastic. In the simulations, the spore is a disc of typical radius R*=1 and Young's modulus Ei* surrounded by an annulus of thickness R*/10 and Young's modulus Eo*. The polar cap is computed as a disc of radius r*=0.9R* whose

center is located on the boundary of the spore, unless for the simulation of Figure 5A where r*>>R*, to account for a diluted polarity.

To test hypothesis of polar cap stabilization from wall mechanics, we assess possible sources of positive feedback. Because the polar cap yields local growth, that results in reducing surface stress, increasing curvature and increasing surface expansion rates; we implement in the model a feedback so that at each time step, the polar cap moves to a new position determined by:
(o) a random walk of step time t*=30,
(i) the minimal value of stress σ,
(ii) the maximal value of curvature of the OSW,
(iii) or the maximal surface growth (computed as the normal velocity of the wall).
In order to avoid completely deterministic simulations with hypotheses (i-iii), an intrinsic white noise of amplitude 5% is added to the variable that defines the location of the polar cap; the value of this noise is unimportant as long as it is small.

Numerically, the elastic problem is solved with the finite elements method implemented in a FreeFem++ program. After each time step, the domain is re-meshed to keep a mesh size equal to 1/10 in the inner wall domain and 1/50 in OSW domain.

Values of parameters used in the model are:
- Ei*=14 in all simulations
- Eo*= 42 for simulations presented in Figures 4B, 4C, 4D, 5A, 7A, 7B and S5A, and $28<Eo^*<42$ for Figure S5B
- $\nu=0.3$ for all simulations;
- R*=1 for Figures 4B, 4D, 5A, 7A, 7B, S5A and S5B, and $0.8<R^*<1.2$ for Figure 4C
- $\varepsilon^*=0.3$ for Figures 4B, 4C, 5A, S5A and S5B, and $0.2<\varepsilon^*<0.35$for Figure 4D
- P*=1, for all simulation

DB_146	h90	wt	leu1-32 ura4-D18 his3-D1	Figs 1,3,4,S1,S3,S4,S5
DB_147	h+/h-	wt	ade-M210/ade-M216 leu1-32 ura4-D18	Not shown
NM 436	h90	leu:GFP-Psy1	leu1-32 ura4-D18	Not shown
NM 422	h+/h-	cdc10-M17	ade-M210/ade-M216	Figs 1,S1
DB_124	h90	bgs4::ura GFP-bgs4:leu	leu1-32 ura4-D18	Figs 2,3,5,6,7,S2,S3,S6
DB_166	h90	rga4::KanMX bgs4::ura GFP-bgs4:leu	leu1-32 ura4-D18	Figs 1,S1
DB_163	h90	rga2::KanMX bgs4::ura GFP-bgs4:leu	leu1-32 ura4-D18	Figs S1
DB_169	h90	bud6-3GFP:KanMX	leu1-32 ura4-D18	Figs 2,5,S2
DB_228	h90	GFP-A8-cdc42:KanMX	leu1-32 ura4-D18	Figs 2,5,S2
DB_214	h90	CRIB-GFP:ura	leu1-32 ura4-D18	Figs 2,5,S2
DB_226	h90	CRIB-GFP:ura bud6-Tomato:NatMX	leu1-32 ura4-D18	Figs 7,S2,S3
DB_287	h90	CRIB-GFP:ura bgs4::ura RFP-bgs4:leu	leu1-32 ura4-D18	Figs S2
DB_221	h90	bgs4::ura RFP-bgs4:leu bud6-3GFP:kan	leu1-32 ura4-D18	Figs S2
NM 376	h90	crn1-GFP::KanMX	ade6-M216	Figs S3
DB_201	h90	leu1-32:SV40:GFP-atb2[leu1+]		Figs S3
DB_182	h90	tea1:NatMX bgs4::ura GFP-bgs4:leu	leu1-32 ura4-D18	Figs 2, S3
DB_236	h90	tip1::kanMX bgs4::ura GFP-bgs4:leu	leu1-32 ura4-D18	Figs 2, S3
DB_181	h90	for3::KanMX bgs4::ura GFP-bgs4:leu	leu1-32 ura4-D18	Figs 2, S3
DB_234	h90	tea4::kanMX bgs4::ura GFP-bgs4:leu	leu1-32 ura4-D18	Figs 2, S3
DB_197	h90	mok13::kanR	leu1-32 ura4D-18 his3-D1	Figs 4
DB_186	h90	chs1::his3+	leu1-32 ura4D-18 his3-D1	Figs 4
DB_218	h90	orb6-25 bgs4::ura GFP-bgs4:leu	ade6-M216 leu1-32 ura4-D18	Figs 5, S5
DB_216	h90	gpd1::ura	ura4-D18	Figs 3
DB_323	h90	orb6-25 bud6-3GFP: KanMX	ade6-M216 leu1-32	Figs 5

Supplementary Table S1 (Related to Experimental procedures): Fission yeast strains used in this study

SUPPLEMENTAL FIGURES

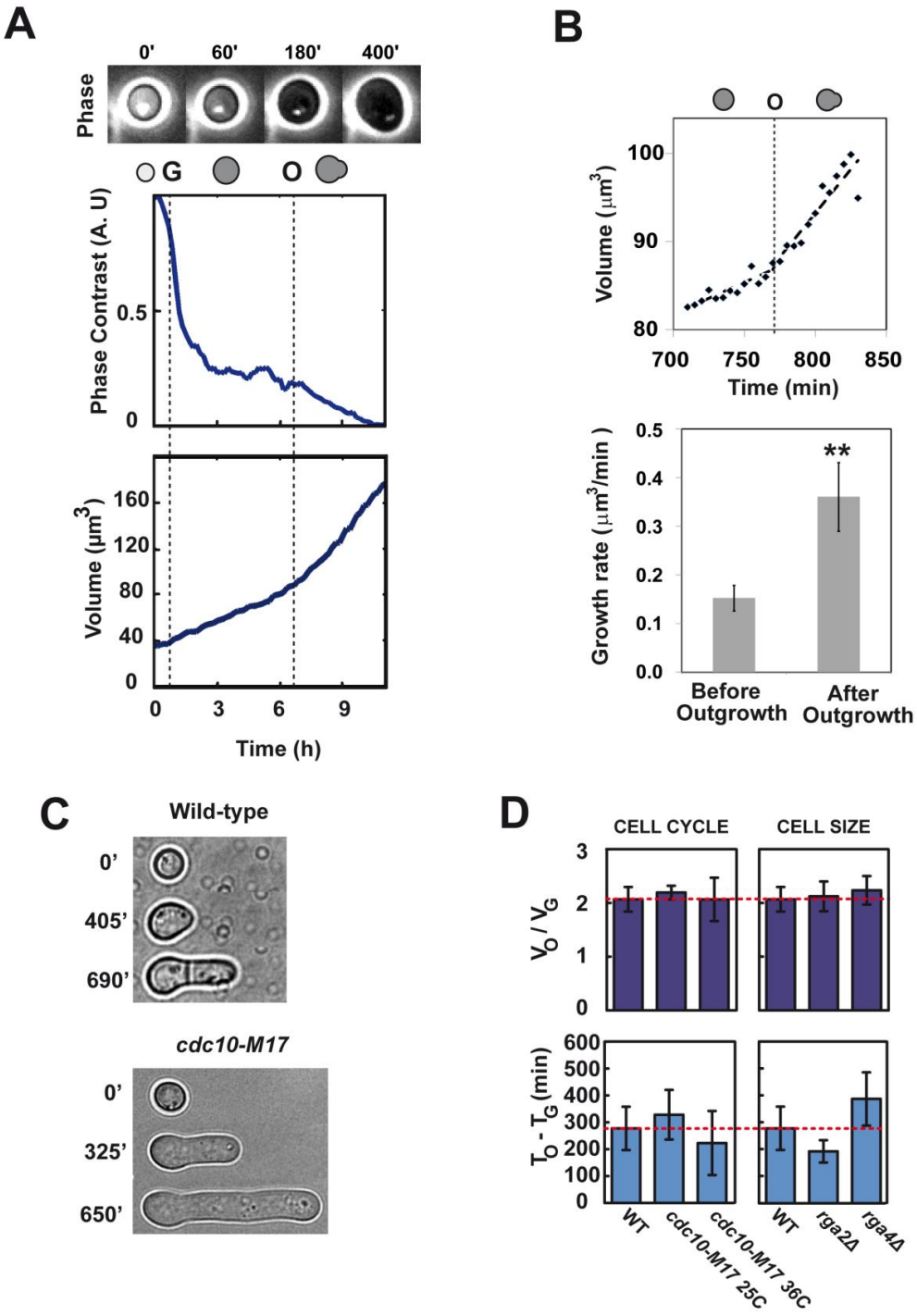

Figure S1

Supplemental Figure 1(Related to Figure 1): Characterization of morphogenetic changes at germination and outgrowth.

(A) Evolution of phase contrast intensity as a function of spore development, and corresponding volume evolution (bottom). High phase contrast signal corresponds to bright spores. **(B)** Growth rate increases at the onset of outgrowth. Top: Cell volume as a function of time. The dotted line corresponds to the linear fits of growth rates before and after outgrowth (indicated by the black dotted line). Bottom: Mean growth rates computed 1h before and 1h after outgrowth (n=13 spores). **(C)** Time-lapse bright field images of WT and *cdc10-M17* mutant spores grown at 37°C. Both strains do outgrowth at similar size increase, but *cdc10-M17* fails cell cycle progression and keeps elongating without dividing. **(D)** Volume-doubling for outgrowth is conserved in mutants defective in cell cycle progression and cell size. Mean volume ratios (dark blue bars) and mean germination to outgrowth times (light blue bars), of indicated mutants ($n > 30$ for each condition). Error bars correspond to standard deviations. ** $p<0.01$, Student's t-test.

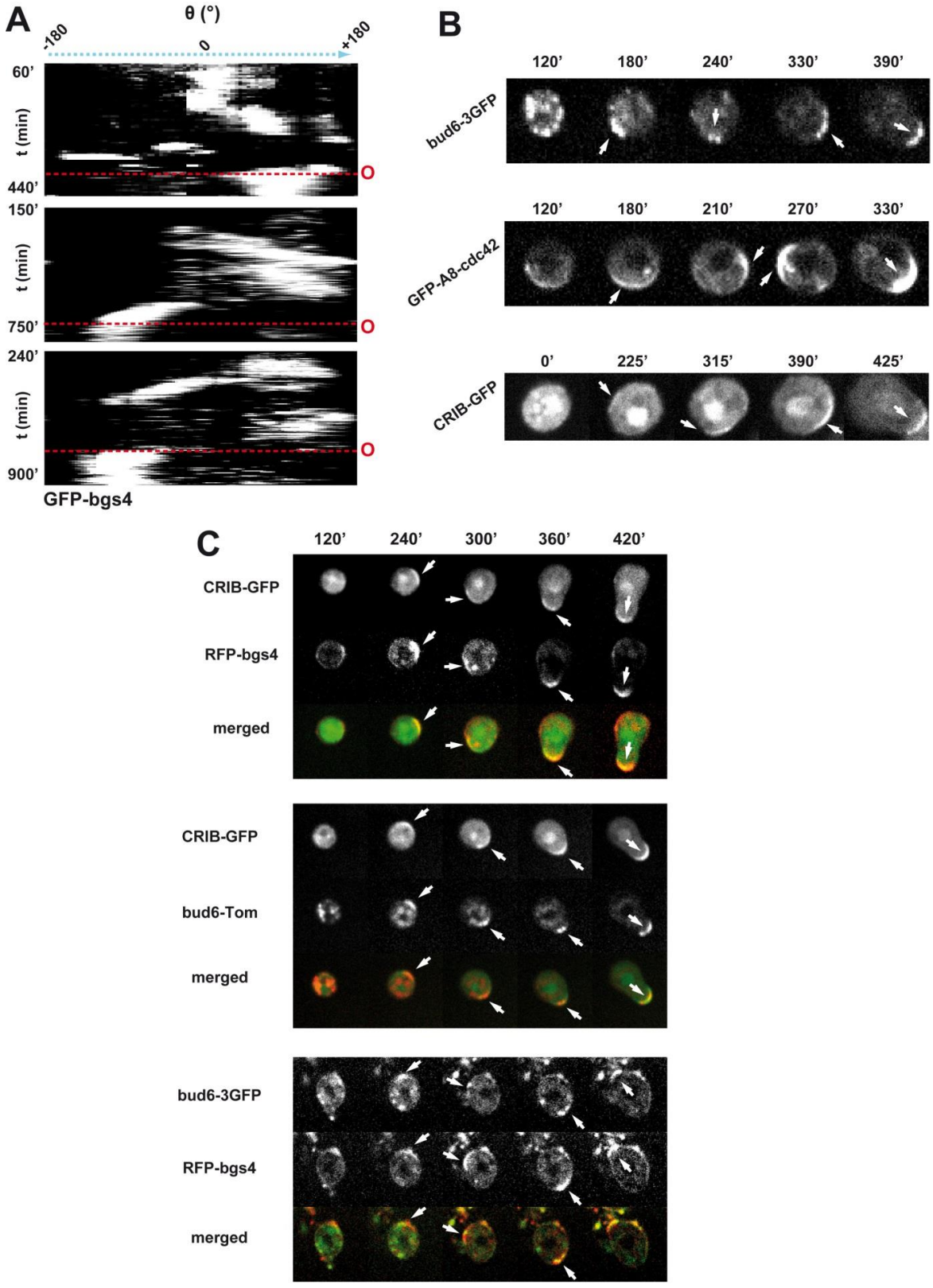
A
θ (°)
-180
0
+180
60'
t (min)
440'
O
150'
t (min)
750'
O
240'
t (min)
900'
O
GFP-bgs4
B
120'
180'
240'
330'
390'
bud6-3GFP
120'
180'
210'
270'
330'
GFP-A8-cdc42
0'
225'
315'
390'
425'
CRIB-GFP
C
120'
240'
300'
360'
420'
CRIB-GFP
RFP-bgs4
merged
CRIB-GFP
bud6-Tom
merged
bud6-3GFP
RFP-bgs4
merged

Figure S2

Supplemental Figure 2 (Related to Figure 2): Polarity components wandering

(A) Cell kymographs of three independent spores representing the changes of localization over time of the polarity factor GFP-bgs4 extracted from epifluorescence time-lapse. Red dotted lines mark the onset of outgrowth. **(B)** Time-lapse single confocal mid-slices of different polarity markers wandering around the spore surface before outgrowth. White arrows point at successive polar cap positions. Note that the nuclear localization of CRIB-GFP is a by-product of the probe, similarly observed in vegetative cells. **(C)** Time-lapse single confocal mid-slices of spores co-expressing the indicated polarity components. Note how polarity components co-wander two by two.

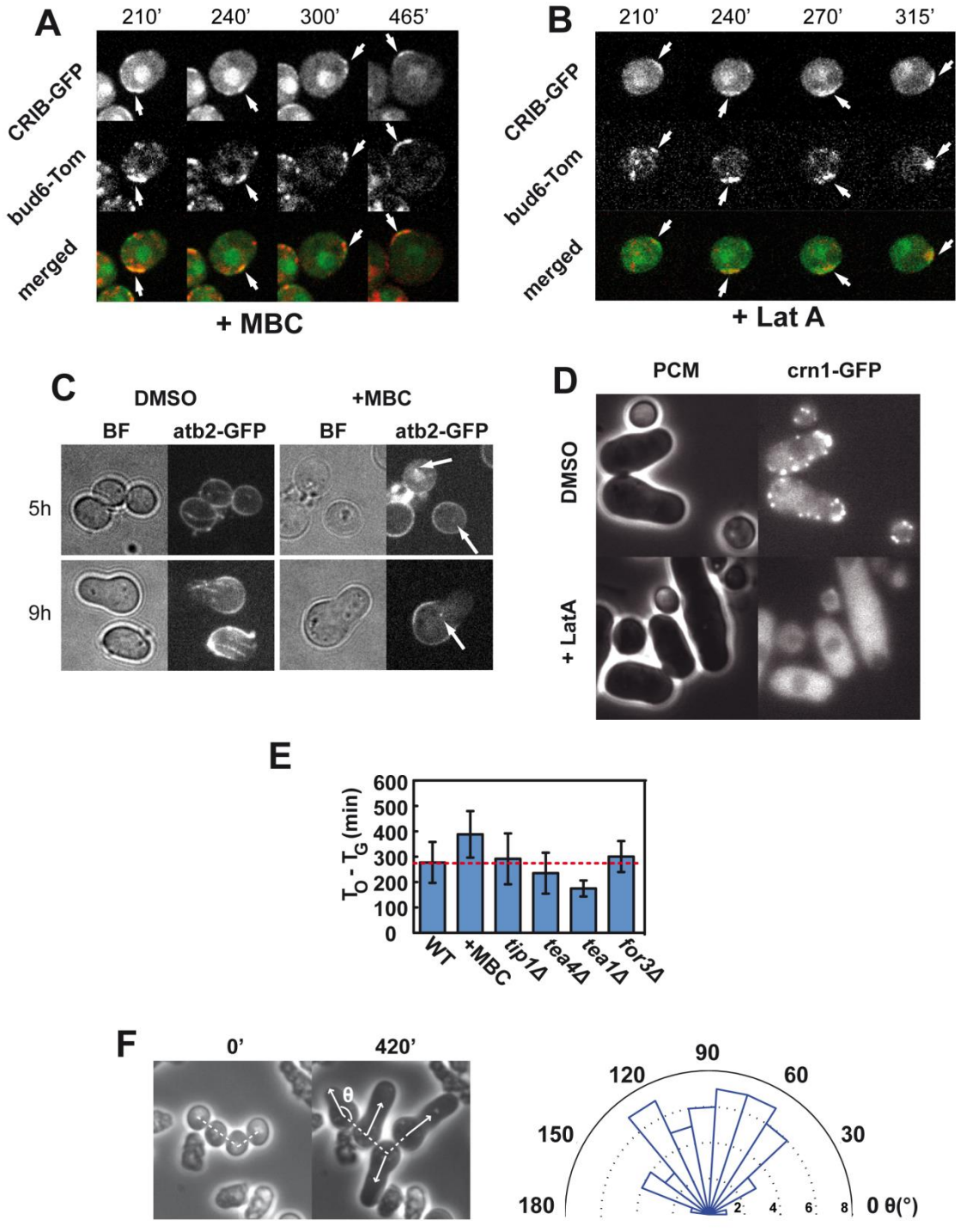
A
210'
240'
300'
465'
CRIB-GFP
bud6-Tom
merged
+ MBC
B
210'
240'
270'
315'
CRIB-GFP
bud6-Tom
merged
+ Lat A
C
DMSO
+MBC
BF
atb2-GFP
BF
atb2-GFP
5h
9h
D
PCM
crn1-GFP
DMSO
+ LatA
E
$T_O - T_G$ (min)
600
500
400
300
200
100
0
WT
+MBC
tip1Δ
tea4Δ
tea1Δ
for3Δ
F
0'
420'
θ
90
120
60
150
30
180
0
2
4
6
8
θ(°)

Figure S3

Supplemental Figure 3 (Related to Figure 2): Polar cap establishment, wandering and stabilization at outgrowth are independent on MTs, MT -associated factors, actin and memory cues

(A) Polar cap wandering is independent of microtubules: Time-lapse single confocal mid-slices of MBC-treated spores expressing CRIB-GFP and bud6-Tomato. White arrows point at the polar cap positions. **(B)** Polar cap wandering is independent of actin. Time-lapse single confocal mid-slices of LatA-treated spores expressing CRIB-GFP and bud6-Tomato. **(C)** Controls for the effect of the Microtubule depolymerizing drug MBC in spores. Bright-field and merged 12 z-stacks of spores expressing GFP-atb2, grown from germination in DMSO (control) or MBC. **(D)** Controls for the effect of Latrunculin A in spores. Phase contrast and epifluorescence images of control and LatA treated spores expressing crn1-GFP, a marker of actin patches. Addition of LatA, causes equal disappearance of actin structures in vegetative cells and in spores. **(E)** Mean germination to outgrowth times of indicated mutants (n>30 for each condition). Note the large variation in absolute time between different mutants. **(F)** Outgrowth direction is independent of previous meiotic division position. Left: Group of daughter spores derived from a mother ascus before germination and after outgrowth. The angle θ, represents the angle between the final growth direction (indicated by the white arrows) and the division axis between two close spores (indicated by the white dotted line). Right: Rose plots integrating angles from 80 different spores. Error bars correspond to standard deviations.

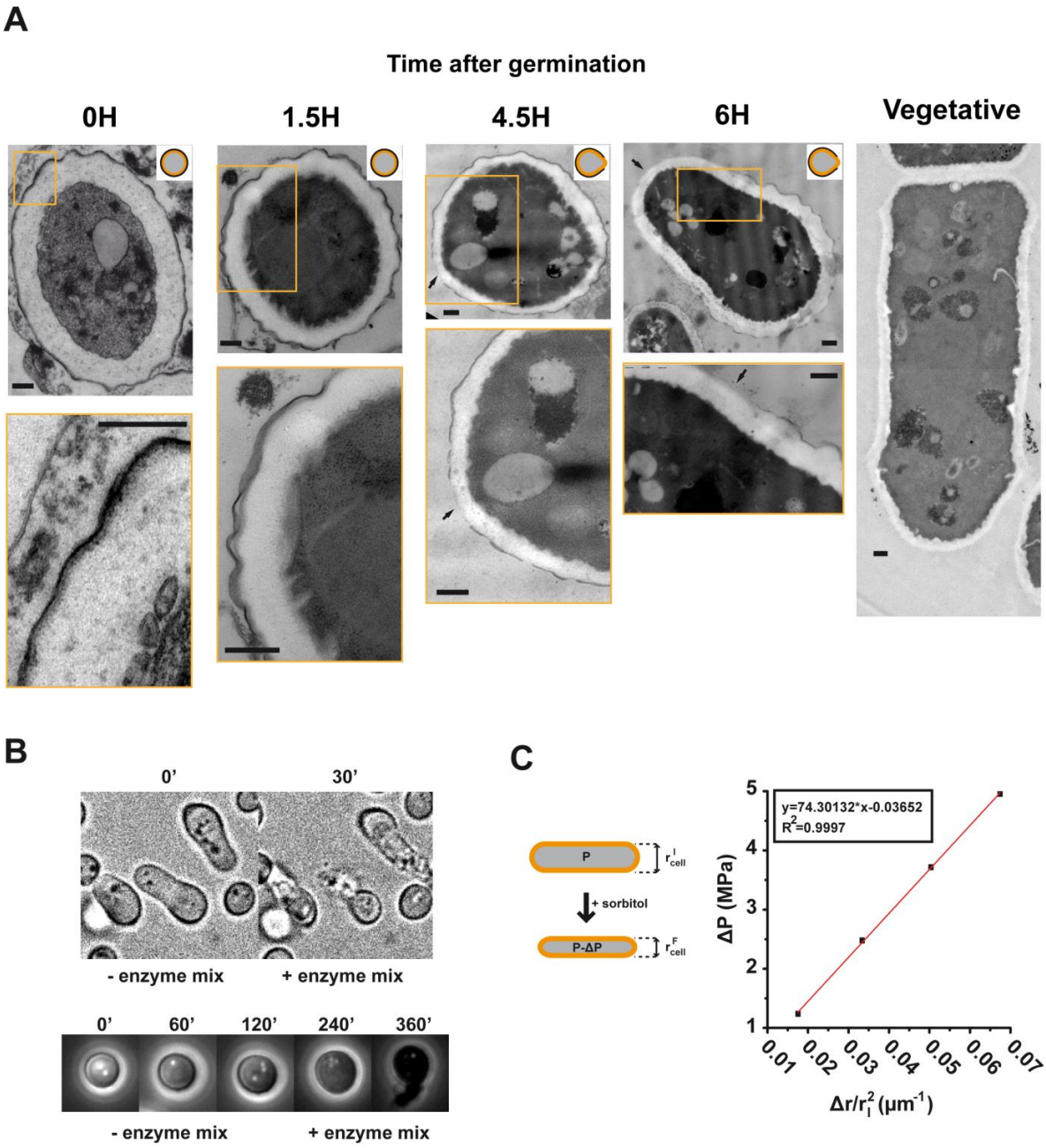
A
Time after germination
0H
1.5H
4.5H
6H
Vegetative
B
0'
30'
- enzyme mix
+ enzyme mix
0'
60'
120'
240'
360'
- enzyme mix
+ enzyme mix
C
P
+ sorbitol
P-ΔP
y=74.30132*x-0.03652
R2=0.9997
ΔP (MPa)
Δr/rI2 (μm-1)

Figure S4

Supplemental Figure 4 (Related to Figure 3): Evolution of spore cell walls during spore development and mechanics of cell walls.

(A) Transmission Electron Microscopy images of spores at different times after germination, with corresponding phenotype drawings and close-ups. Black arrows point at sites on the spores surface with no apparent OSW. Scale bars, 200 nm. **(B)** (Top) Description of the death assay used to monitor the presence of an intact spore outer spore wall. The time-lapse depicts the effect of the addition of an inner cell wall enzyme mix on spore (protected by the OSW) and outgrown spores where the tip is not protected anymore. Spores survive but outgrown spores burst and die within less than 30 minutes. (Bottom) Phase contrast time lapse of a single wild-type spore grown in microfluidic chambers from germination. The inner wall enzyme mix is added 3h after germination. At time 6h, note how the spore burst and dies because of the enzyme mix digesting the inner wall not protected anymore by the opened OSW. **(C)** (Left) Stress-strain experimental approach used to measure the elastic properties of vegetative walls: vegetative cells are exposed to different concentrations of sorbitol and the corresponding deformation at the tip side is measured, by tracking changes in local radius of curvature; (Right) Cell deformation scales linearly with osmotic pressure drops caused by dose-dependent sorbitol addition. Pressure drop is plotted as a function of local deformation of the tip for the case of WT vegetative cells. The surface modulus of the cell wall can be extracted from the linear fit (indicated by the red line), as described in experimental procedures.

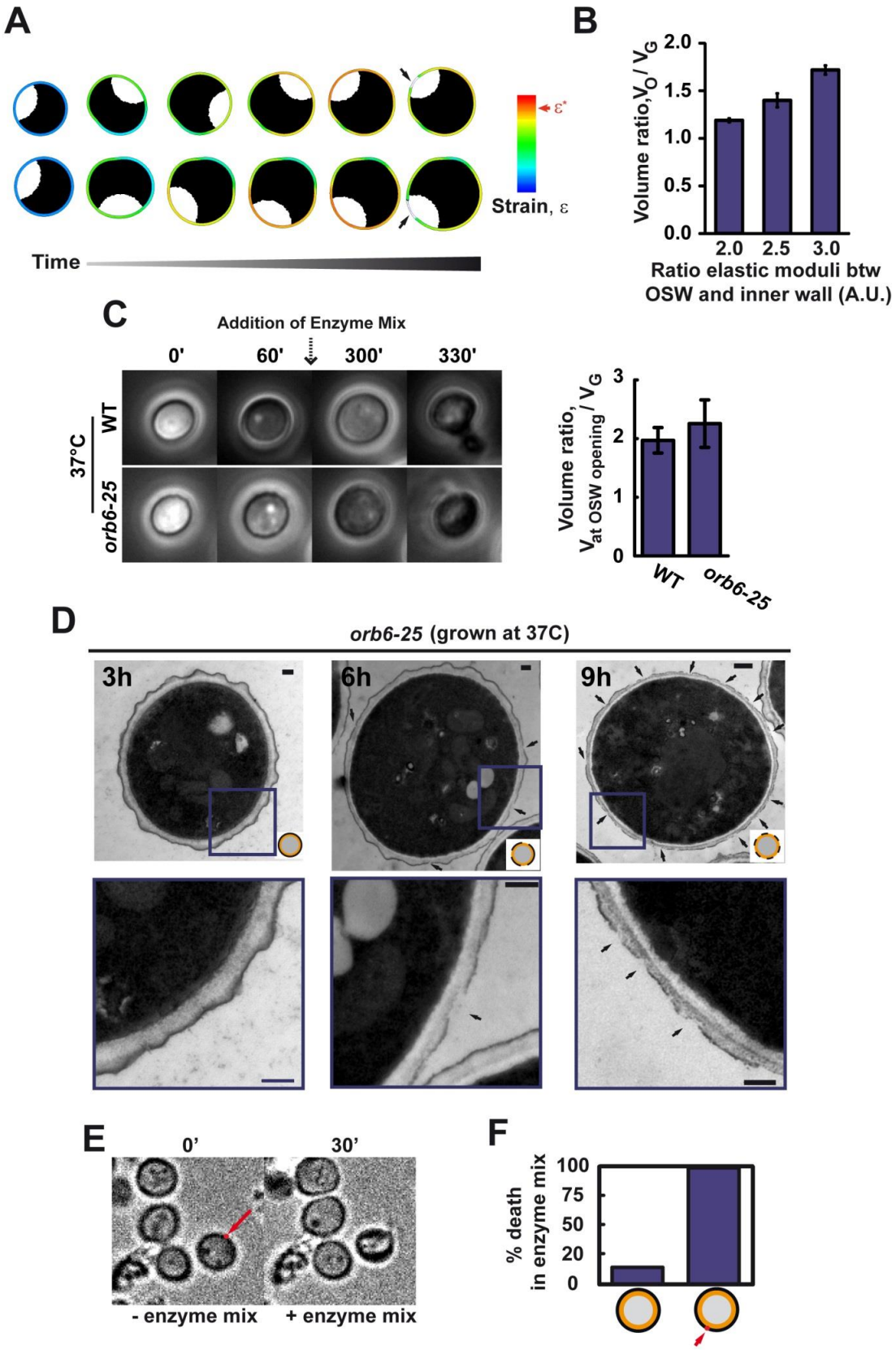
A
Time
Strain, ε
ε*
B
Volume ratio, V_O / V_G
2.0
1.5
1.0
0.5
0.0
2.0
2.5
3.0
Ratio elastic moduli btw
OSW and inner wall (A.U.)
C
Addition of Enzyme Mix
0'
60'
300'
330'
37°C
WT
orb6-25
Volume ratio,
$V_{at\ OSW\ opening}$ / V_G
3
2
1
0
WT
orb6-25
D
orb6-25 (grown at 37C)
3h
6h
9h
E
0'
30'
- enzyme mix
+ enzyme mix
F
% death
in enzyme mix
100
75
50
20
0

Figure S5

Supplemental Figure 5 (Related to Figures 4, 5 and 6): Spatio-temporal control of rupture in the OSW; and optimization of the specificity of UV laser assay in fragilizing the outer spore wall but not the inner wall.

(A) Spores growing *in silico*. Colors in the OSW correspond to local strain/stress values in the OSW. Note the local rupture in the OSW marked by the arrow when the strain reaches the red zone. **(B)** Influence of the ratio between elastic moduli of inner and outer spore wall on volume ratio for outgrowth, as predicted from numerical simulations. **(C)** Growth in enzyme mix assay for wild-type and *orb6-25* spores (grown at 37°C). (Left) Phase contrast time-lapses of spores growing and bursting at the moment of OSW opening. (Right) Volume ratio between spore volumes right before death, corresponding to OSW opening, and volume at germination. **(D)** Representative examples of TEM images of *orb6-25* spores grown at 37°C at different times after germination with corresponding phenotype drawings. Black arrows point at sites on the spores surface with openings in the OSW. Scale bars, 200 nm. Error bars correspond to standard deviations. (**E)** Use of enzyme mix death assay to optimize the selective effect of laser photoablation on the spore outer wall but not inner wall. The spore indicated by the arrow is photoablated, and the three other spores serve as controls. After rinsing with the enzyme mix, only the photoablated spore dies. **(F)** Death assay quantification in photo-ablated spores: percentage of dying spores in the enzyme mix in the case of photoablated and non-photoablated spores (n=37 spores).

Chapter 4

Strain- or stress-sensing in phyllotaxis

4.1 Summary

In the previous chapter, we saw how polar elongation is triggered by two couplings involving growth, one with mechanics and the other with polarity. Plants provide another example of coupling between mechanics and polarity, but at the tissue level. The outgrowth of the plant organs is triggered by the accumulation of the growth hormone auxin, which soften the cell wall. Thus the regular arrangement of these organs relies on the patterns of auxin. These patterns have been shown to be generated by the polar transport of auxin by the protein PIN FORMED1 (PIN1), which orients the efflux preferentially towards the cells with the higher concentration. Recently, several pieces of evidence have suggested that mechanics of the cell wall is the intermediary mechanism by which the transporters are ultimately able to measure auxin concentration: a cell with a higher auxin will be softer and thus the tension in its neighbors will increase to compensate this local weakness. This tension in turn activates the insertion of transporters, amplifying the auxin heterogeneity.

I implemented a chemomechanical model, incorporating the effects discussed above, chemomechanical model in order to investigate an issue rarely addressed in the context of mechano-sensing: is the feedback controlled by stress or by strain? To answer this question I simulated the experiments discussed in the literature that involve auxin transport and mechanical perturbation. Although the study of some of these experiments leads to ambiguous results, the overall conclusion is that a feedback based on strain agrees better with the available results.

I also studied the robustness of the two patterning mechanism with respect

to noisy inputs or transient parameter perturbations. Both kind of simulations support the idea of strain-sensing, whose wavelength is less sensitive, an observation that seems to fit better with the remarkable regularity of phyllotaxis.

For this project I implemented the model and performed the simulations and their analysis. I also wrote the paper, with some input from Alain and Arezki.

4.2 Paper

Stress- or strain-sensing in phyllotaxis

Jean-Daniel Julien[1,2,3], Alain Pumir[3] and Arezki Boudaoud[1,2]

[1]Laboratoire Joliot-Curie, [2]Laboratoire de Reproduction et Développement des Plantes, [3]Laboratoire de Physique, Ecole Normale Supérieure de Lyon, Lyon Cedex 07, France

Abstract

Both chemical and mechanical effects are known to play a major role in morphogenesis. In plants, the development of organs, such as leaves or flowers, notoriously involves chemical signaling; the phytohormone auxin and its directional transport play a key role in the emergence of robust patterns. Recent experiments indicate that cell mechanics feedback on auxin concentration by enhancing its transport in stretched cells, and conversely, auxin accumulation in incipient organs induces modifications in cell mechanics. The nature of the coupling between the two types of signals, however, remains largely unexplored. In particular, it is unclear whether active transport is sensitive to the strain or to the stress exerted on the tissue. Here, we address the nature of this coupling by using a theoretical approach. We implement a model of auxin patterning, with active transport mechanically regulated either by stress or by strain, and compare the resulting pattern formation with previous experimental results, where tissue mechanics is perturbed by ablations, chemical treatments, or genetic manipulations. We also study the

robustness of the patterning mechanism to noise and provide predictions for the effects of a shock that disrupts its chemical equilibrium. All together, our results favor a mechanism of strain-sensing. The computational modeling approach used here, which enables us to distinguish between several possible mechanical feedbacks, thus offers promising perspective to elucidate the role of mechanics in the development of other tissues, and may provide important insight on the underlying molecular mechanisms.

4.3 Introduction

Understanding the establishment of biochemical patterns in living organisms, such as zebrafish stripes [22] or hydra head positioning [3] remains a challenging question, despite many experimental and theoretical studies. The regular and highly reproducible positioning of the organs in plant shoots, called phyllotaxis, has intrigued scientists for a very long time [1]. It relies on the patterns of the growth hormone auxin, whose local accumulation is necessary for the emergence of new organs [23, 17]. Auxin efflux is facilitated by the membrane-localized PIN FORMED1 (PIN1) protein [33, 48], which can be polarly (asymmetrically) distributed, inducing a directional transport of auxin, and resulting in well-defined auxin patterns. This transport is necessary for the development of the plant: knocking it down, either genetically or chemically, leads to the absence of primordia at the shoot tip, which can be rescued by the local application of exogenous auxin [32, 38, 39].

Several models have been proposed to describe the interaction between the hormone and its carrier in the context of the shoot apex, with the major assumption that the transporters allocation between the different sides of a cell is driven by auxin concentrations [47, 21, 42, 46]. How the auxin concentration regulates the transporters, however, remains unclear.

Since morphogenesis relies on changes in the structural elements of the organism, biochemical patterns must also influence the mechanics of these structural elements, in plants [15] as well as in animals [18, 8, 37]. Conversely, mechanics can feedback on biochemical processes [15, 18, 19, 43], including gene expression [10] or cell fate [2]. Plants are well suited to study the coupling between biochemical and biophysical processes as hydrostatic

cell pressure generates tremendous forces and results in a high tension in the polysaccharide-based walls surrounding cells [12, 15]. The recent progress in computational approaches [7] and in the measurement of cell mechanics [27] has fostered a renewed interest for the mechanics of plant morphogenesis.

Notably, at the shoot apex, organogenesis is associated with a decrease in the stiffness of the cell wall [34] and likely with a reduced mechanical anisotropy[44]. In the context of phyllotaxis, the coupling between mechanics and chemistry was explored theoretically [31] and mechanics has been proposed to regulate the transport of auxin in the shoot apical meristem [16]. A mechanical feedback, capable of generating a local accumulation of auxin, was postulated [16]. Based on preferential localization of PIN1 in the regions of the plasma membrane in contact with the wall with highest mechanical stress, this mechanical feedback is supported by several experiments [16, 30, 6]. However, whether PIN1 polarity is driven by the stress or by the strain of the cell wall remains unclear. In fact, the issue of stress- or strain-sensing has been insufficiently studied, especially in the context of plant development [29].

In this work we address this issue by investigating a model of mechanical feedback on auxin transport, whose predictions can be compared with known results of experiments. We also study the robustness of the pattern formation mechanism with respect to noise and abrupt changes in some of the biochemical parameters. Our main result is that a strain feedback leads to a more realistic behavior, and to a patterning mechanism which is much less sensitive to noisy inputs or sharp perturbations.

4.4 Results

A mechanochemical model of auxin patterning We built a mechanochemical model of auxin transport and tissue mechanics that incorporates the influence of auxin on the stiffness of the cell wall and the mechanical feedback from the cell wall on auxin transport, as illustrated in Fig. 4.1. We briefly describe its main ingredients here, more details can be found in the method section. We modeled a single cell layer, accounting for the epidermis of the shoot apex. The rest state of the tissue is assumed to be a hexagonal lattice. As a result of turgor pressure, the tissue is under global isotropic tension. Each edge of the lattice is made of two cell walls corresponding to either of the two neighboring cells. Each cell wall is modeled by a linear spring, whose stiffness decreases with the auxin concentration of the corresponding cell. Changes in auxin concentration are due to production, degradation, diffusion and transport. We considered two hypotheses for the mechanical feedback: PIN1 proteins are inserted preferentially facing the cell walls that (i) undergo the highest elastic strain (elastic deformation) or (ii) the highest stress (force).

We considered two main observables: the polarity $\mathcal{P}$, which is the ratio between the highest and the lowest transporters concentrations along the cell edges, and the membrane fraction $\mathcal{F}$, which is the ratio between the transporters localized in the membrane and the total amount of transporters in a cell (Fig. 4.1).

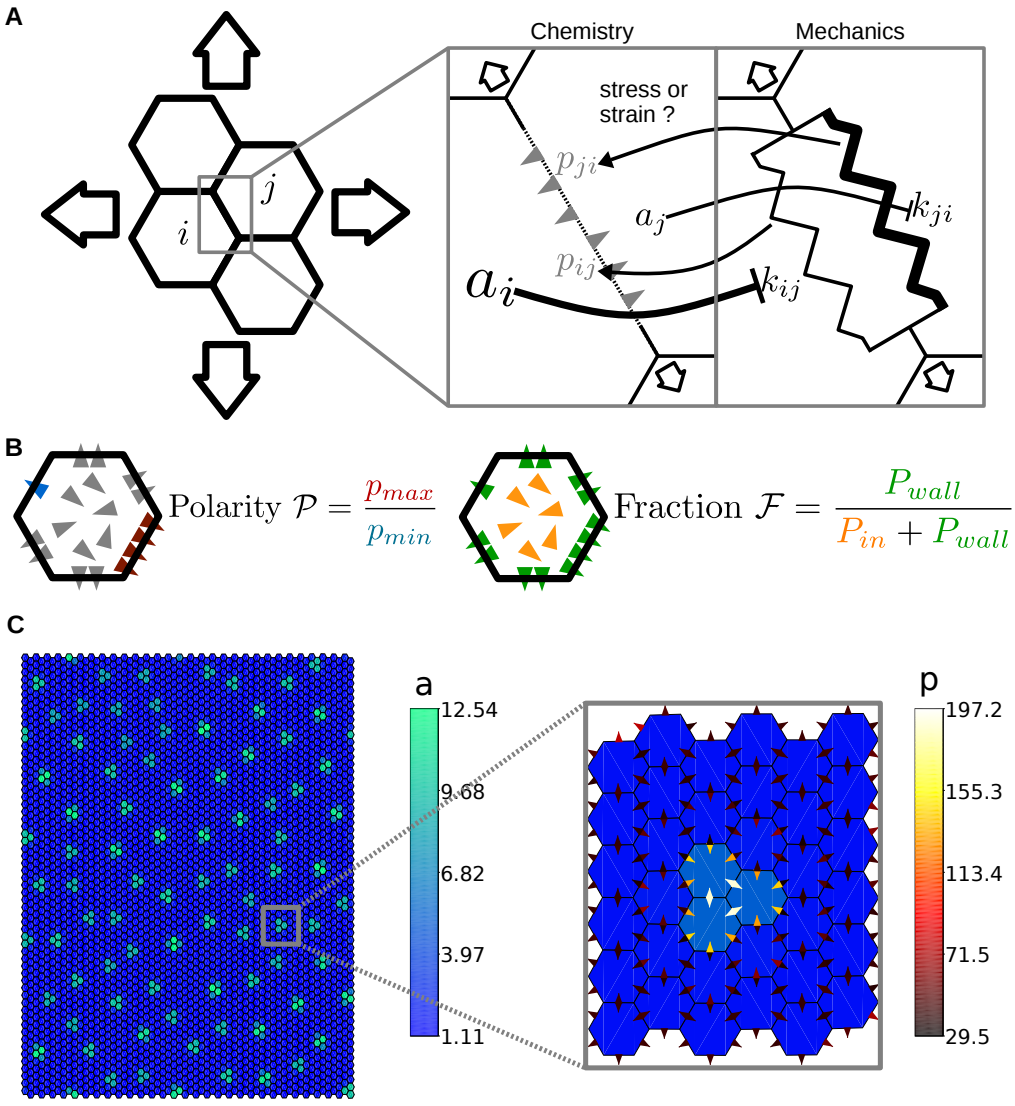

Figure 4.1: **Modeling assumptions and observables:** (A) Schematic of the model: the tissue consists of hexagonal cells, whose walls are subject to mechanical stress, and organize the transport of auxin. The biochemical and mechanical effects are presented in two different boxes, and their interactions are represented by arrows. The tissue is stretched by the turgor pressure. PIN1 proteins facilitate auxin movement out of cells. The stiffness of each cell wall is a decreasing function of the auxin concentration in the cell. The amount of effective transporters increases with the stress or strain at the cell wall. (B) Schematic definition of the two observables: the triangles represents the PIN1 transporters, colored according to the definition of the observables. The polarity $\mathcal{P}$ is the ratio between the two extremal concentrations in the cell walls of a cell. The fraction $\mathcal{F}$ is the ratio between the number of effective transporters and the total number of transporters. (C) An example of pattern predicted by the model: the cells are colored according to their auxin concentration. The box is a close-up on a part of the tissue, where PIN1 transporters are also depicted.

Cell ablation induces radial polarity When a single epidermal cell is laser-ablated at the shoot apex, the hypothesis that the epidermis is in tension implies that the maximal stress orientation is circumferential around the ablation [14]. The preferential localization of PIN1 transporters in the stretched walls would then makes the transport radial. A model similar to ours was able to reproduce this observation with a stress-driven feedback [16]. Here, we specifically asked whether our model can, with a strain-driven feedback mechanism, reproduce the experimental results. As in [16], auxin, transporters, and cell walls were removed from the ablated cell, while the insertion of transporters in the membranes of neighboring cells facing the ablated cell was excluded. Ablations lead to the radial reorientation of the transporters in neighboring cells (Figure 4.7), as in experiments [16]. It thus appears that ablation experiments do not allow us to distinguish between strain- and stress-feedback mechanisms.

Variations of polarity with turgor pressure Experiments with osmotic treatments show that PIN1 polarity is affected by changes in turgor pressure [30], as shown when quantifying the polarity $\mathcal{P}$. By performing osmotic treatments, turgor pressure was varied by approximately a factor 2 in these experiments. Polarity was significantly smaller (-15%) with reduced turgor and slightly smaller (-5%) with enhanced turgor.

We simulated the effect of a gradually increasing or decreasing turgor pressure by modulating tissue tension σ (see Eq.(4.1)), and monitored the change in the polarity of the transporters with the two possible mechanical feedbacks. We found numerically that the polarity increases with pressure in the range ($\sim 50\% - 200\%$) corresponding to experiments, with either feedbacks.

This increase is sharper at small turgor, consistently with experiments. At higher turgor pressure ($\sim$200%), the two models have a small disagreement with experiments as they predict a slight increase in polarity while a small decrease is observed. It is unclear whether this is due to a shortcoming of the model or to a bias in experimental quantifications.

With the stress feedback, the sharp drop seen in Fig. 4.2 is due to a change in the overall generated pattern of auxin peaks, which is not relevant in the present context, and is followed by an increase in polarity; examples of tissues and PIN1 distributions before and after this transition are shown in Figure 4.8.

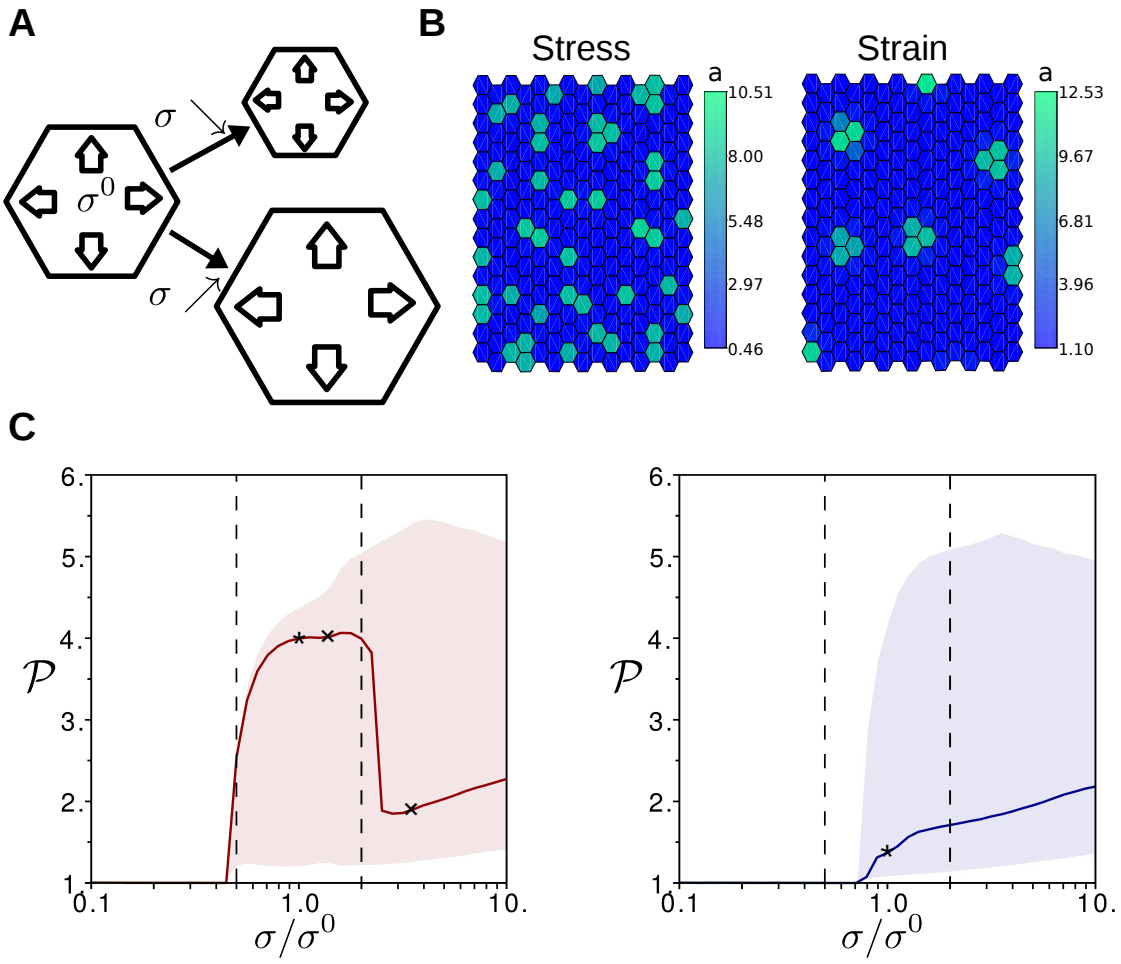

Figure 4.2: **Dependence of polarity on turgor pressure:** (A) Schematic of the simulations: starting from σ^0, the pressure is gradually increased or decreased, for pressures ranging from $0.1 \times \sigma^0$ and $10 \times \sigma^0$. (B) Examples of tissues with either feedback, in isotonic conditions ($\sigma = \sigma^0$), corresponding to the black stars in C. (C) For each cell the polarity $\mathcal{P}$ is measured. The curves represent the median value of $\mathcal{P}$ and the shaded areas the interval between the 85th and 15th percentiles on a tissue of 3600 cells. The results are shown in red (left) for the stress-based feedback, in blue (right) for the strain-based feedback. The dashed lines show the range of pressure investigated experimentally [30] and the black crosses indicate the parameters for which tissues are shown in Fig. 4.8.

Global softening of the tissue increases polarity Cellulose is the stiffest polysaccharide in plant cell walls. Accordingly, impairing cellulose synthesis

by chemical treatments leads to a softening of the plant tissues [40]. The consequence of such treatments on PIN1 localization was also investigated in [16]. First, PIN1 polarity, $\mathcal{P}$ is amplified - the membrane concentration of PIN1 increases where it is high before treatment and decreases elsewhere. Second, the amount of PIN1 decreases in the cytosol, or equivalently the membrane fraction $\mathcal{F}$ increases.

We simulated such treatments by decreasing the minimal stiffness, k_{min}, of the cell walls (Fig. 4.3). The increase in polarity $\mathcal{P}$ and in the membrane fraction $\mathcal{F}$ is reproduced with both feedbacks (Fig. 4.3). Therefore, these experiments do not allow us to discriminate between the two possible feedbacks.

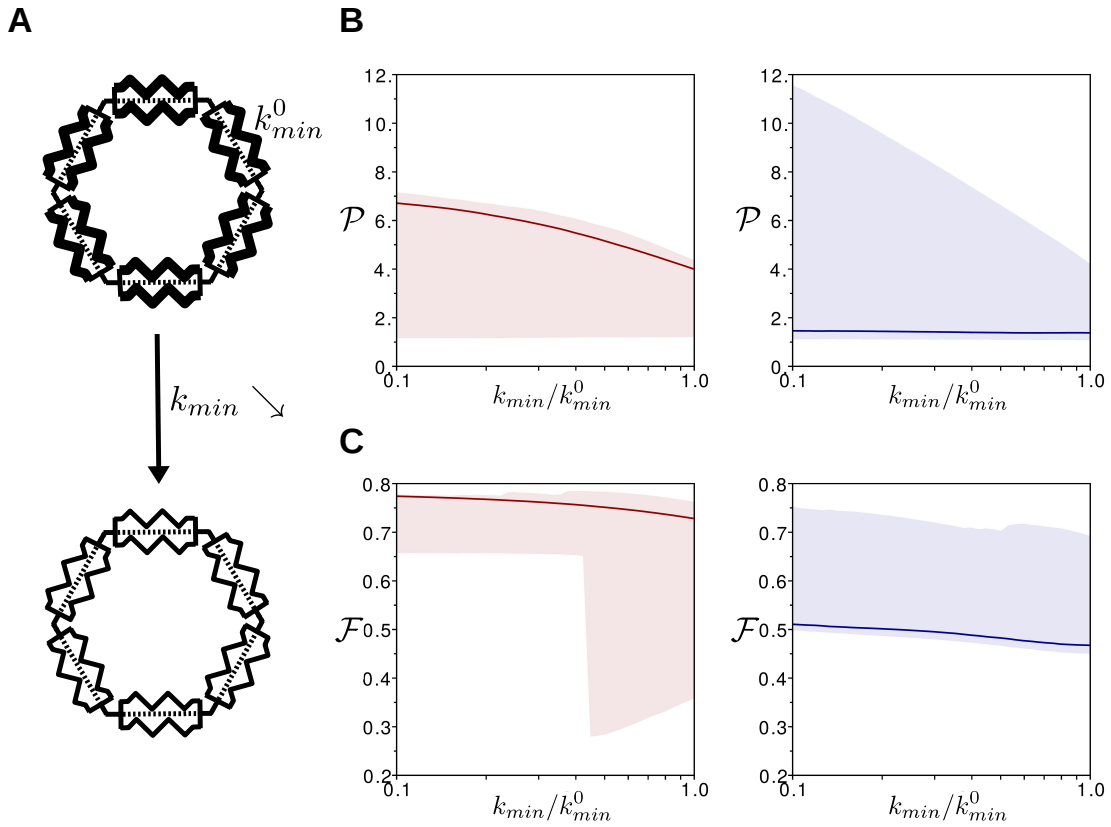

Figure 4.3: **Global softening of the tissue increases polarity:** (A) Schematic of the simulations: starting from k^0_{min}, the minimal stiffness of the tissue is gradually decreased, ranging from k^0_{min} to $k^0_{min}/10$. This corresponds to the stiffness at high levels of auxin. We quantified (B) the polarity $\mathcal{P}$ and (C) the membrane fraction $\mathcal{F}$ of transporters. The curves represent the median and the shaded areas the interval between the 85th and 15th percentiles on a tissue of 3600 cells. The results are shown in red (left) for the stress-based feedback, in blue (right) for the strain-based feedback.

Reducing auxin-driven softening disrupts polarity It has been shown that de-methyl-esterification of the pectin homogalacturonan by pectin methylesterases (PMEs) is necessary for auxin to soften the cells [35]. Indeed, in plants over-expressing PME INHIBITOR3, which inhibits PME activity, the application of auxin fails to trigger tissue softening and organ formation [6]. In these plant lines, polarity and membrane fraction are both reduced.

To simulate such overexpression, we decreased the value of the parameter, δk (see Eq.(4.3) in the method section), that controls the sensitivity of cell wall stiffness to auxin. A vanishing δk means that auxin has no effect on wall stiffness, and high values of δk imply that a small change in auxin level induces a large change in stiffness. In parallel, we kept $k_{min} + \delta k$ constant so that the reference stiffness (with no auxin) remains unchanged. We measured the polarity $\mathcal{P}$ and the fraction $\mathcal{F}$ of transporters in the cell walls with the two types of feedbacks.

Fig. 4.4 shows that when δk decreases, the polarity converges towards 1, meaning that the pattern is abolished. Thus both feedbacks reproduce the polarity loss due to tissue stiffening. However, the variations of the membrane fraction $\mathcal{F}$ depend on the precise feedback mechanism. When stiffening the tissue, $\mathcal{F}$ decreases with the strain feedback, but remains approximately constant with the stress-feedback, as shown in Fig. 4.4.

The behavior of the model can be understood analytically. In the homogeneous state, that is in the absence of auxin patterns as observed in the simulations when δk is decreased, the membrane fraction can be computed exactly. The calculations predict that $\mathcal{F}^{stress}$ remains constant, whereas $\mathcal{F}^{strain}$ decreases when δk decreases (see supplementary material for more details). In view of these results, we conclude that a strain feedback is more realistic to describe experiments where PME activity is manipulated.

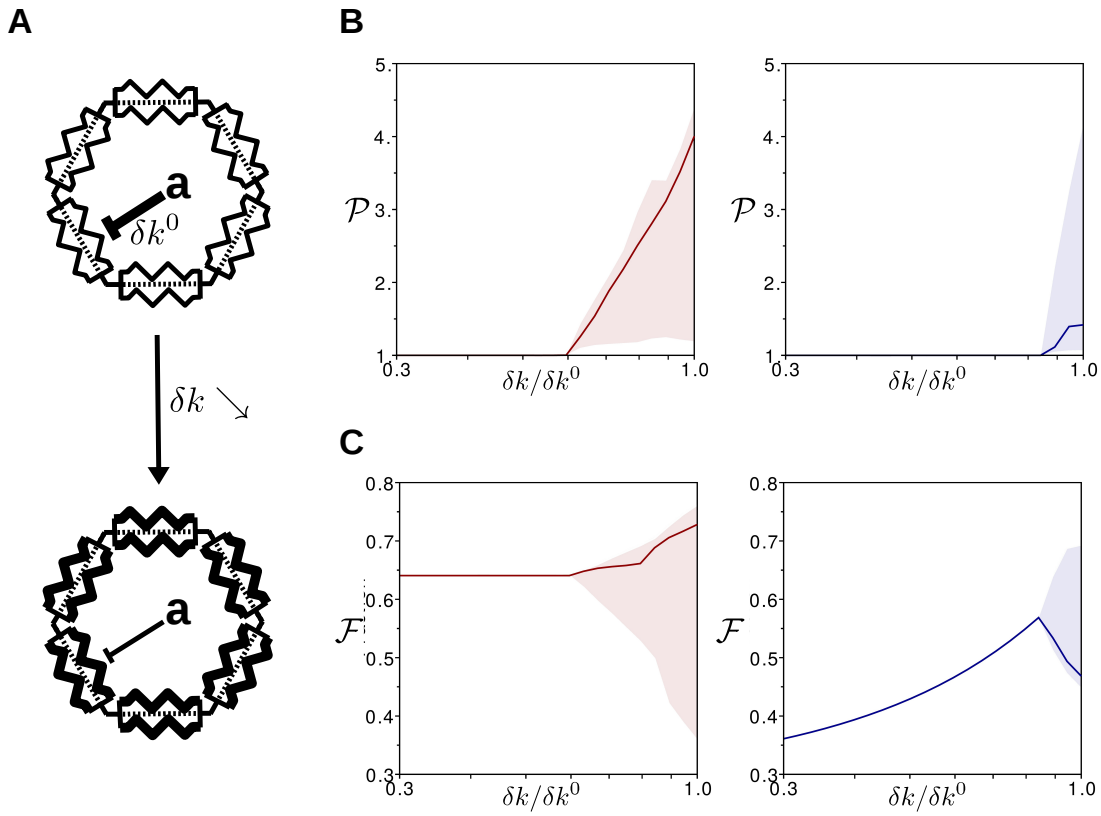

Figure 4.4: **Reducing auxin effects on the cell wall disrupts polarity:** (A) Schematic of the simulations: starting from δk^0, the amplitude of stiffness variations is gradually decreased, from k^0_{min} to $0.3 \times k^0_{min}$. We quantified (B) the polarity $\mathcal{P}$ and (C) the membrane fraction $\mathcal{F}$ of transporters. The curves represent the median and the shaded areas the interval between the 85th and 15th percentiles on a tissue of 3600 cells. The results are shown in red (left) for the stress-based feedback, in blue (right) for the strain-based feedback.

Robustness to noise We then investigated the robustness of the patterning mechanism by studying its sensitivity to noise. A random term, temporally and spatially uncorrelated, is added to the production rate of auxin or to the concentration of transporters (respectively p_a or P in Eq. (4.2)). We measured the wavelength of the pattern and its dependence on the noise amplitude (Fig. 4.5).

The pattern is almost insensitive to the effect of noise on the production of

auxin. In contrast, noise in the concentration of transporters P alters significantly the pattern. With the stress feedback, the wavelength is observed to increase by up to 200%, whereas the increase in the wavelength of the pattern is only 20% with the strain feedback. Thus the model predicts that the coupling based on stress is far more sensitive to noise in PIN1 quantities, than the coupling based on strain. Although it is difficult to assess the level of noise in planta, the striking robustness of phyllotaxis suggests that a strain feedback is more relevant.

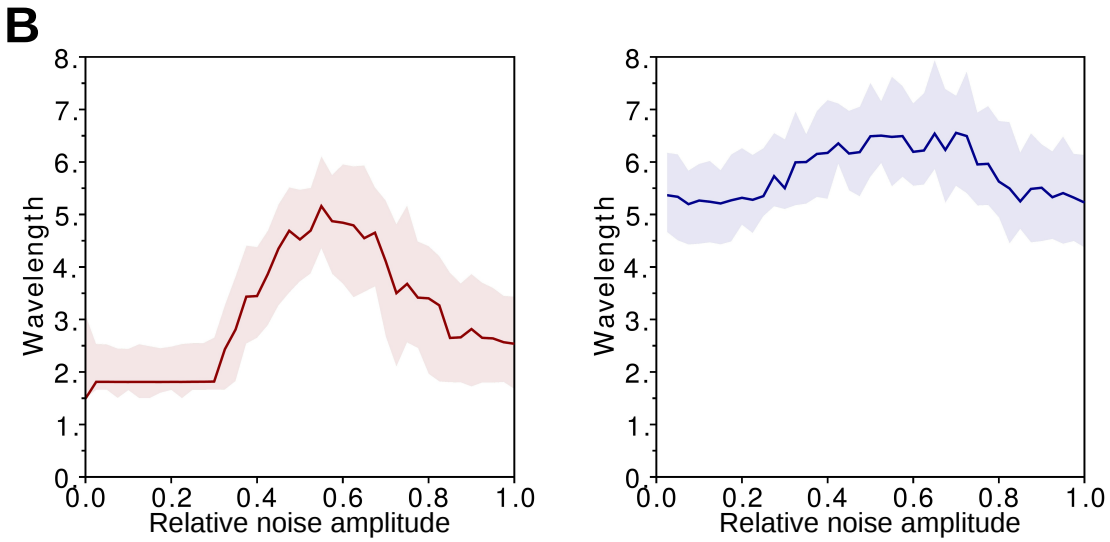

Figure 4.5: **Robustness to noise:** The auxin production rate p_a (A) or the PIN1 concentration P (B) is spatially and temporally random, with a uniform distribution centered around the value of these parameters without noise. The relative noise amplitude is half the ratio between the width of this interval and the average value of the variable. The wavelength is measured as the average distance between a peak and its nearest neighbor. The prediction of the model with the stress feedback is shown in red (left), while the one with the strain feedback is represented in blue (right). The curves represent the median and the shaded areas the interval between the 85th and 15th percentiles.

Robustness to sharp variations Even though robustness to noise discriminates between the two models, noise is difficult to manipulate experimentally. Robustness can also be tested by applying a transient shock to the system, i.e. a sharp modification of the external parameters, and by observing whether the tissue returns to its pre-shock state. Experimentally, this is feasible by transient chemical perturbation, such as external auxin application or inhibition of auxin transport.

We simulated such perturbation as follows. After an equilibrium is reached, we modify the mean auxin level $\langle a \rangle$ (through the production rate p_a) or the concentration of transporters P until the system reaches a second equilibrium. Then we reset the parameter to its initial value and obtain a third equilibrium. We compare the wavelengths of the first and third equilibria. Observing the same wavelength would mean that the system exactly recovers its initial state.

With either feedback, large differences in wavelength can be observed between the first and the third equilibria. The strain feedback is not as sensitive (Fig. 4.6), which is qualitatively consistent with its lower sensitivity to noise.

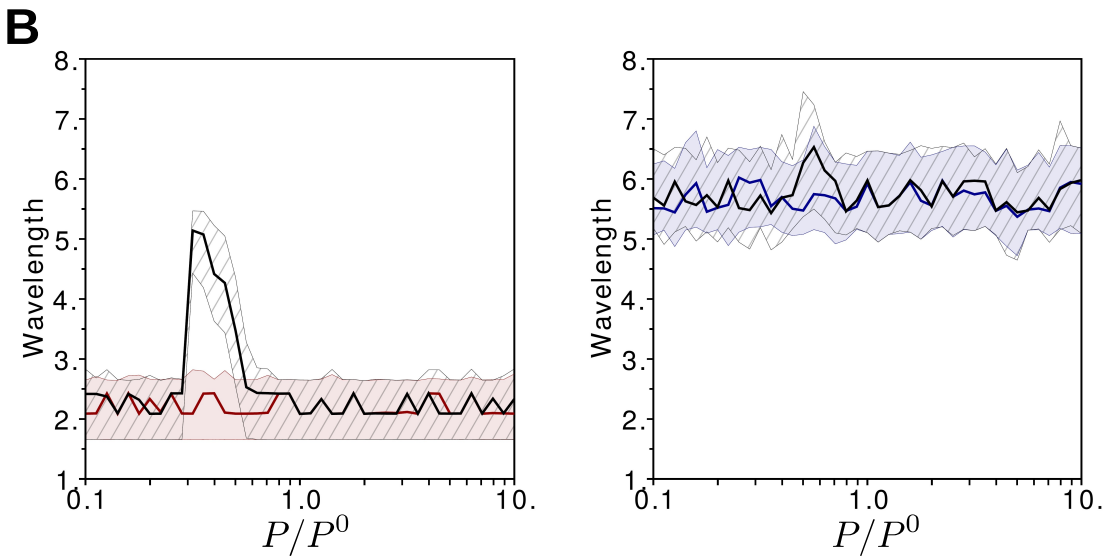

Figure 4.6: **Robustness to sharp variations:** The auxin production rate p_a (A) or the PIN1 concentration P (B) is transiently modified over the entire tissue. Once the tissue reaches equilibrium, the original set of parameters is restored. The wavelength is measured at equilibrium before the shock and, and at equilibrium after reseting the original parameters. The wavelength before the shock is plotted in red for the stress feedback (left) and in blue for the strain feedback (right). The wavelength after the recovery is plotted in black. The curves represent the median, the shaded areas the interval between the 85th and 15th percentiles before the shock, and the hatched areas the same percentiles after the reseting.

4.5 Discussion

We developed here a mechanochemical model for auxin patterning in the plant shoot apical meristem. Auxin promotes organ initiation via the local softening of the tissue [23, 17]. In addition, cell mechanics regulates the transport of the growth hormone auxin, via the PIN1 proteins. Patterns of auxin peaks result from the interplay between these two chemomechanical processes [16]. The central question, addressed with our model, is whether the insertion of the efflux facilitators in the membrane is driven by the strain of the cell walls or by the stress applied to them. To this end, we compared the predictions of the model with available experimental results.

We found that both stress and strain-based feedbacks lead to similar predictions when simulating cell ablation, turgor-induced changes in tissue tension, or a global reduction of the stiffness of the cell walls, generally in agreement with observations. Modeling *PMEI*-overexpressing plants allowed us to discriminate between the two models: Assuming that auxin effect on cell wall stiffness is reduced in such plant lines, we found that only the strain-based feedback accounted for observations. Interestingly, organogenesis is abolished in these lines, showing that it is useful to investigate the system behavior in the absence of patterns. Finally, investigating the effect of noise, or of a transient change in chemical parameters, on patterning reinforced our conclusion: Patterns appear more robust with the strain-based feedback.

The model, however, partly failed to reproduce the observations concerning the effect of tissue tension on polarity. Irrespective of the feedback chosen, we found that polarity increased with tension, whereas, experimentally, polarity slightly decreases from isotonic to hypertonic conditions [30]. A pos-

sible explanation is that we assumed the amount of transporters per cell to be constant, whereas PIN1 levels decrease in hypertonic conditions; other processes might be triggered when plants react to such osmotic stress. Alternatively, the slight decrease observed might be due to a small experimental bias, and the difference between experiments and our simulations might be not significant.

Overall, our work suggests that PIN1 proteins are allocated to membranes with the highest strain, raising the question of the underlying molecular mechanisms. Many types of mechanosensors are known [36]. In the case of PIN1, strain could shift the balance between endocytosis and exocytosis, accounting for the strain-based feedback, because osmotic stress affects cell trafficking, in particular through clathrin-mediated endocytosis [50]. The contact between the plasma membrane and the cell wall is needed for PIN1 polarity [4, 9], suggesting that the mechanical state of the cell wall is relevant for polarity. However the role of the cell wall might just be to reduce lateral diffusion of PIN1, helping to maintain the distribution of PIN1 determined by cell trafficking [26].

The question of strain- and stress-sensing was raised in the context of plant cortical microtubules orientation by mechanical cues, and the combination of experimental and theoretical approaches suggests that stress-sensing is more likely to be involved [14, 5]. The same conclusion has been reached concerning the actomyosin cortex in the drosophila wing disc [24]. However, the case of isolated animal cells has been debated. Early experiments suggested force- [11] or deformation-sensing [41]. More recent experiments showed that deformation-sensing occurred at low force, while force-sensing occurred at high force [49], though other experiments showed that cells could sense the

stiffness of extracellular space [28], consistently with the observation that cells can differentiate according to the stiffness of their environment [2]. Actually, mechanosensing occurs at different scales [36], so that the mechanical variable sensed may depend on the specific function.

In order to disentangle the parameters involved in mechanosensing, it is necessary to combine experimental perturbations of cells or tissues with analytical and computational studies of their behaviors. This is now made possible by the improvement of micromechanical [27] and computational [7] approaches. In this spirit, the present work provides insight on how the interaction between biomechanical and biochemical fields contributes to the robustness of morphogenesis.

4.6 Materials

Tissue mechanics We model auxin transport through anticlinal cell walls in the epidermis and thus we neglect the mechanical contribution of other cell walls. We assume that the rest state of the tissue to be a regular hexagonal tiling of the plane and we formulate the problem in terms of a vertex model with periodic boundary conditions. The equilibrium positions of the vertices are obtained by minimizing the mechanical energy of the N_C cells. The contribution of cell i to the mechanical energy is

$$E_i = \sum_{\langle j \rangle_i} l^0 \mathcal{E}_{i,j} \; ; \; \mathcal{E}_{i,j} = \frac{1}{2} k_{i,j} \varepsilon_{i,j}^2 \; ; \; \varepsilon_{i,j} = \left(\frac{l_{i,j} - l^0}{l^0} \right)$$

$\langle j \rangle_i$ stands for the 6 cells neighboring cell i. l^0 is the rest length of all walls. $\mathcal{E}_{i,j}$ is the linear energy density of the cell wall between cell i and cell j, $k_{i,j}$ its

stiffness, $l_{i,j}$ its length, and $\varepsilon_{i,j}$ its strain. The stress in the anticlinal wall is then given by the derivative of its energy with respect to strain:

$$S_{i,j} \equiv \frac{\partial \mathcal{E}_{i,j}}{\partial \varepsilon_{i,j}}.$$

Forces resulting from turgor pressure and tissue curvature are accounted for by external stress with components σ_x, σ_y. The total energy of the tissue then takes the form

$$E = -\sigma_x L_{y,0} \left(L_x - L_{x,0}\right) - \sigma_y L_{x,0} \left(L_y - L_{y,0}\right) + \sum_{i=1}^{N_C} E_i \tag{4.1}$$

where L_x and L_y are the tissue dimensions along the x and y directions and L_x^0 and L_y^0 their values without external stress. Here we considered only isotropic cases, such that $\sigma_x = \sigma_y = \sigma$.

Auxin dynamics and coupling with the mechanics We follow assumptions made in previous studies [21, 42]. We only model auxin concentrations in the cytosol; we assume auxin movement through cell walls to be the limiting step and therefore PIN1 dynamics to be fast compared to auxin dynamics. These assumptions lead to one chemical equation per cell, that describes auxin concentration, a_i, in cell i, and accounts for auxin synthesis at rate p_a, degradation rate d_a, diffusion (coefficient D), and PIN1 dependent efflux:

$$\begin{aligned} \frac{da_i}{dt} &= p_a - d_a a_i - \frac{P}{A} \sum_{\langle j \rangle_i} l_{i,j} \left(t\left(a_i\right) p_{i,j} - t\left(a_j\right) p_{j,i}\right) \\ &- \frac{D}{A} \sum_{\langle j \rangle_i} l_{i,j} \left(a_i - a_j\right) \end{aligned} \tag{4.2}$$

where A is the area of each hexagon, and P is the total concentration of PIN1 proteins, assumed to be cell-independent. (Other notation is the same as earlier.) The rate of auxin transport by PIN1 proteins, $t(a)$, has the following sigmoidal-dependence on auxin concentration:

$$t\left(a\right) = \frac{a^{H_t}}{K_t^{H_t} + a^{H_t}}$$

where K_t is a threshold in auxin concentration and H_t the Hill coefficient.

Auxin controls tissue mechanics by softening the cell walls (Fig.1). The stiffness of the walls decreases with the amount of auxin in the cells:

$$k\left(a\right) = k_{min} + \delta k \frac{K_k^{H_k}}{K_k^{H_k} + a^{H_k}} \tag{4.3}$$

where k_{min} is the wall stiffness in the absence of auxin, δk the variations in stiffness, K_k the auxin threshold and H_k the Hill coefficient.

Conversely, tissue mechanics feedbacks on auxin dynamics via its transport. The amount of PIN1 transporters in the cell is shared between its walls depending on their strain or on their stress (Fig. 4.1). The rate of PIN1 proteins facilitating auxin efflux from cell i to cell j is

$$p_{i,j} = \frac{K_f^{H_f} \left(\left(\alpha + (1-\alpha) \frac{k_{i,j}}{k_0} \right) \varepsilon_{i,j} \right)^{H_f}}{1 + \frac{\sum\limits_{\langle k \rangle_i} l_{i,k} K_f^{H_f} \left(\left(\alpha + (1-\alpha) \frac{k_{i,k}}{k_0} \right) \varepsilon_{i,k} \right)^{H_f}}{\sum\limits_{\langle k \rangle_i} l_{i,k}}}$$

where $\alpha = 0$ for the stress feedback, $\alpha = 1$ for the strain feedback. $\mathcal{E}_{i,j}$ and $k_{i,j}$ stand for wall strain and wall stiffness as described above. The parameter k_0 is set to k^*, the value of the stiffness in the homogeneous equilibrium state, so

that the contributions of stress and strain are of the same order of magnitude in the homogeneous state. K_f sets the slope of the insertion function and H_f is the corresponding Hill coefficient.

Observables Two observables are relevant for the comparison between our simulations and experimental observations (Fig. 4.1) [30, 6]. The first is polarity, defined as the ratio of the PIN1 concentrations on the most and least enriched membrane of cell i:

$$\mathcal{P}_i = \frac{p_i^{max}}{p_i^{min}} = \frac{\underset{\langle j \rangle_i}{\max}\left(p_{i,j}\right)}{\underset{\langle j \rangle_i}{\min}\left(p_{i,j}\right)},$$

and the second is the ratio of plasma membrane localized PIN1 to the total amount in the cell:

$$\mathcal{F}_i = \frac{P_i^{wall}}{P_i^{in} + P_i^{wall}} = \frac{\sum\limits_{\langle j \rangle_i} l_{i,j} p_{i,j}}{\sum\limits_{\langle j \rangle_i} l_{i,j}}$$

In practice we use their averages over all the tissue, $\mathcal{P}$ and $\mathcal{F}$, respectively.

Implementation The model was programmed in C. The energy is minimized thanks to the BFGS algorithm [25], implemented in the NLopt library [20]. The differential equations are solved thanks to the GNU GSL library with a Runge-Kutta (2, 3) method [13]. Data analysis is performed in Scilab [45]. Table 4.6 summarizes the values of the parameters used in the present work.

Table 4.1: Values of the parameters used in the simulation.

l^0	σ	p_a	d_a	D	P	K_t	H_t	K_f	H_f	k_0	k_{min}	δk	K_k	H_k
1	1.4	1	0.5	5	100	2	1	30	3	30	10	40	2	2

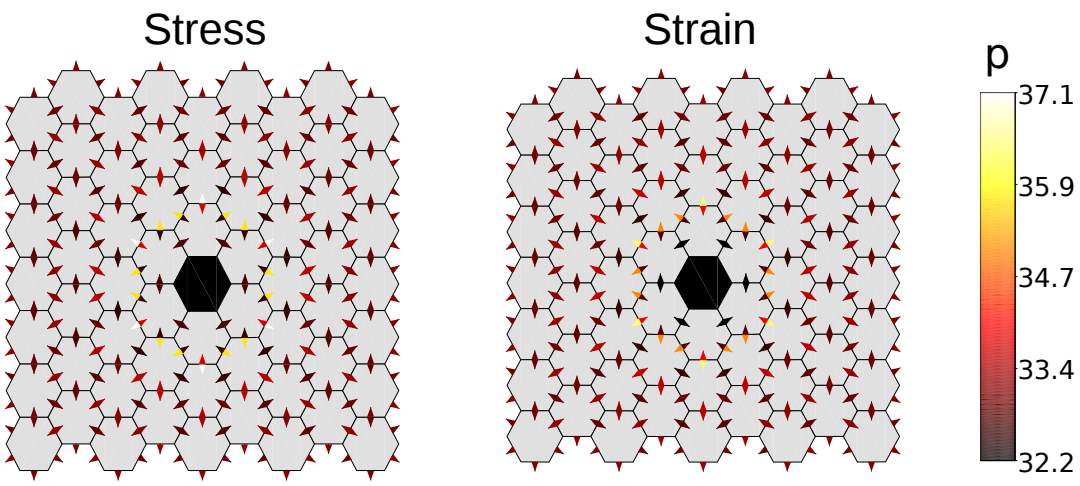

Figure 4.7: **Radial polarity around a cell ablation:** The black hexagon corresponds to the ablated cell, whose walls, auxin and transporters have been removed from the simulation. The transporters pointing toward this cell are also removed. The arrows represent the transporters, pointing away from the cell in which they facilitate efflux. Their colors indicate the concentration of transporters on this cell wall. The insertion of transporters is driven either by stress (left) or by strain (right). The degradation of auxin was increased for these simulations so that there is no auxin pattern that superimposes with the ablation pattern.

Change of pattern type with increased pressure for the stress-feedback

A sharp decrease of the median polarity $\mathcal{P}$ was predicted with a stress-based feedback when tension is increased above $\sigma/\sigma_0 = 2.3$ (see Fig. 4.2). This decrease is due to the change of pattern type. At low tension, the auxin peaks are limited to one or two cells. They become larger as tension increases. This enlargement corresponds to smaller auxin gradients between neighboring cells and accordingly to weaker polarities (see Fig. 4.8).

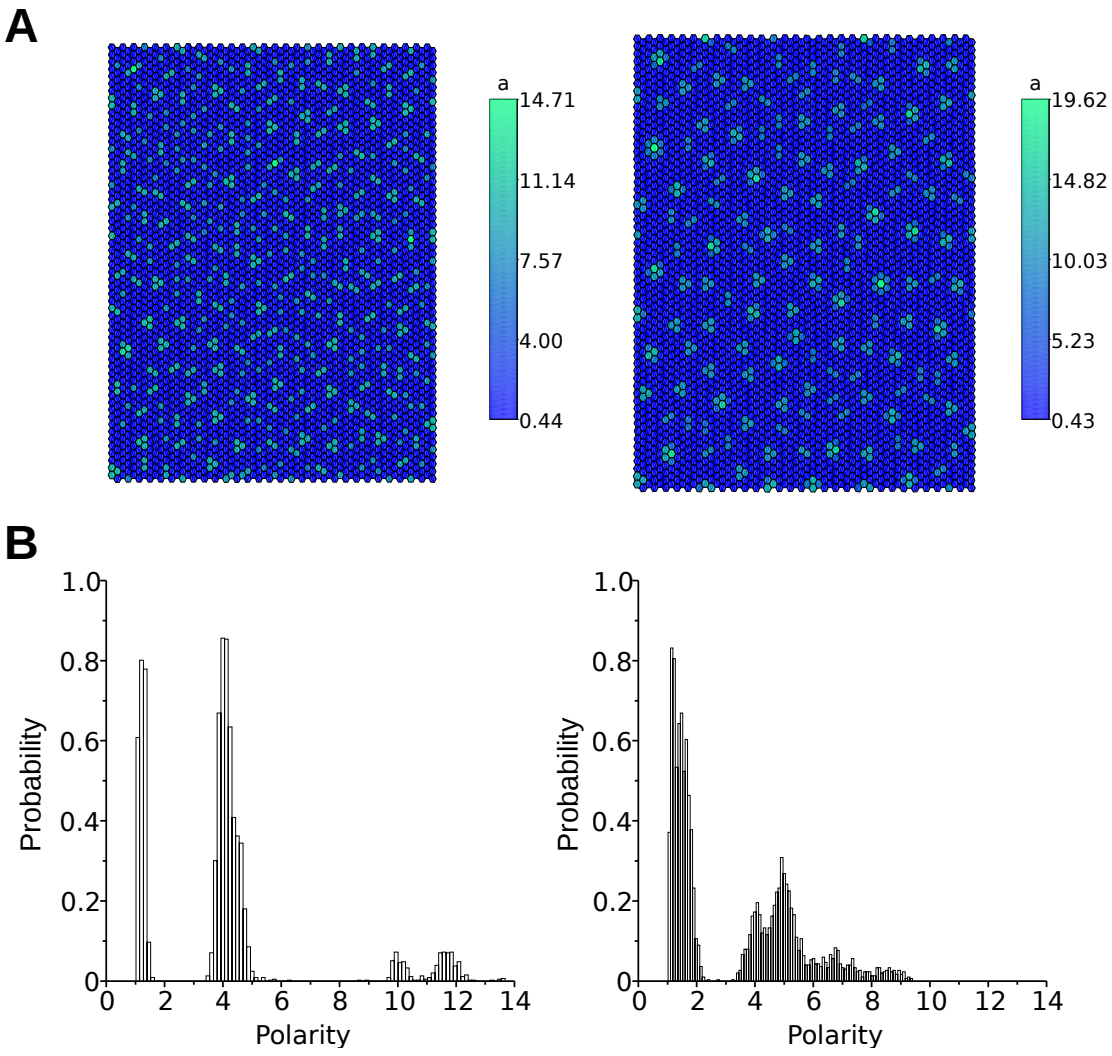

Figure 4.8: **Change in the overall pattern when tension increases:** (A) Tissues are represented for$\sigma/\sigma_0 = 1.41$ (left) and $\sigma/\sigma_0 = 3.55$ (right). Each hexagon is a cell that is colored according to its auxin concentration. The two tissues correspond to the parameters marked by black crosses in Fig. 2C. (B) Probability distributions of the polarity $\mathcal{P}$ computed on the respective tissues.

Dependence of the membrane fraction $\mathcal{F}$ on δk To simulate the effect of pectin methylesterase inhibition, we decrease the parameter δk, with the constraint that $k_{min} + \delta k$ remains constant. By doing so, the dependence of cell wall stiffness with auxin concentration is decreased but the stiffness in

the absence of auxin remains the same. The simulations, presented in Fig. 4.4, show that with the two feedback mechanisms the polarity $\mathcal{P}$ and the membrane fraction of PIN1 $\mathcal{F}$ decrease until the auxin patterns vanish. After the disappearance of the pattern, the simulation results depend on the feedback mechanism. With a stress-based feedback, the fraction $\mathcal{F}$ remains constant, whereas with a strain-based feedback it keeps decreasing. These different behaviors can be explained analytically. In the homogeneous state, the membrane fraction $\mathcal{F}$ of transporters is:

$$\mathcal{F}^{stress} = \frac{K_f^{H_f} \left(\frac{k^*}{k_0}\varepsilon^*\right)^{H_f}}{1 + K_f^{H_f} \left(\frac{k^*}{k_0}\varepsilon^*\right)^{H_f}}$$

$$\mathcal{F}^{strain} = \frac{K_f^{H_f} \left(\varepsilon^*\right)^{H_f}}{1 + K_f^{H_f} \left(\varepsilon^*\right)^{H_f}}$$

where the star indicates the values in the homogeneous state. k^* is given by

$$k^* = k_{min} + \delta k \frac{K_k^{H_k}}{K_k^{H_k} + \left(a^*\right)^{H_k}}$$

If we decrease the value of δk from an initial value δk^0 with the constraint that $k_{min} + \delta k$ remains constant, equal to its initial value $k_{min}^0 + \delta k^0$, k^* is then:

$$k^* = k_{min}^0 + \delta k^0 - \delta k \frac{\left(a^*\right)^{H_k}}{K_k^{H_k} + \left(a^*\right)^{H_k}}$$

Thus k^* is a decreasing function of δk. The deformation of a regular hexagonal lattice of springs with rest length l_0, stiffness k^* and under a tension σ is given by $\varepsilon^* = \frac{\sqrt{3}\sigma l_0}{2k^*}$. In conclusion, the fractions are

$$\mathcal{F}^{stress} = \frac{K_f^{H_f} \left(\frac{\sqrt{3}\sigma l_0}{2k_0}\right)^{H_f}}{1 + K_f^{H_f} \left(\frac{\sqrt{3}\sigma l_0}{2k_0}\right)^{H_f}}$$

$$\mathcal{F}^{strain} = \frac{K_f^{H_f} \left(\frac{\sqrt{3}\sigma l_0}{2k^*}\right)^{H_f}}{1 + K_f^{H_f} \left(\frac{\sqrt{3}\sigma l_0}{2k^*}\right)^{H_f}}$$

These formulas show that $\mathcal{F}^{stress}$ does not depend on δk whereas $\mathcal{F}^{strain}$ actually decreases because k^* increases, The second behavior is consistent with available experimental results [6].

References

[1] I. Adler, D. Barabe, and R. V. Jean. A history of the study of phyllotaxis. *Annals of botany*, 80(3):231–244, 1997.

[2] Evangelia Bellas and Christopher S Chen. Forms, forces, and stem cell fate. *Curr Opin Cell Biol*, 31C:92–97, Sep 2014.

[3] H. R. Bode. Axial Patterning in Hydra. *Cold Spring Harbor Perspectives in Biology*, 1(1):a000463–a000463, July 2009.

[4] Yohann Boutté, Marie-Thérèse Crosnier, Nicola Carraro, Jan Traas, and Béatrice Satiat-Jeunemaitre. The plasma membrane recycling pathway and cell polarity in plants: studies on pin proteins. *J Cell Sci*, 119(Pt 7):1255–65, Apr 2006.

[5] Behruz Bozorg, Pawel Krupinski, and Henrik Jönsson. Stress and strain provide positional and directional cues in development. *PLoS Comput Biol*, 10(1):e1003410, Jan 2014.

[6] Siobhan A. Braybrook and Alexis Peaucelle. Mechano-Chemical Aspects of Organ Formation in Arabidopsis thaliana: The Relationship between Auxin and Pectin. *PLoS ONE*, 8(3):e57813, March 2013.

[7] Vijay Chickarmane, Adrienne H.K. Roeder, Paul T. Tarr, Alexandre Cunha, Cory Tobin, and Elliot M. Meyerowitz. Computational Morphodynamics: A Modeling Framework to Understand Plant Growth. *Annual Review of Plant Biology*, 61(1):65–87, June 2010.

[8] Lance A Davidson. Embryo mechanics balancing force production with elastic resistance during morphogenesis. *Curr Top Dev Biol*, 95:215–41, Jan 2011.

[9] Elena Feraru, Mugurel Ioan Feraru, Jürgen Kleine-Vehn, Alexandre Martinière, Grégory Mouille, Steffen Vanneste, Samantha Vernhettes, John Runions, and Jiří Friml. Pin polarity maintenance by the cell wall in arabidopsis. *Current biology : CB*, 21(4):338–43, Feb 2011.

[10] María Elena Fernández-Sánchez, Sandrine Barbier, Joanne Whitehead, Gaëlle Béalle, Aude Michel, Heldmuth Latorre-Ossa, Colette Rey, Laura Fouassier, Audrey Claperon, Laura Brullé, Elodie Girard, Nicolas Servant, Thomas Rio-Frio, Hélène Marie, Sylviane Lesieur, Chantal Housset, Jean-Luc Gennisson, Mickaël Tanter, Christine Ménager, Silvia Fre, Sylvie Robine, and Emmanuel Farge. Mechanical induction of the tumorigenic β-catenin pathway by tumour growth pressure. *Nature*, 523(7558):92–5, Jul 2015.

[11] T M Freyman, I V Yannas, R Yokoo, and L J Gibson. Fibroblast contractile force is independent of the stiffness which resists the contraction. *Exp Cell Res*, 272(2):153–62, Jan 2002.

[12] Anja Geitmann and Joseph K.E. Ortega. Mechanics and modeling of plant cell growth. *Trends in Plant Science*, 14(9):467–478, September 2009.

[13] Brian Gough. *GNU Scientific Library Reference Manual - Third Edition*. Network Theory Ltd., 3rd edition, 2009.

[14] Olivier Hamant, Marcus G. Heisler, Henrik Jönsson, Pawel Krupinski, Magalie Uyttewaal, Plamen Bokov, Francis Corson, Patrik Sahlin, Arezki Boudaoud, Elliot M. Meyerowitz, and others. Developmental patterning by mechanical signals in Arabidopsis. *science*, 322(5908):1650–1655, 2008.

[15] Olivier Hamant and Jan Traas. The mechanics behind plant development. *New Phytologist*, 185(2):369–385, January 2010.

[16] Marcus G. Heisler, Olivier Hamant, Pawel Krupinski, Magalie Uyttewaal, Carolyn Ohno, Henrik Jönsson, Jan Traas, and Elliot M. Meyerowitz. Alignment between PIN1 Polarity and Microtubule Orientation in the Shoot Apical Meristem Reveals a Tight Coupling between Morphogenesis and Auxin Transport. *PLoS Biology*, 8(10):e1000516, October 2010.

[17] Marcus G. Heisler, Carolyn Ohno, Pradeep Das, Patrick Sieber, Gonehal V. Reddy, Jeff A. Long, and Elliot M. Meyerowitz. Patterns of Auxin Transport and Gene Expression during Primordium Development Revealed by Live Imaging of the Arabidopsis Inflorescence Meristem. *Current Biology*, 15(21):1899–1911, November 2005.

[18] Jonathon Howard, Stephan W Grill, and Justin S Bois. Turing's next steps: the mechanochemical basis of morphogenesis. *Nature Reviews Molecular Cell Biology*, 12(6):400–6, Jun 2011.

[19] Thomas Iskratsch, Haguy Wolfenson, and Michael P Sheetz. Appreciating force and shape - the rise of mechanotransduction in cell biology. *Nat Rev Mol Cell Biol*, Oct 2014.

[20] Steven G. Johnson. *The NLopt nonlinear-optimization package*, 2010.

[21] Henrik Jönsson, Marcus G. Heisler, Bruce E. Shapiro, Elliot M. Meyerowitz, and Eric Mjolsness. An auxin-driven polarized transport model for phyllotaxis. *Proceedings of the National Academy of Sciences of the United States of America*, 103(5):1633–1638, 2006.

[22] Shigeru Kondo. The reaction-diffusion system: a mechanism for autonomous pattern formation in the animal skin. *Genes to Cells*, 7(6):535–541, 2002.

[23] Cris Kuhlemeier and Didier Reinhardt. Auxin and phyllotaxis. *Trends in plant science*, 6(5):187–189, 2001.

[24] Loïc Legoff, Hervé Rouault, and Thomas Lecuit. A global pattern of mechanical stress polarizes cell divisions and cell shape in the growing drosophila wing disc. *Development*, 140(19):4051–9, Oct 2013.

[25] Ladislav Luksan. *New subroutines for large-scale optimization*, 2007.

[26] Alexandre Martinière, Irene Lavagi, Gayathri Nageswaran, Daniel J Rolfe, Lilly Maneta-Peyret, Doan-Trung Luu, Stanley W Botchway, Stephen E D Webb, Sebastien Mongrand, Christophe Maurel, Marisa L Martin-Fernandez, Jürgen Kleine-Vehn, Jirí Friml, Patrick Moreau, and John Runions. Cell wall constrains lateral diffusion of plant plasma-membrane proteins. *P Natl Acad Sci Usa*, Jun 2012.

[27] Pascale Milani, Siobhan A Braybrook, and Arezki Boudaoud. Shrinking the hammer: micromechanical approaches to morphogenesis. *J Exp Bot*, 64(15):4651–62, Dec 2013.

[28] Démosthène Mitrossilis, Jonathan Fouchard, David Pereira, François Postic, Alain Richert, Michel Saint-Jean, and Atef Asnacios. Real-time single-cell response to stiffness. *Proceedings of the National Academy of Sciences of the United States of America*, Sep 2010.

[29] Bruno Moulia, Catherine Coutand, and Jean-Louis Julien. Mechanosensitive control of plant growth: bearing the load, sensing, transducing, and responding. *Frontiers in Plant Science*, 6, February 2015.

[30] Naomi Nakayama, Richard S. Smith, Therese Mandel, Sarah Robinson, Seisuke Kimura, Arezki Boudaoud, and Cris Kuhlemeier. Mechanical Regulation of Auxin-Mediated Growth. *Current Biology*, 22(16):1468–1476, August 2012.

[31] Alan C. Newell, Patrick D. Shipman, and Zhiying Sun. Phyllotaxis: Cooperation and competition between mechanical and biochemical processes. *Journal of Theoretical Biology*, 251(3):421–439, April 2008.

[32] Kiyotaka Okada, Junichi Ueda, Masako K. Komaki, Callum J. Bell, and Yoshiro Shimura. Requirement of the auxin polar transport system in early stages of Arabidopsis floral bud formation. *The Plant Cell Online*, 3(7):677–684, 1991.

[33] Klaus Palme and Leo Gälweiler. PIN-pointing the molecular basis of auxin transport. *Current opinion in plant biology*, 2(5):375–381, 1999.

[34] Alexis Peaucelle, Siobhan A Braybrook, Laurent Le Guillou, Emeric Bron, Cris Kuhlemeier, and Herman Höfte. Pectin-induced changes in

cell wall mechanics underlie organ initiation in arabidopsis. *Current biology : CB*, Oct 2011.

[35] Alexis Peaucelle, Romain Louvet, Jorunn N. Johansen, Herman Höfte, Patrick Laufs, Jérome Pelloux, and Grégory Mouille. Arabidopsis Phyllotaxis Is Controlled by the Methyl-Esterification Status of Cell-Wall Pectins. *Current Biology*, 18(24):1943–1948, December 2008.

[36] Beth L Pruitt, Alexander R Dunn, William I Weis, and W James Nelson. Mechano-transduction: from molecules to tissues. *Plos Biol*, 12(11):e1001996, Nov 2014.

[37] Matteo Rauzi and Pierre-François Lenne. Cortical forces in cell shape changes and tissue morphogenesis. *Curr Top Dev Biol*, 95:93–144, Jan 2011.

[38] Didier Reinhardt, Therese Mandel, and Cris Kuhlemeier. Auxin regulates the initiation and radial position of plant lateral organs. *The Plant Cell Online*, 12(4):507–518, 2000.

[39] Didier Reinhardt, Eva-Rachele Pesce, Pia Stieger, Therese Mandel, Kurt Baltensperger, Malcolm Bennett, Jan Traas, Jiří Friml, and Cris Kuhlemeier. Regulation of phyllotaxis by polar auxin transport. *Nature*, 426(6964):255–260, 2003.

[40] Peter Ryden, Keiko Sugimoto-Shirasu, Andrew Charles Smith, Kim Findlay, Wolf-Dieter Reiter, and Maureen Caroline McCann. Tensile properties of arabidopsis cell walls depend on both a xyloglucan cross-linked microfibrillar network and rhamnogalacturonan ii-borate complexes. *Plant Physiol*, 132(2):1033–40, Jun 2003.

[41] Alexandre Saez, Axel Buguin, Pascal Silberzan, and Benoît Ladoux. Is the mechanical activity of epithelial cells controlled by deformations or forces? *Biophysical Journal*, 89(6):L52–4, Dec 2005.

[42] Patrik Sahlin, Bo Söderberg, and Henrik Jönsson. Regulated transport as a mechanism for pattern generation: Capabilities for phyllotaxis and beyond. *Journal of Theoretical Biology*, 258(1):60–70, May 2009.

[43] Arun Sampathkumar, An Yan, Pawel Krupinski, and Elliot M. Meyerowitz. Physical Forces Regulate Plant Development and Morphogenesis. *Current Biology*, 24(10):R475–R483, May 2014.

[44] Massimiliano Sassi, Olivier Ali, Frédéric Boudon, Gladys Cloarec, Ursula Abad, Coralie Cellier, Xu Chen, Benjamin Gilles, Pascale Milani, Jiří Friml, Teva Vernoux, Christophe Godin, Olivier Hamant, and Jan Traas. An Auxin-Mediated Shift toward Growth Isotropy Promotes Organ Formation at the Shoot Meristem in Arabidopsis. *Current Biology*, 24(19):2335–2342, October 2014.

[45] Scilab Enterprises. *Scilab: Free and Open Source software for numerical computation*. Scilab Enterprises, Orsay, France, 2012.

[46] Richard S. Smith and Emmanuelle M. Bayer. Auxin transport-feedback models of patterning in plants. *Plant, Cell & Environment*, 32(9):1258–1271, September 2009.

[47] Richard S. Smith, Soazig Guyomarc'h, Therese Mandel, Didier Reinhardt, Cris Kuhlemeier, and Przemyslaw Prusinkiewicz. A plausible model of phyllotaxis. *Proceedings of the National Academy of Sciences of the United States of America*, 103(5):1301–1306, 2006.

[48] Teva Vernoux, Jocelyne Kronenberger, Olivier Grandjean, Patrick Laufs, and Jan Traas. PIN-FORMED 1 regulates cell fate at the periphery of the shoot apical meristem. *Development*, 127(23):5157–5165, 2000.

[49] Ai Kia Yip, Katsuhiko Iwasaki, Chaitanya Ursekar, Hiroaki Machiyama, Mayur Saxena, Huiling Chen, Ichiro Harada, Keng-Hwee Chiam, and Yasuhiro Sawada. Cellular response to substrate rigidity is governed by either stress or strain. *Biophys J*, 104(1):19–29, Jan 2013.

[50] Marta Zwiewka, Tomasz Nodzyński, Stéphanie Robert, Steffen Vanneste, and Jiří Friml. Osmotic stress modulates the balance between exocytosis and clathrin-mediated endocytosis in arabidopsis thaliana. *Mol Plant*, 8(8):1175–87, Aug 2015.

Chapter 5

A mechanics-based rule accounts for the orientation of cell division in the shoot apical meristem of Arabidopsis Thaliana

5.1 Summary

In the previous chapter, we studied how a coupling between biochemical and mechanical fields generates the patterns of growth hormone that lead to the positioning the plant organs. In this chapter, we study the impact of mechanics on cell divisions, which are intrinsically related to growth and could constitute an additional layer of control of the shape of the tissue. The balance between growth and divisions determine the average size of the cells. It also determines their shape: most of the time, plant cells tend to build new cell walls so that they are short, that is by dividing the cells perpendicularly to their long axis, and consequently limiting their geometrical anisotropy. Divisions are especially important for plants, who lack two major mechanisms used by animal cells to control their shapes and topologies: plant cells are glued together, unable to migrate, and young tissues are not subject to cell death.

A few years ago, Sebastien Besson and Jacques Dumais [4] have formulated a probabilistic model for the prediction of division orientation based on cell shape. The main assumptions is that a cell contains a constant number S of endoplasmic microtubules. A number s^j of microtubules connect the nucleus to the cell wall j, $j \in [1; N]$. We note $x^j = s^j/S$ the fraction of microtubules attached to j. Thus the entropy of a given configuration $\{x^j\}_{j\in[1;N]}$ is given by

$$H\left(x^1, ..., x^N\right) = - \sum_{j\in \text{ cell walls}} x^j \ln\left(x^j\right)$$

If A is the area of the cell and $\rho = \sqrt{A}$ its mean cell diameter, $< d >$ is related to ρ via a constant c to be determined experimentally. Thus,

$$< d >= c\rho = \sum_{j \in \text{ cell walls}} x^j d^j$$

where d^j is the distance between the nucleus and the cell wall j. Finally, maximizing the entropy H with respect to the configuration $\{x^j\}_{j\in[1;N]}$ gives

$$x^j = \frac{\exp\left(-\beta d^j/\rho\right)}{Z}$$

where $Z = \sum_j - \beta d^j/\rho$ is the partition function of the system and β a constant. Experiments indicate that during a division the new cell wall forms between the walls that receive more microtubules. The probability of observing a division between the walls j and k is thus given by

$$p^{jk} = \frac{x^j x^k}{\sum_{(u,v)\in \text{ pairs of walls}} x^u x^v}$$

Finally, assuming that the length of the new cell wall i, forming between the cell walls j and k, is approximately $l^i = d^j + d^k$, its probability is

$$P^i = p^{uv} = \frac{\exp\left(-\beta l^i/\rho\right)}{Z'}$$

where the new partition function is $Z' = \sum_j - \beta l^i/\rho$.
This project starts with a simple observation. The geometrical rule of Besson and Dumais seems to be contradicted in the apex of *Arabidopsis Thaliana*. There, young organs emerge from the meristem, a group of fast-growing undifferentiated cells. In the boundary between a young organ and the meris-

tem, cells seem to have a higher shape anisotropy than in the surrounding tissues. Such shapes seem incompatible with divisions oriented by geometrical cues such as mentioned above. It appears that the meristem and the young organ are characterized by high growth rates, compared with the boundary. Additionally, their dome shapes make their curvature isotropic, whereas the boundary has a saddle shape, that is an anisotropic curvature. These two observations both suggest that the boundary undergoes an anisotropic mechanical stress, tensile in its own direction and compressive in the orthogonal direction. This particular mechanical identity led us to the hypothesis that mechanics could explain the bias toward divisions that are "unlikely" according to the usual geometrical cues.

To investigate this possibility, I implemented a mathematical model describing tissue growth. Vertex models as described in the introduction section have been proven well-suited to study the mechanics of epithelial tissues. I used such a model to mimic a boundary, by including either growth heterogeneities or external anisotropic stretching to the equations. I performed simulations where divisions are oriented by the geometry of the cells or by their mechanical stresses. They were compared with experimental data by analyzing both simulated and real tissues with an algorithm published a few years ago and computing the possible divisions and their probability according to the geometrical cues. We show that dividing the cells along the maximal mechanical tension can explain the bias in the boundary. Additionally, we performed cell ablations. They are known to create circumferential stress around the ablated cell, and we observed both the reorientation of tension in the simulations and the reorientations of divisions in real tissues.

My contribution to this project was the development of the model and its

implementation. I wrote the parts of the paper about our model and the previous models studying cell division rules in the plant shoot. All the authors were involved in the discussion about the interpretation of the results, and the preparation of the manuscript.

5.2 Paper

A mechanics-based rule accounts for the orientation of cell division in the boundary of the shoot apical meristem of *Arabidopsis thaliana*

Marion Louveaux[1,2], Jean-Daniel Julien[1,2,3], Vincent Mirabet[1,2], Arezki Boudaoud[1,2], and Olivier Hamant[1,2]

[1]Laboratoire Reproduction et Développement des Plantes, [2]Laboratoire Joliot-Curie, and [3]Laboratoire de Physique, ENS Lyon, 46 allée d'Italie, Lyon Cedex 07, France

Abstract

Regulation of cell division plane orientation is a way for multicellular organisms to control the topology and geometry of their tissues, in particular in plant, where cells are glued to each other by stiff pectocellulosic cell walls. At the end of the XIX^{th} century, cell geometry was proposed to play a key role in cell division plane orientation and several geometrical division rules were proposed by Hofmeister, Errera and Sachs. However none of these deterministic rules describes all the divisions at the shoot apical meristem (SAM) of *Arabidopsis thaliana*. Recently, the rule of Errera was re-examined and generalized into a probabilistic rule: the Besson-Dumais rule. The Besson-Dumais rule has been tested only on tissues with rather isotropic shapes or

growth and the exact molecular mechanism controlling division plane orientation is still unknown. In the present paper, we tested the application of Besson-Dumais rule to the divisions at the SAM of *Arabidopsis thaliana*, which present both isotropic and anisotropic regions. We found that a non negligible proportion of cells do not choose the shortest plane at the epidermis of the SAM. The Besson-Dumais division rule partially accounted for observations but long plane were over-represented, in particular in the boundary region. We simulated growing tissues submitted to anisotropic stress and compared two division rules: geometrical or mechanical based. We found that the mechanical rule reproduced the enrichment of long planes observed in the boundary and thus better accounted for cell divisions in this region. We could correlate a bias in division plane orientation with an experimental perturbation of mechanical stress pattern by laser ablation. We also simulated tissues submitted to isotropic stress. We found that the mechanical rule reproduced the plane distribution observed in other regions of the SAM. Thus mechanical rule predicts better planes at the SAM.

5.3 Introduction

Regulation of cell division plane orientation is a way for multicellular organisms to control the topology (number of neighbors) and geometry (cell shapes and sizes) of their tissues, as highlighted by simulations of growing tissue under different division rules (see for instance [20]). Whereas this process may be compensated by cell death and cell rearrangement in animal tissues, this is an essential mechanism in plants: plant cells are glued to each other by stiff pectocellulosic cell walls, which prevent cell movement, while cell death does not occur in young, rapidly dividing tissues.

At the end of the XIX^{th} century, Hofmeister, Errera and Sachs proposed cell geometry as a spatial cue guiding cell division plane orientation, at least for symmetric cell divisions [11, 19, 7]. In particular, Léo Errera observed that cells behaved like soap bubbles when positioning their division plane, i.e. they tend to minimize the length of new interfaces between daughter cells. From this statement was derived the rule of Errera: "cells divide along the shortest path", which is a rough simplification of Errera's initial observation (for a full review, see [5]). The rules of Hofmeister, Errera (simplified version) and Sachs were recently tested at the shoot apical meristem (SAM) of *Arabidopsis thaliana[22]*. None of these rules fully described all the divisions at the SAM, but Errera's rule was the one which described the highest percentage of divisions.

Errera's exact statement was recently reexamined and the deterministic "shortest path" rule was generalized in a probabilistic one by Sébastien Besson and Jacques Dumais [4]. Here this rule will be referred as the Besson-Dumais rule. Like soap bubbles, cells do not always choose the shortest path, but one

of the shortest. For a given cell geometry, several minima of energy exist and the probability to divide along one of these minima is related to the length of the interface. However, the Besson-Dumais rule has only been tested on tissues with rather isotropic shapes or growth, like the thallus of the green alga *Coleochaete orbicularis*, whereas most of the epithelia have a 3D shape and a non isotropic growth. Moreover, the molecular mechanism behind this rule remains speculative and limited to vacuolated cells: it was proposed to involve minimization of tension within cytoplasmic strands of vacuolated cells [4]. Cytoplasmic strands are populated with microtubules, guide the relocation of nucleus at the cell center of mass prior to division and coalesce into the phragmosome at the future division site. Such a mechanism would suggest that the reorganization of interphasic microtubules into the preprophase band (PPB) is primarily driven by cytoplasmic strands. The PPB circles the nucleus prior to division and marks the future division site. Its formation requires the presence of TONNEAU1 and TONNEAU2. PPB disappears concomitantly with nuclear breakdown but its former localization is kept by the persistence of several molecular actors, such as TANGLED and POK, which are involved in phragmoplast guidance at division site. The *tonneau*, *tangled* and *pok* mutants exhibit defects in division plane orientation[25, 16, 27]. Finally epithelial cells are exposed to different patterns of biochemical factors and mechanical stress. Microtubules are able to sense supracellular mechanical stress, as they were shown to align along maximal tensile stress direction in the boundary domain of the SAM of *Arabidopsis thaliana* [9]. And auxin signaling through the Aux/IAA factor BODENLOS was recently shown to bias Errera's rule towards longer division planes in young embryos [28]. How this heterogeneity and dynamics impact cell division plane orientation has

not been characterized quantitatively yet.

In the present paper, we tested the application of Besson-Dumais rule to the divisions at the shoot apical meristem (SAM) of *Arabidopsis thaliana*, which present both mechanically isotropic and anisotropic regions. We found that a non negligible proportion of cells did not choose the shortest plane at the epidermis of the SAM. The Besson-Dumais division rule partially accounted for observations but long plane were over-represented, in particular in the boundary domain. We simulated growing tissues submitted to anisotropic stress and compared two division rules: geometrical or mechanical based. We found that the mechanical division rule reproduced the enrichment of long planes observed in the boundary and thus better accounted for cell divisions in this region. We also simulated tissues submitted to isotropic stress. However, in these tissues, we could not found a perfect match between outputs of simulations with a mechanical rule and observed divisions in isotropic domains of the SAM.

5.4 Results

5.4.1 A non negligible proportion of cells does not select the shortest plane at the epidermis of the SAM

We analyzed cell division plane orientations at the epidermis of the shoot apical meristem of *Arabidopsis thaliana* with the plane classification used in the Besson-Dumais rule. We acquired confocal images of *LTi6B-GFP* (WS-4) dissected meristems every 12h during 48h (Fig. 5.1A). On each snapshot, 3D surface was reconstructed and segmented with MorphoGraphX to extract

cell shapes (see Material and Methods and Fig. 5.1B). New cell walls were identified by a visual comparison between snapshots (from T=12h to T=48h). We hypothesized that cell shape did not change much immediately after division and thus that the recorded cell wall position between the two daughter cells corresponded to the position of the former PPB in the mother cell. The Besson-Dumais rule applies only to symmetrically dividing cells. Comparison of the areas of the two daughter cells, computed on the 3D surface, showed that 78h of the cells within the SAM divided almost equally, i.e. the smallest daughter cell occupying between 40% and 50% of the sum of the two daughters areas (see Fig. 5.6B in §5.7 Supplemental Figures). The 22% of asymmetrical dividing cells were located preferentially in the meristem region of the SAM (see Fig. 5.6C in §5.7 Supplemental Figures, and Fig. 5.2A for the definition of SAM regions). In the following, these asymmetrically dividing cells are removed from analysis, to be in line with the Besson and Dumais rule. The Besson and Dumais rule is defined only in 2D. Epidermis of the SAM has an almost constant thickness of around $5\mu m$ and new cell walls in this layer are perpendicular, e.g. anticlinal, to the surface (Fig. 5.6A and Fig. S1 in [26]). Thus we could restrict our analysis to 3D surface of the SAM. Although SAM surface is curved (Fig. 5.1C and Fig. 5.6A), the surface of the pair of daughter cells is small enough compared to the variations of curvature to be locally flattened in 2D without too much shape deformations (see Material and Methods and Fig. 5.7).

We computed predictions of the Besson-Dumais rule using Sébastien Besson's Matlab script (see Material and Methods). This script is later referred as Besson script. For each cell, the Besson script seeks the shortest plane between each pair of edges that divide equally the mother's area (e.g., on our

dataset, the fused daughter cells area). It happens that the Besson script do not find any solution satisfying the condition on area for a given pair of edges. All possible planes are ranked from the shortest to the longest. The probability P_i to divide along a given plane i depends on the length of the plane and takes the form [4]:

$$P_i = \frac{e^{-\beta \ell_i / \rho}}{\sum_{j=1}^{N} e^{-\beta \ell_j / \rho}} \tag{5.1}$$

where ℓ_i is the length of plane i, ρ the mean cell diameter, β a constant and N the total number of theoretical possible planes of the cell.

The Besson script also compares theoretical predictions to observations and give the rank of the observed plane and its probability P_i to be chosen among other possibilities (Fig. 5.1F and Fig. 5.8). More precisely, the Besson script compares pair of edges connected to predicted cell walls to the pair of edges connected to the observed cell wall. In only 5 to 8% of the cases (depending on SAM), the Besson script did not find a match between observations and theoretical predictions (Fig. 5.1G). These observed planes are referred as NP for "not predicted" (by Besson script). By opposition, other planes are referred as predicted planes.

As cells in the SAM display different shapes and shape anisotropy and as the number of possible planes may vary from one cell to another, ranks are not sufficient to compare cells. As shown in Fig. 5.8A-B, the shortest plane (rank=1) in an elongated cell (Fig. 5.8A) has a higher probability P_1 to be observed than the shortest plane (rank=1 also) of a roundish cell (Fig. 5.8B). And the longest plane of the cell showed in Fig. 5.8C (rank=9) has a higher probability to be observed than the longest plane of the cell showed in Fig. 5.8D (rank=4).

In order to compare cells with one another, we compared all predicted planes of a given cell with the shortest predicted plane of this cell: we computed the pairwise probability p_{pw} between the shortest predicted plane of length ℓ_1 (e.g. Errera's predicted plane) and the observed plane of length ℓ_{obs}, with $\ell_1 \leq \ell_{\text{obs}}$ as the ratio between the probability P_{obs} of observed plane and the sum of the probabilities P_{obs} and P_1 (probability to observe the shortest plane):

$$p_{\text{pw}} = \frac{P_{\text{obs}}}{P_1 + P_{\text{obs}}} \tag{5.2}$$

Pairwise probability p_{pw} varies between 0 (long plane) and 0.5 (short plane). When observed plane is the shortest one (as for instance in Fig. 5.8A-B), pairwise probability is strictly equal to 0.5.

We defined 5 classes of pairwise probability: $= 0.5$; $[0.375; 0.5[$; $[0.250; 0.375[$; $[0.125; 0.250[$;$[0.; 0.125[$ and added a 6^{th} class, when no match between theoretical predictions and observations had been found. These classes are later referred as planes classes. The first class correspond to the choice of the shortest plane by the cell. Planes classes are not strictly equivalent to ranks, but they are independent of cell shape (Fig. 5.9).

Proportions of planes classes between meristems are similar but not identical (Fig. 5.1G). In each SAM, 65 to 77% of all planes, (corresponding to 68 to 81% of predicted planes), correspond to the shortest.

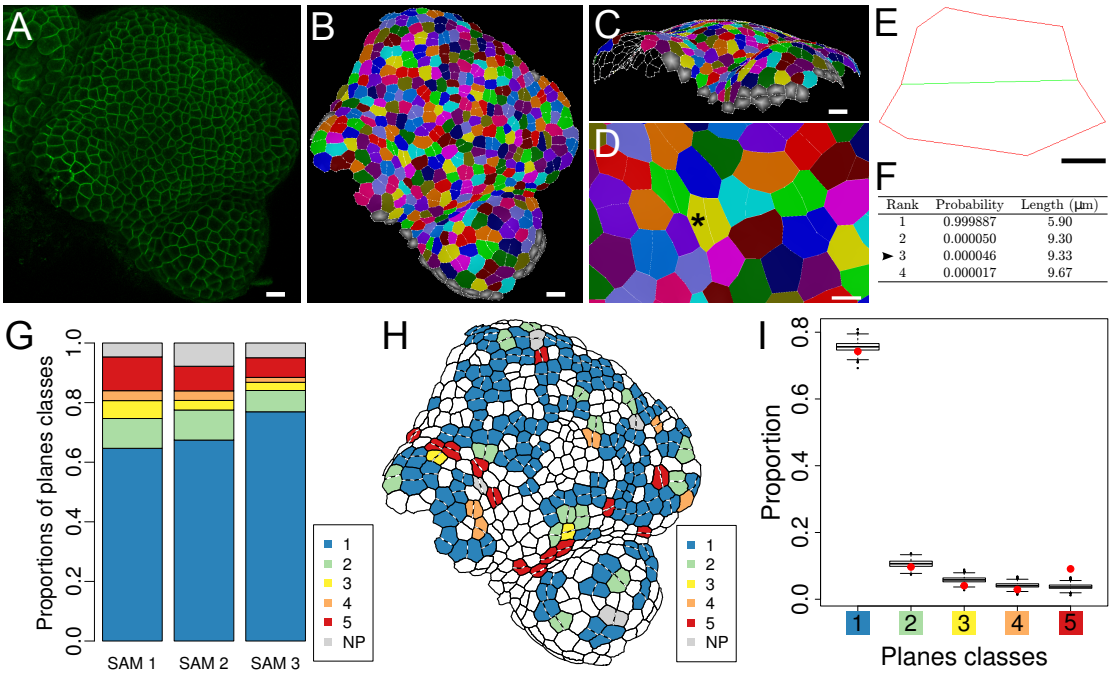

Figure 5.1: **Division planes at the shoot apical meristem of *Arabidopsis thaliana*.** (A) Confocal image of *LTi6B-GFP* (WS-4) dissected shoot apical meristem. Scale bar=$10\mu m$. (B) Cellular segmentation of the shoot apical meristem with MorphoGraphX. Cells sharing the same color are daughters from a division which occurred during the last 12h. Scale bar=$10\mu m$. (C) Segmentation is done on 3D surface. Scale bar=$10\mu m$. (D) Close up of (B) in a young boundary region. The black asterisk points at a mother cell (e.g. two fused daughter cells) which is analyzed with Besson script in panels (E) and (F). Scale bar=$5\mu m$. (E) Flattened mother cell. Only the main vertices (i.e. at the junction between three cells) are kept. The new plane is coloured in green. Scale bar=$5\mu m$. (F) Planes predicted by the Besson script for cell (E). The arrowhead indicates that the observed plane in cell (E) corresponds to predicted plane of rank three. $p_{\text{PW}} = 4 \times 10^{-11}$, e.g. this cell belongs the 5^{th} plane class of pairwise probability. (G) Proportion of planes classes in each SAM (total number of symmetrically dividing cells in SAM1, 2 and 3 is respectively 150, 218 and 182). Classes 1 to 5 correspond to the ratio between the probability for a cell to choose the observed planes and the probability to choose the shortest plane, as predicted by the Besson script. Ratio varies from 0 to 0.5. Class 1 $[= 0.5]$ corresponds to the choice of the shortest plane and Class 5 $[0; 0.125[$ corresponds to the choice of one of the longest planes. NP (not predicted) corresponds to an absence of match between theoretical predictions and observations. (H) Map displaying planes classes for the divisions which occurred in the 12h following this snapshot. (I) Comparison of observed planes proportions within the different classes (red dots) with fluctuation range obtained by bootstrap among theoretical predictions given by the Besson script (boxplots). Planes which did not match prediction (NP class) were excluded from this analysis. Total number of symmetrically dividing cells: 517.

5.4.2 The Besson-Dumais division rule partially accounts for observations, but long planes are over-represented at the SAM

When compared to elongated cells of the hypocotyl, meristematic cell shapes are rather isotropic; this could explain the relatively high proportion of cell not dividing along the shortest plane in the shoot apical meristem. To test this hypothesis, we computed the range of fluctuation of the proportion of each planes class and compared to observed proportions. To compute the range of fluctuation of the proportion of each planes class, we used a bootstrap approach to produce theoretical set of planes corresponding to the observed tissue geometry. To compute a particular set of planes, for each dividing cell that had chosen a plane predicted by the Besson script, we sampled a new plane among the theoretical predictions given by the Besson script. The probability to sample this plane i was equal to the probability P_i described above. We then computed the pairwise probability p_{pw} between the shortest predicted plane of length ℓ_1 and the sampled plane s of length ℓ_s, with $\ell_1 \leq \ell_s$. We obtained a first set of simulated pairwise probabilities and computed the frequencies of each class, using the planes classes defined previously. We repeated this procedure a thousand time to generate a thousand sets of planes and the corresponding proportions. We plotted boxplots of proportions for each plane class and added our observed proportions (red dots) on the same graph (Fig. 5.1I). The boxplot (with its notches) represents a confidence interval at 95%. For a given plane class, if observation dot is out of the boxplot, the probability to get this proportion of planes is lower than 5%. Here, the probability to get observed proportions of planes classes 1 to 4 are is above

5%, whereas the probability to get observed proportion of class 5 is below 5%. This result indicates that long planes are over-represented at the shoot apical meristem of *Arabidopsis thaliana* and that the Besson-Dumais rule only partially accounts for observed planes.

5.4.3 The boundary region is enriched in long planes

We spatialized results of the bootstrap analysis to evaluate the impact of tissue anisotropy on planes classes proportions. Three regions were defined manually: the meristem, which corresponds to the central zone and peripheral zone, the outgrowing primordia and the boundary, between primordia and meristem (Fig. 5.2A). Meristem and primordia have a rather isotropic shape and growth, compared to the boundary, which is creased and characterized by a lower growth rate when compared to surrounding tissues [13]. Cell localization was identified on the timepoint preceding cell division. In the primordia, proportions of planes classes were found to be within the confidence interval, showing a good agreement between predictions of Besson-Dumais rule and observed planes (Fig. 5.2B-C). In the meristem, as in the whole tissue, the the probability to get the observed proportion of planes of class 5 was lower than 5%. The proportion of long planes was higher than expected. This could be due to our restrictive definition of the boundary regions. In the boundary, the probability to get the observed proportion of planes of class 1, 4 and 5 was lower than 5% (Fig. 5.2D). In this region, proportion of planes of class 1 was lower than expected and proportion of planes of class 4 and 5 higher.

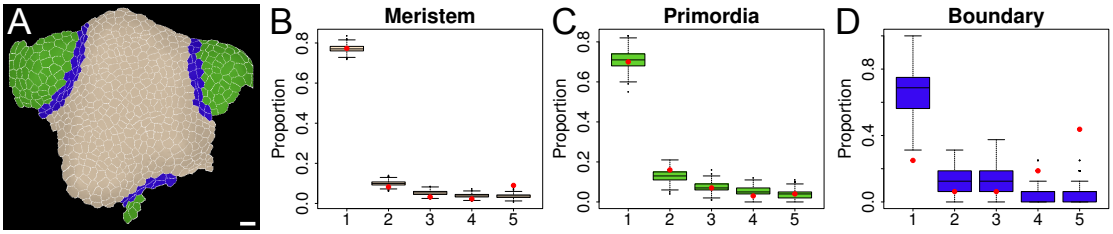

Figure 5.2: **A domain-based comparison between observations at the SAM and predictions of the Besson-Dumais rule.** (A) Example of expert manual definition of the boundary domain (blue), the meristem domain (beige) and the primordia domains (green). (B-D) Comparison of observed planes proportions (red dots) with fluctuation range obtained by bootstrap among theoretical predictions given by the Besson script (boxplots), displayed in function of regions: (B) Meristem, (C) Primordia and (D) Boundary. Planes that were not predicted by the Besson script (NP planes) were excluded from this analysis. Number of symmetrically dividing cells in these regions is respectively: 401, 100 and 16.

5.4.4 Simulation of a growing boundary suggests a contribution of mechanical stress to the bias in the division plane distribution

Boundaries have a very specific identity compared to other part of the SAM, both genetically and mechanically. In particular, the boundary domain is defined by the expression of specific transcription factors [1, 18], hormonal levels (e.g. [10, 6] and highly anisotropic tensile stress [9]. Dissecting the different factors contributing to the boundary identity and identifying the ones that are involved in this bias is thus complex. Simulations offer the possibility to simplify the system and test alternative and integrative hypotheses, notably by focusing on tissue geometry.

We used a vertex model that allowed to compute the mechanics and the geometry of the tissue at the cellular scale. The tissue is a two dimensional

lattice of growing and dividing cells. Cells behave like rubber balloons, with a certain wall elasticity, under (turgor) pressure. They are packed together and thus cannot reach their optimal shape. Additional mechanical stress either emerges from differential growth (growth-derived stress) or is imposed as an anisotropic mechanical stress, mimicking shape-derived stress that are prescribed by the anisotropic curvature of the boundary (curvature-derived stress). In the growth-derived stress simulations, a ring of slow-growing cells surrounds a disc of fast-growing cells. Growth (e.g. displacement of vertices) is computed by minimizing the energy of the tissue, which is a balance between pressure and curvature and elasticity of cell walls resisting to this tension. Cells divide when reaching a certain size threshold. In all the simulations, the new division plane goes through the barycenter of the cell. Two division rules were tested: either the new division plane follows the direction of the short axis of the cell (the geometrical division rule) or it follows the direction of local maximal tensile stress (the mechanical division rule). These defined four cases of study: growing tissue following either geometrical or mechanical division rule, undergoing either growth-derived or curvature derived stress. Mechanical stress field is anisotropic to mimic the boundary region: growth is three times higher in the central disc than in the surrounding ring or force is three times higher along x axis than along y axis.

We computed cells' aspect ratio (ratio of short over long axis of the cell) in the different simulated tissues. When tissue was submitted to anisotropic mechanical stress, the geometrical division rule produced tissues with rather isotropic cells' aspect ratio, whether the mechanical division rule produced tissues with more anisotropic cell's aspect ratio (Fig. 5.10B). In this last case, anisotropic cell shapes were mostly located at the interface between the fast

and slow growing tissues in the differential growth simulations, and along maximal tensile stress in anisotropic curvature simulations. In comparison, at the SAM, mean cell aspect ratio is equal to 0.74. Boundary cells have a more anisotropic shape in average, with a mean aspect ratio of 0.58, compared to meristem and primordia cells (mean aspect ratio of 0.76, see Fig. 5.10A). Thus, the mechanical division rule produced tissues with an aspect ratio close (in average) to those of meristem and primordia when stress field was isotropic, and close (in average) to those of boundary regions when stress field was anisotropic (Fig. 5.10B compared to Fig. 5.10A). However, whereas mean aspect ratio do not differ much between dividing and non dividing cells (e.g. will or will not divide in the next 12h in the meristem and primordia, mean aspect ratio of boundary cells is higher (0.74) for dividing cells compared to non dividing cells (0.58) (Fig. 5.10A). Thus, aspect ratio do not differ much between dividing cells of the different regions. Results of simulations were filtered on cell aspect ratio: only cells with an aspect ratio superior to 0.5 were kept in the analysis.

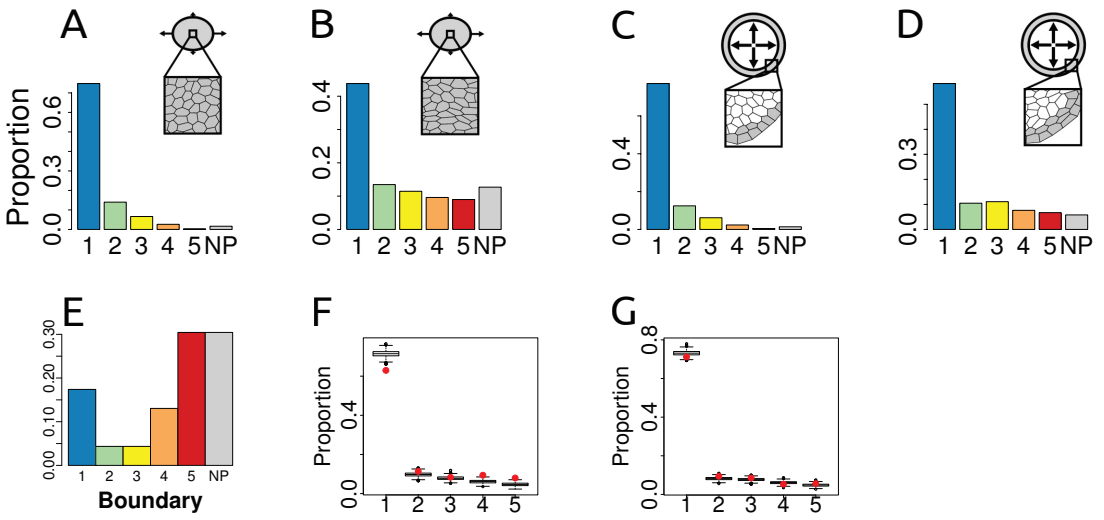

Figure 5.3: **Comparison of two division rules in a simulated boundary region.** Planes classes proportions in the different simulated growing tissue, either submitted to curvature-derived (top) or growth-derived (bottom) anisotropic stress and a geometrical (left) or mechanical division rule (right). Comparison of observed planes proportions in simulated tissues (red dots) with fluctuations range obtained by bootstrap among theoretical predictions given by the Besson script (boxplot), in a curvature-derived (top) or growth-derived (bottom) anisotropic stress field.

We applied the Besson script on the output of simulated tissues to compute predictions of Besson-Dumais rule and match with observed division planes. We computed pairwise probabilities between observed plane and shorter predicted plane and subdivided this variable into the 6 classes defined previously in §5.4.1 (Fig. 5.3A-D). Tissues simulated with the geometrical rule, both in growth- and curvature-derived stress, displayed a majority of short planes, as expected. The implemented geometrical division rule mimics Errera's simplified shortest path rule, but do not follow exactly the same conditions: division plane orient along short axis of the cell, with a straight cell walls going through the barycenter of the cell, but without condition on the equality of daughters area. This difference may explain the existence of planes in the

class 2 to 5. Tissues simulated with the mechanical division rule displayed a higher proportion of long planes than tissues simulated with the geometrical rule, and a higher proportion of non predicted planes (NP).

We spatialized proportion of planes classes in function of regions of the SAM. The boundary had a lower proportion of short planes and and higher proportion of long planes, as observed in the simulations of growing tissues undergoing anisotropic stress field and following a mechanical division rule. However, the we could also observe a peak for the planes of the class 5 and of non predicted planes (NP), which was not observed in simulations (Fig. 5.3E).

We applied the same bootstrap approach described in §5.4.2 on tissues simulated with the mechanical division rule to see how far this rule was from Besson-Dumais rule predictions in anisotropic cases and to confirm depletion in planes of class 1 and enrichment of planes of class 5, as observed in the boundary region of the SAM (Fig. 5.2D). In curvature-derived anisotropic stress fields we observed a depletion in planes of class 1 and an enrichment of planes of class 5, with a probability lower than 5% to get these two proportions (Fig. 5.3F), similar to what was observed in the boundary region of the SAM (Fig. 5.2D). We did not observe the same bias in growth-derived anisotropic stress fields, when taking into account the whole tissue (Fig. 5.3G), but we could observe it when separating cells of simulated tissues according to their growth rate (Fig. **??**A-B). However, this bias could also be provoked by a boundary effect as slow growing cells were chosen at the periphery of the tissue. In absence of growth rate difference (e.g. isotropic stress field), we could still observe a small bias between the two cell populations (Fig. **??**C-D).

5.4.5 Mechanical perturbations influence division plane orientation

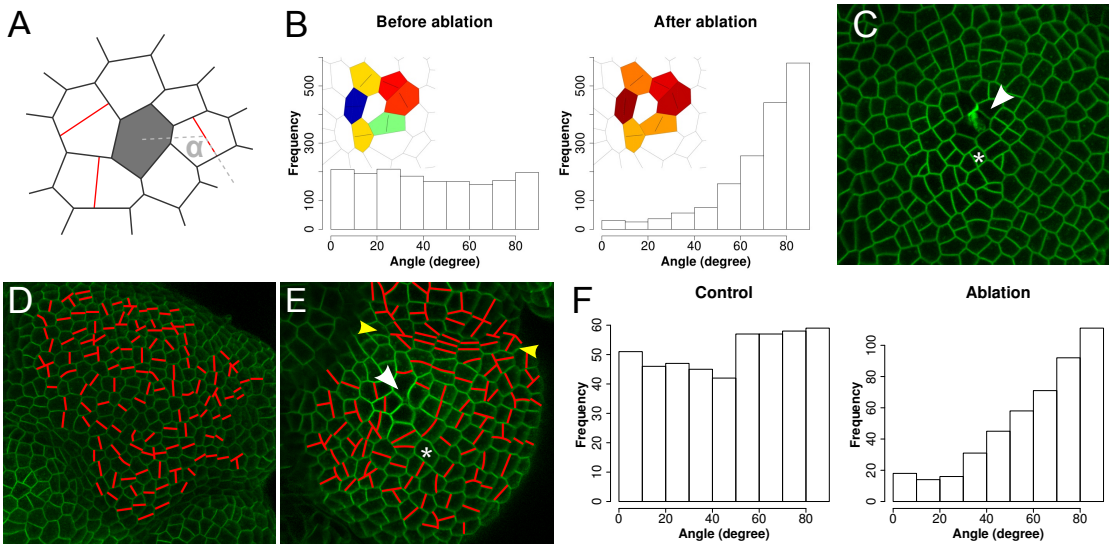

Figure 5.4: **Effects of mechanical perturbation on division plane orientation.** (A) Angle α between principal stress axis (simulated tissues) or new cell wall (real tissues) and radius of the ablation is measured in each cell neighboring the ablation site. (B) Angle α before and after ablation on simulated tissues. Close-up on a simulated tissue shows direction of maximal tension within the cells (black bar). Cells are coloured according to the value of angle α, from blue ($0°$) to red ($90°$). (C) Confocal image of *LTi6B-GFP* (WS-4) dissected SAM 30min after pulsed UV laser ablation. White arrowhead points at ablation site. White asterisk: same cell as in (E). (D-E) New cell walls formed within 48h (red lines) on (D) control and (E) ablated *LTi6B-GFP* (WS-4) dissected SAM. White arrowhead points at ablation site. Yellow arrowheads: boundary. White asterisk: same cell as in (C). (F) Distribution of the angle α in neighbouring cells of 30 ablated meristems. Control: 30 cells of the same meristem are taken as "ablation site" and α is computed in neighbouring cells.

Our analysis so far showed that Besson-Dumais did not predict well all division plane orientations at the SAM, and in particular in the boundary region. Simulations of growing tissues revealed that, when submitted to curvature derived anisotropic stress and following a mechanical division rule, simulated

tissues mimicked both more anisotropic cell aspect ratio and the high proportion of long planes observed in boundary regions of the SAM. An anisotropic modification of the mechanical stress pattern should thus also affect the pattern of cell division plane orientation. We tested this hypothesis using single cell ablation.

FEM simulation of L1 layer under tension predicts that an ablation in the epidermis induces circumferential maximal tensile stress directions in the cells adjacent to the ablated zone [9]. We first ensured that our model was consistent with these previously published results: on different tissues undergoing homogeneous growth and isotropic external stress, a cell was removed from the template and the stress pattern before and after the ablation was analyzed (Fig. 5.4A). As expected, the stress pattern, which was random before ablation, became locally circumferential after the ablation (Fig. 5.4B).

We next performed ablations on real meristems with a pulsed UV laser (Fig. 5.4C) and computed the orientation of division planes in the neighboring cells 48h after ablation (Fig. 5.4D-E). New cell walls formed after the ablation oriented circumferentially around, following the predicted tensile stress pattern (Fig. 5.4F).

5.4.6 Towards a mechanics-based division rule?

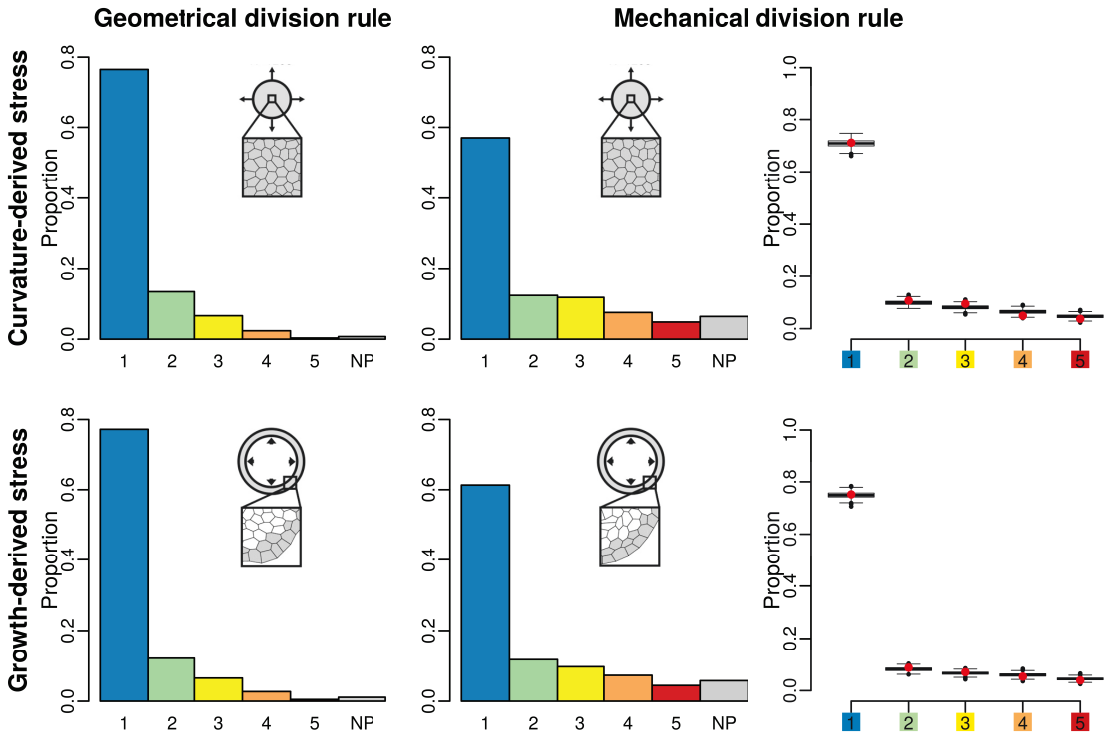

Figure 5.5: **Comparison of two division rules in an isotropic stress field.** Planes classes proportions in the different simulated growing tissue, either submitted to curvature-derived (top) or growth-derived (bottom) isotropic stress and a geometrical (left) or mechanical division rule (right). Comparison of observed planes proportions in simulated tissues (red dots) with fluctuations range obtained by bootstrap among theoretical predictions given by the Besson script (boxplot), in a curvature-derived (top) or growth-derived (bottom) isotropic stress field.

We simulated tissue undergoing an isotropic stress field (same growth on all the tissue and same force in x and y direction), and which thus mimic meristem and primordia regions to test further the application of the mechanical rule. Isotropic growth and curvature derived stress fields produced tissues with similar cell aspect ratio whatever the applied division rule (Fig. 5.10B).

We applied the Besson script on the output of simulated tissues and com-

puted classes of pairwise probabilities as defined previously in §5.4.1 (Fig. 5.5). Again,tissues simulated with the geometrical rule, both in growth- and curvature-derived stress, displayed a majority of short planes, as expected. And tissues simulated with the mechanical division rule displayed a higher proportion of long planes and non predicted planes (NP) than tissues simulated with the geometrical rule.

We applied the same bootstrap approach described in §5.4.2 on tissues simulated with the mechanical division rule to see how far this rule was from Besson-Dumais rule predictions in isotropic cases We found that output of isotropic simulations (Fig. 5.5F-G) are very similar to Besson-Dumais predictions. We did not observed any difference between curvature-derived and growth-derived isotropic stress fields.

5.5 Discussion

Cell division is a defining feature of the shoot meristem, both etymologically (meresis means cell division) and histologically (the meristem organization in layers and zones relates to cell division planes and rates respectively). The shoot apical meristem is therefore a place of choice to investigate how cell division is regulated. Since the end of the XIX^{th} century, geometrical division rules were proposed to explain positioning of new division planes in plants. However none of these rules accounted for all the divisions at the shoot apical meristem (SAM) of *Arabidopsis thaliana* [22]. Recently, one of these rules, the rule of Errera, was re-examined and generalized into a probabilistic rule: the Besson-Dumais rule.

We investigated whether the Besson-Dumais rule can be extended to the dif-

ferent regions of the SAM of *Arabidopsis thaliana* and most particularly to the boundary region. We found that around one quarter of the cells did not choose the shortest plane at the epidermis of the shoot apex. Throughout a bootstrap-like approach we showed that the Besson-Dumais division rule partially accounted for observations, but that long plane were over-represented. A spatialisation of our analysis revealed that the boundary was enriched in long planes. Boundary have a very specific identity compared to other part of the SAM, both genetically and mechanically. We chose a simulation-based approach to simplify the system and tested two alternative division rules hypothesis, either based on geometry or on mechanics, in isotropic or anisotropic mechanical stress field, mimicking either meristem and primordia regions, or boundary regions. We classified planes with the Besson script in order to compare outputs of the simulations with observations made at the SAM. Simulations of a growing tissue following mechanical division rule and submitted to anisotropic stress field displayed a high proportion of long planes, very similar to what had been observed in the boundary. Simulations of a growing tissue following mechanical division rule and submitted to isotropic growth-derived stress field (but not curvature-derived stress field) displayed planes classes proportions similar to those of the meristem region, but not to the primordia. However, the geometrical rule better accounted for planes classes proportions in the primordia. Simulations predicted a local circumferential mechanical stress pattern (e.g. anisotropic) in response to an ablation in a tissue undergoing homogeneous growth and isotropic external stress, consistent with previous simulations of mechanical stress [9]. We performed UV pulsed laser ablations on the meristem region and observed that new cell walls formed after the ablation were oriented circumferentially around. We

performed bootstrap-like approach on the predictions of Besson-Dumais rule on the output of simulations of growing tissue following a mechanical division rule. We found that even if output of isotropic simulations are closer to Besson-Dumais predictions than output of anisotropic simulations, they do not mimic exactly predictions of Besson-Dumais rule. Thus we propose that Besson-Dumais rule is valid in isotropic regions of the SAM, such as the meristem and the primordia, and that anisotropic mechanical stress fields, such as the one in the boundary region or the one provoked by the ablation, may overcome this rule.

Here we pointed at a possible interference between anisotropic mechanical stress field and division plane orientation. Biochemical signals, such as auxin, may as well only interfere with a local geometrical division plane rule, for instance by constraining localization of microtubules. The identification of the synergies and antagonisms between these molecular and mechanical cues will certainly be a fruitful area of research in the future.

5.6 Material and Methods

5.6.1 Plant material and growth conditions

The *LTi6B-GFP* (WS-4) was already described in [15]. Plants were sown on soil, kept at $4°C$ during 48h, then grown in short day conditions (8h light at $19°C$; 16h night at $17°C$) during 4 weeks and transferred 2 to 3 weeks in long days conditions (16h day at $21°C$; 8h night at $19°C$) prior to dissection. Meristems were cut from the stem, dissected the day before imaging and stuck in "Arabidopsis apex culture medium" (2.2g.L^{-1} Duchefa Biochemie MS

basal salt mixture without vitamins, 1% sucrose, 0.8% agarose, pH 5.8), as described in [8]. Medium was supplemented with vitamins (1000X stock solution: 5g Myo-inositol Sigma, 0.05g Nicotinic acid Sigma, 0.05g Pyridoxine hydrochloride Sigma, 0.5g Thiamine hydrochloride Sigma and 0.1g Glycine Sigma in 50mL water) and 200nmol N6-Benzyladenine. Dissected meristems were kept in a phytotron in long days conditions (Sanyo, 16h day at $20°C$; 8h night at $20°C$, synchronized with growth culture chambers).

5.6.2 Imaging

1024x1024 pixels stacks of dissected meristems, with Z slices every $0.5\mu m$, were acquired every 12h during 48h on a Zeiss LSM 700 upright confocal microscope, with a 40x water-dipping lens. Stacks from the kinetics were processed with a C++ script using Level Set Method (Landrein et al., submitted) to detect the 3D surface of the meristem at high resolution. Meshes of these surfaces were then created with MorphoGraphX [12, 3]. Surface geometry of processed stack was extracted with a marching cube algorithm. Initial mesh had a $5\mu m$ resolution. Mesh was smoothed and subdivided until its resolution went below membrane signal thickness (around $0.5\mu m$). Fluorescence signal (1 to $3\mu m$ below the surface) was projected on this mesh. Semi-automatic segmentation was performed using watershed method, allowing delineation of cells.

For each cell, lineage and localization (referred as "primordia", "boundary" and "meristem", e.g. central zone + peripheral zone) were recorded manually for each 12h-snapshots. A boundary is defined as a curved region between an outgrowing primordia and the meristem. Very young boundaries and pri-

mordia are gathered with the "meristem" region. Maps of area and curvature (with a radius of $20\mu m$) for each snapshot, and growth rates and growth directions between each pair of contiguous snapshots, were computed with MorphoGraphX. Each snapshot was exported as a .vtk text file, recording vertices coordinates and associations of vertices to cells. Lineage, localization of cells, growth, curvature and area raw data were saved as separate text files. .vtk and other MorphoGraphX output text files were processed with R [17]to extract various cells indicators (orientation and length of long and short axis, area, growth rate, local direction and intensity of curvature). For each of the snapshots between T12h and T48h, fused daughters cells that came from a division between previous and current snapshot were projected in 2D using a principal component analysis on vertices. Vertices are more spread in x and y, meaning that third dimension always correspond to z. Third dimension explain only a few percent of dispersion of vertices (between 0 and 2.5%, with a mean at 0.15%, see Fig. 5.7C), indicating that local flattening does not deform too much mother cell shape. We kept only the two first dimensions and ordered these vertices clockwise or anti-clockwise. We adapted the input required by Matlab [24] script, written by Sébastien Besson. Predictions given by the rule of Besson and Dumais were obtained with the Matlab [24] script written by Sébastien Besson. This script seeks the shortest plane between each pair of edges dividing the cell into two equal areas and rank these planes according to their length. It then compares observed plane with theoretical predictions and gives the rank of the plane and the probability to observe this plane. Principal Component Analysis were performed with the R package FactoMineR [14].

5.6.3 Ablations

UV laser ablations were performed on an inverted Leica DMI4000 microscope, equipped with a confocal spinning disk head (Yokogawa CSU22), with a 20x dry lens. Stacks from the ablations were processed with MerryProj [2] to obtain a top view 2D projection of the meristems. New cell walls within the two first rank of neighbors around the ablation were identified manually using layers and paths tool of the GNU Image Manipulation Program[23]. Angles between the new plane and the radius of the ablation zone were measured with Fiji angle tool [21]. A non ablated meristem was used as a control. On this meristem, 30 cells were taken as "center of non ablated zone" to compare with the 30 ablations.

5.6.4 Model

We modeled two possible mechanisms driving the positioning of the new wall during a cell division: the new wall can be positioned either to minimize its length or in the direction of highest tension. Then we compared the development of tissues following one or the other mechanism.

We employed a vertex model that allows to compute the mechanics and the geometry of the tissue at the same scale. The model is 2D but 3D information can be incorporated as an external stress.

Mechanics

The cells form a flat polygonal tilling, each polygon being a cell. The mechanics of a single cell C is driven by its anisotropic deformation $M_C - M_C^{(0)}$ where

M_C is the actual shape of the cell and $M_C^{(0)}$ its equilibrium state. The shape tensor is computed as the covariance matrix:

$$M_C = \frac{1}{N_C} \begin{pmatrix} \sum_{i=1}^{N_C}(x_i - x_C)^2 & \sum_{i=1}^{N_C}(x_i - x_C)(y_i - y_C) \\ \sum_{i=1}^{N_C}(x_i - x_C)(y_i - y_C) & \sum_{i=1}^{N_C}(y_i - y_C)^2 \end{pmatrix}$$

where (x_i, y_i) are the coordinates of the cell's vertices, (x_C, y_C) the barycenter of the vertices and N_C the number of vertices. Thus we are able to measure the anisotropy of the cells.

The positions of the vertices is given by the minimization of the mechanical energy of the tissue. Taking into account the elasticity and the turgor pressure, we can define the energy of a single cell:

$$E_C = -pA_C + \frac{\alpha}{2} A_C \frac{\|M_C - M_C^0\|_F^2}{\mathbf{tr^2}\,(M_C^0)}$$

with p the pressure and α the shear modulus of the periclinal wall. The stress tensor of the periclinal wall is then given by the functional derivative of its energy density with respect to its strain:

$$S_C = \frac{\partial \left(\alpha \frac{\|M_C - M_C^0\|_F^2}{\mathbf{tr^2}(M_C^0)} \right)}{\partial \left(\frac{M_C - M_C^0}{\mathbf{tr}(M_C^0)} \right)} = \alpha \frac{M_C - M_C^0}{\mathbf{tr}\,(M_C^0)}$$

where I is the identity matrix.

In a folded boundary, stress is predicted to be anisotropic. Therefore, to take into account the curvature of a real tissue, an external stress is introduced in

the energy of the whole tissue:

$$E_T = \sum_C E_C - A_T \frac{M_T - M_T^0}{\mathbf{tr}\,(M_T^0)} : S_T$$

where A_T is the area of the tissue, M_T its shape, M_T^0 its reference shape and S_T the external stress. The reference shape of the tissue is computed by minimizing the energy without the external term.

As new divisions in the epidermis of the shoot apical meristem are anticlinal (see Fig. 5.6A), we hypothesized that mechanical stress within periclinal cell walls controls the orientation of new anticlinal cell wall. Thus we simulated only mechanics of periclinal cell walls.

Tissue growth

Because of the turgor pressure and the cellular interactions, the cells' shapes are different from their targets when the mechanical energy is minimal. To model the growth as the evolution of the equilibrium state of the cell, the target matrix evolves proportionally to its difference with the actual shape.

$$\frac{dM_C^0}{dt} = a_C \left(M_C - M_C^0\right) \text{ for } C \text{in } 1..N_C$$

where a_C is the growth rate of the cell.

We employed an incremental approach to growth: after minimizing the mechanical energy, the targets evolve according to the differential equation system.

Cellular division

During cell growth, if the area of a cell is higher than the division threshold, the cell is divided according to one of the two following rules:
For the geometrical hypothesis, we mimicked the simplified "shortest path" version of Errera's rule [7] by choosing the division direction $\overrightarrow{n}$ as the one which minimizes the shape of the cell:

$$\overrightarrow{n}, \quad \overrightarrow{n}^t M_C \overrightarrow{n} = \min \left\{ \overrightarrow{u}^t M_C \overrightarrow{u} \right\}_{\|\overrightarrow{u}\|=1}$$

For the mechanical hypothesis, the division direction $\overrightarrow{n}$ is the one which maximizes the stress:

$$\overrightarrow{n}, \quad \overrightarrow{n}^t S_C \overrightarrow{n} = \max \left\{ \overrightarrow{u}^t S_C \overrightarrow{u} \right\}_{\|\overrightarrow{u}\|=1}$$

The cell is divided by a straight line going through its center, which is defined as the barycenter of its vertices.

Properties of the daughter cells

After division, the growth rate of the daughter cells is equated with the growth rate of the mother cell:

$$a_D = a_M$$

The targets of the daughter cells are chosen in order to keep the stress constant over the division:

$$\frac{M_D - M_D^0}{\mathbf{tr}\,(M_D^0)} = \frac{M_M - M_M^0}{\mathbf{tr}\,(M_M^0)}$$

where D stands for a daughter cell and M for the mother cell. One can show that this relation is equivalent to the following definition for the daughter's target:

$$M_D^0 = M_D + \frac{\mathbf{tr}\,(M_D)}{\mathbf{tr}\,(M_M)}\left(M_M^0 - M_M\right)$$

As the two neighbouring cells in the direction of the division get a new vertex, their shape matrix is slightly modified. Therefore, their targets are also adapted to keep the mechanical stress constant. The relation is identical:

$$M_{C'}^0 = M_{C'} + \frac{\mathbf{tr}\,(M_{C'})}{\mathbf{tr}\,(M_C)}\left(M_C^0 - M_C\right)$$

where C and C' stands for the neighbouring cell before and after the division.

Implementation

Model was implemented in a C program. The energy was minimized thanks to the BFGS algorithm, implemented in the NLopt library. The differential equation system was solved thanks to the GNU Scientific Library. Simulation parameters were $p = 0.01$ for the turgor pressure, $\alpha = 2$ for the shear modulus, $S_{T,xx} = 0.03$ and $S_{T,yy} \in \{0.01, 0.03\}$ for the curvature-derived stress, and $a_C \in \{0.3, 1\}$ for the growth rate. Initially the energy was minimized

every $\Delta t = 10^{-2}$, but this time step was reduced proportionally to the number of cells in order to keep a constant temporal resolution on the divisions. Mechanical parameters were set to lead to a strain corresponding to a few percent, as it is observed in real tissues. The external stress was estimated to vary between 1 and 10 times the pressure stress, thus we set the parameters so that the external stress contribution is 75% of the total stress. The tissues are initially 100 cells large and grow up to 250 or 300 cells depending on the simulation. Noise in the initial conditions and in the growth rates allows us to perform each kind of simulation several times. The noise in the initial conditions was tuned so that no vertex cross a cell wall. The noise in the growth rates was a white noise of amplitude 10% that was reset at each time step.

5.7 Supplemental Figures

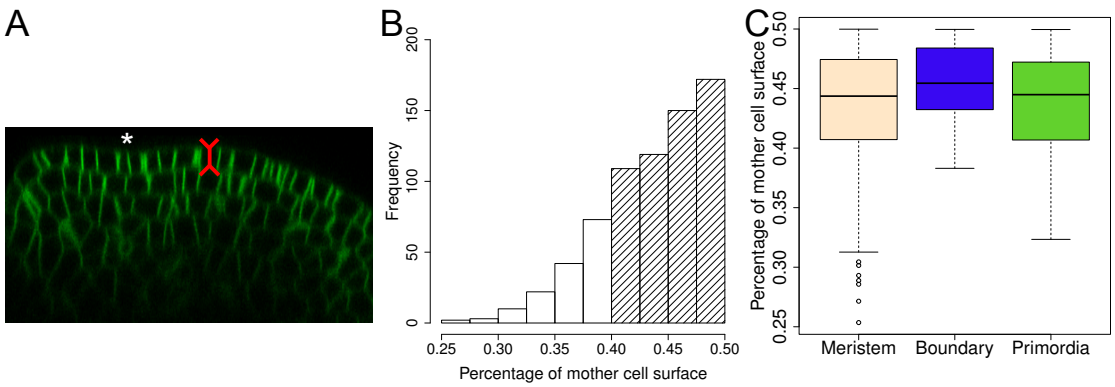

Figure 5.6: **Besson script can be applied on 3D surface of the SAM.** (A) Orthogonal view of a *LTi6B-GFP* (WS4) dissected meristem. L1 has a constant thickness and divisions are anticlinal to the surface. White asterisk: crease of a forming boundary. (B) Distribution of the surface ratio occupied by the smallest of the two daughter cells. N=702 cell divisions. Striped bars: 78% of cells divided almost symmetrically. (C) Distribution of the surface ratio occupied by the smallest of the two daughter cells in the different regions of the SAM. Number of division in the Meristem, Boundary and Primordia region is 544, 26 and 132, respectively.

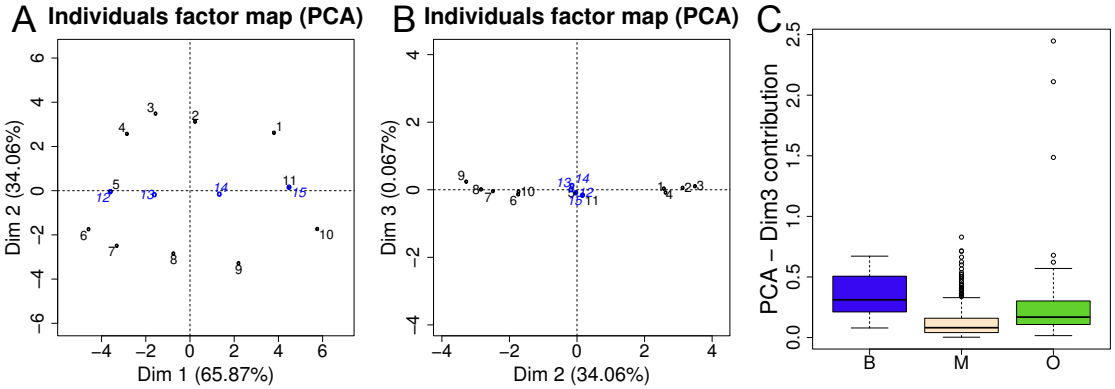

Figure 5.7: **2D projection of two daughter cells.** (A-B) Example of individual factor map of a projected daughters. Cell is the same as in Fig. 5.1D (black asterisk) and E. Vertices of new cell wall are coloured in blue. (A) Plane of dimension one and two. (B) Plane of dimension two and three. (C) Contribution of third dimension in percent in the different regions of the SAM.

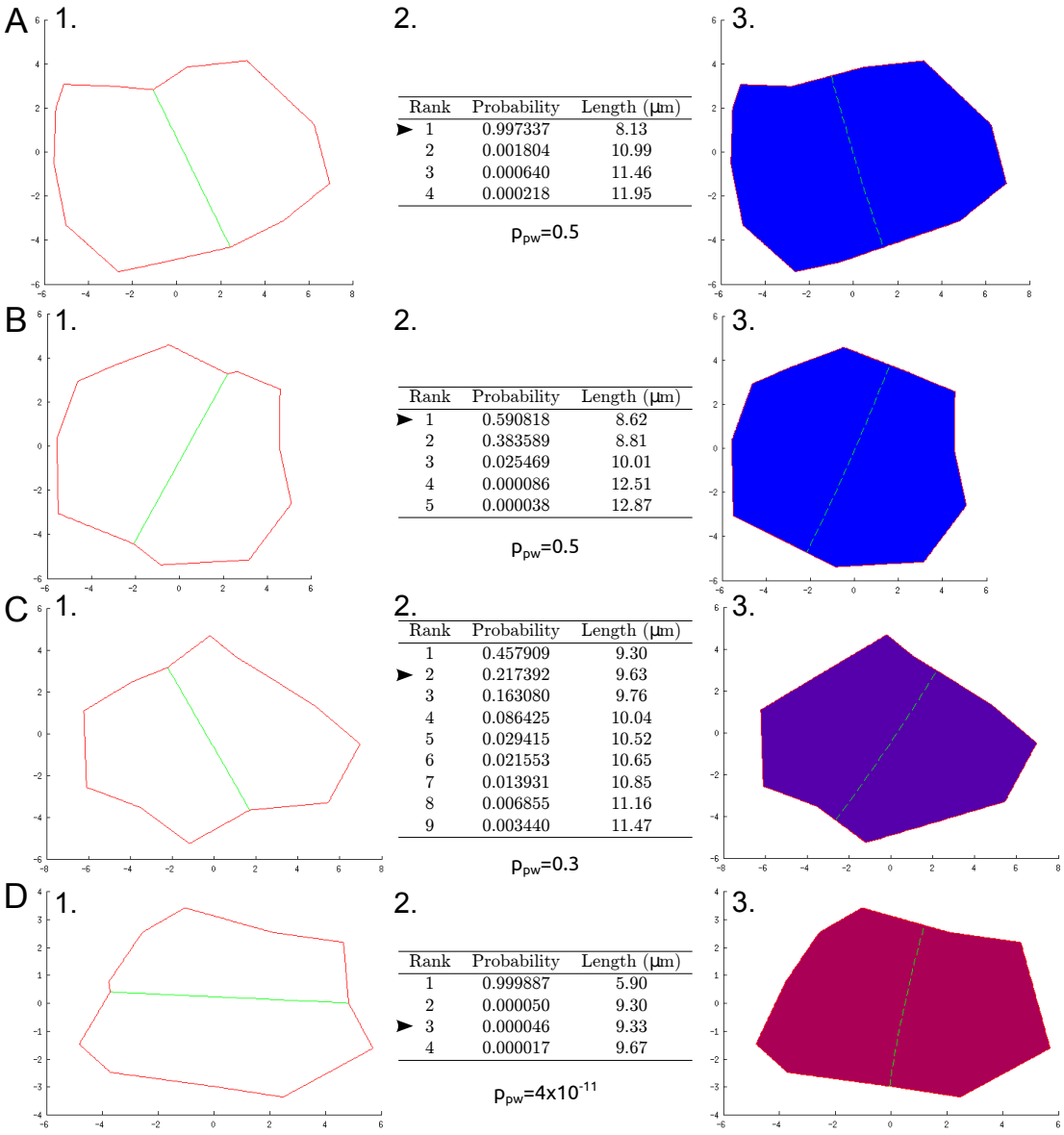

Figure 5.8: **Examples of computations of the Besson script.** (A-D) Different cell shapes, theoretical predictions of the Besson script and their choice of plane. 1. Flattened divided cells. Only main vertices (between the junction of three cells) are kept. New plane are displayed in green. Division occurred in the last 12h. 2. The Besson script computes theoretical predictions and gives match between chosen plane and predictions (arrowhead). 3. The Besson script colors cells according to the rank of theoretical plane matching with the chosen division plane. Blue = shortest plane, purple = second shortest plane, magenta = third shortest plane. Green dashed line indicate position of the shortest theoretical plane. 1. and 3.: X and Y axis are in μm.

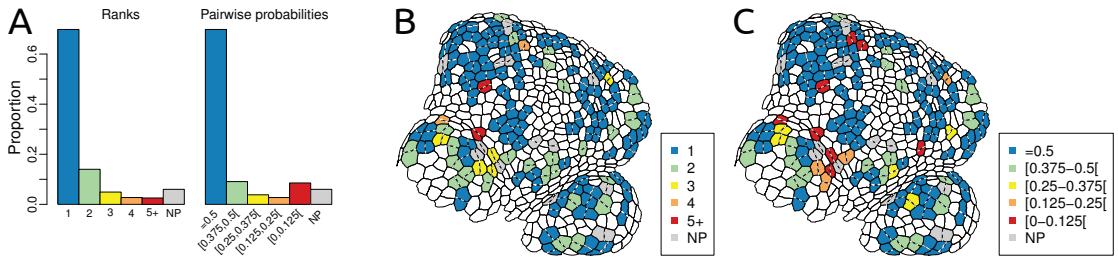

Figure 5.9: **Comparison between ranks and pairwise probabilities.** (A) Proportions of plane ranks and classes of pairwise probabilities (ratio between probability of observed plane and the sum of this probability and the probability of shortest plane). (B) Example of map of planes choices in function of ranks. (C) Example of map (same snapshot as in (B)) of planes choices in function of pairwise probabilities classes.

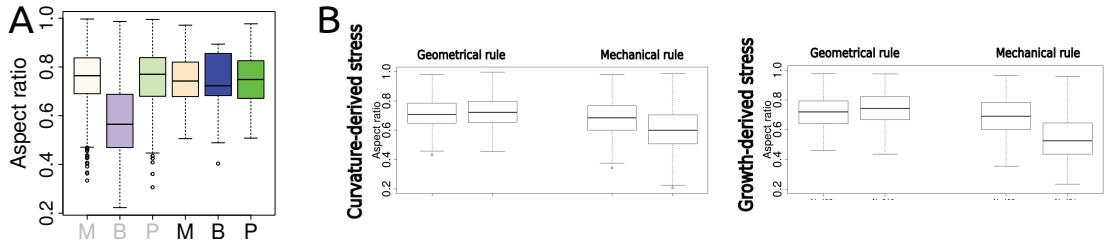

Figure 5.10: **Aspect ratio** (A) Observed aspect ratio of non dividing cells (gray) and symmetrically dividing cells (black) in the different regions of the SAM. M: meristem, B: boundary, P: primordia. Number of cells from left (non dividing meristem cells) to right (dividing primordia cells) is respectively 3220, 527, 1082, 422, 23 and 105. (B) Aspect ratio of cells in simulated tissues, when mechanical stress is derived from curvature or growth. Tissues divided according to either geometrical or mechanical division rule. Mechanical stress field is either isotropic (on the left) or anisotropic (on the right). Number of cells from left (isotropic curvature-derived stress field and geometrical division rule) to right (anisotropic growth-derived stress field and mechanical division rule) is respectively 1208, 1208, 1208, 1008, 402, 310, 408 and 431.

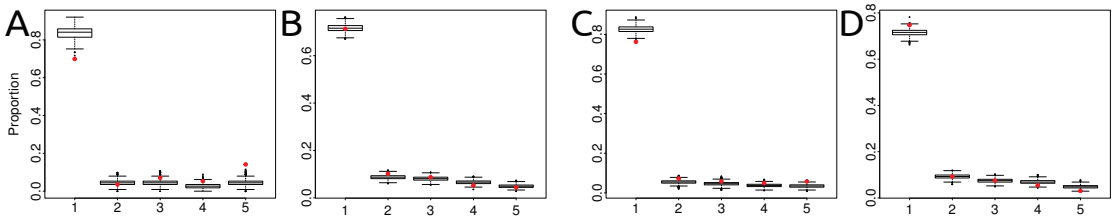

Figure 5.11: **Comparison of planes proportions in simulated tissues with the predictions of the Besson-Dumais rule.** (A-D) Comparison of observed planes proportions in simulated tissues (red dots) with fluctuation range obtained by bootstrap among theoretical predictions given by the Besson script (boxplots), in anisotropic (A-B) or isotropic (C-D) growth-derived stress fields, in function of cell location (A and C: periphery, B and D: center).

References

[1] Mitsuhiro Aida and Masao Tasaka. Genetic control of shoot organ boundaries. *Current Opinion in Plant Biology*, 9(1):72–77, 2006.

[2] P. Barbier de Reuille, I. Bohn-Courseau, C. Godin, and J. Traas. A protocol to analyse cellular dynamics during plant development. *The Plant Journal*, 44(6):1045–1053, 2005.

[3] P. Barbier de Reuille, A.-L. Routier-Kierzkowska, D. Kierzkowski, G. W. Bassel, T. Schüpbach, G. Tauriello, N. Bajpai, S. Strauss, A. Weber, A. Kiss, A. Burian, H. Hofhuis, A. Sapala, M. Lipowczan, M. B. Heimlicher, S. Robinson, E. M. Bayer, K. Basler, P. Koumoutsakos, A. H. K. Roeder, T. Aegerter-Wilmsen, N. Nakayama, M. Tsiantis, A. Hay, D. Kwiatkowska, I. Xenarios, C. Kuhlemeier, and R. S. Smith. MorphoGraphX: A platform for quantifying morphogenesis in 4d. *eLife*, 4, 2015.

[4] S. Besson and J. Dumais. Universal rule for the symmetric division of plant cells. *PNAS*, 108(15):6294–6299, 2011.

[5] S. Besson and J. Dumais. Stochasticity in the symmetric division of plant cells: when the exceptions are the rule. *Frontiers in Plant Science*, 5, 2014.

[6] G. Brunoud, D. M. Wells, M. Oliva, A. Larrieu, V. Mirabet, A. H. Burrow, T. Beeckman, S. Kepinski, J. Traas, M. J. Bennett, and Teva Vernoux. A novel sensor to map auxin response and distribution at high spatio-temporal resolution. *Nature*, 482(7383):103–106, 2012.

[7] L. Errera. Über Zellformen und Seifenblasen. *Botanisches Centralblatt*, 34:395–398, 1888.

[8] O. Hamant, P. Das, and A. Burian. Time-Lapse Imaging of Developing Meristems Using Confocal Laser Scanning Microscope. In V. Žárský and F. Cvrčková, editors, *Plant Cell Morphogenesis*, volume 1080, pages 111–119. Humana Press, Totowa, NJ, 2014.

[9] O. Hamant, M. G. Heisler, H. Jönsson, P. Krupinski, M. Uyttewaal, P. Bokov, F. Corson, P. Sahlin, A. Boudaoud, E. M. Meyerowitz, Y. Couder, and J. Traas. Developmental Patterning by Mechanical Signals in Arabidopsis. *Science*, 322(5908):1650–1655, 2008.

[10] M. G. Heisler, C. Ohno, P. Das, P. Sieber, G. V. Reddy, J. A. Long, and E. M. Meyerowitz. Patterns of Auxin Transport and Gene Expression during Primordium Development Revealed by Live Imaging of the Arabidopsis Inflorescence Meristem. *Current Biology*, 15(21):1899–1911, 2005.

[11] W. Hofmeister. Zusatze und berichtigungen zu den 1851 veröffentlichen untersuchungen der entwicklung höherer kryptogamen. *Jahrbucher fur Wissenschaft und Botanik*, 3:259–293, 1863.

[12] D. Kierzkowski, N. Nakayama, A. L. Routier-Kierzkowska, A. Weber, E. Bayer, M. Schorderet, D. Reinhardt, C. Kuhlemeier, and R. S. Smith. Elastic domains regulate growth and organogenesis in the plant shoot apical meristem. *Science*, 335(6072):1096, 2012.

[13] D. Kwiatkowska and J. Dumais. Growth and morphogenesis at the vegetative shoot apex of Anagallis arvensis L. *Journal of experimental botany*, 54(387):1585–1595, 2003.

[14] S. Lê, J. Josse, and F. Husson. FactoMineR: an R package for multivariate analysis. *Journal of statistical software*, 25(1):1–18, 2008.

[15] J. Marc, C. L. Granger, J. Brincat, D. D. Fisher, T. Kao, A. G. McCubbin, and R. J. Cyr. A GFP–MAP4 reporter gene for visualizing cortical microtubule rearrangements in living epidermal cells. *The Plant Cell*, 10(11):1927–1939, 1998.

[16] S. Müller, S. Han, and L. G. Smith. Two Kinesins Are Involved in the Spatial Control of Cytokinesis in Arabidopsis thaliana. *Current biology*, 16(9):888–894, 2006.

[17] R Core Team. R: A Language and Environment for Statistical Computing, 2015.

[18] M. I. Rast and R. Simon. The meristem-to-organ boundary: more than an extremity of anything. *Current opinion in Genetics & Development*, 18(4):287–294, 2008.

[19] J. Sachs. Uber die Anordnung der Zellen in jungsten Pflanzentheilen. *Arbeiten des Botanisches Institut Wurzburg*, 2:46–104, 1878.

[20] P. Sahlin and H. Jönsson. A Modeling Study on How Cell Division Affects Properties of Epithelial Tissues Under Isotropic Growth. *PLoS ONE*, 5(7):e11750, 2010.

[21] J. Schindelin, I. Arganda-Carreras, E. Frise, V. Kaynig, M. Longair, T. Pietzsch, S. Preibisch, C. Rueden, S. Saalfeld, Benjamin Schmid, J.-Y. Tinevez, D. J. White, V. Hartenstein, K. Eliceiri, P. Tomancak, and A. Cardona. Fiji: an open-source platform for biological-image analysis. *Nature Methods*, 9(7):676–682, 2012.

[22] B. E. Shapiro, C. Tobin, E. Mjolsness, and E. M. Meyerowitz. Analysis of cell division patterns in the Arabidopsis shoot apical meristem. *Proceedings of the National Academy of Sciences*, 112(15):4815–4820, 2015.

[23] The GIMP team. GNU Image Manipulation Program, 2012.

[24] The MathWorks, Inc. Matlab, 2013.

[25] J. Traas, C. Bellini, P. Nacry, Jocelyne Kronenberger, D. Bouchez, and M. Caboche. Normal differentiation patterns in plants lacking microtubular preprophase bands. *Nature*, 375(6533):676–677, 1995.

[26] M. Uyttewaal, A. Burian, K. Alim, B. Landrein, D. Borowska-Wykret, A. Dedieu, A. Peaucelle, M. Ludynia, J. Traas, A. Boudaoud, D. Kwiatkowska, and O. Hamant. Mechanical Stress Acts via Katanin to Amplify Differences in Growth Rate between Adjacent Cells in Arabidopsis. *Cell*, 149(2):439–451, 2012.

[27] K. L. Walker, S. Müller, D. Moss, D. W. Ehrhardt, and L. G. Smith. Arabidopsis TANGLED Identifies the Division Plane throughout Mitosis and Cytokinesis. *Current Biology*, 17(21):1827–1836, 2007.

[28] S. Yoshida, P. Barbier de Reuille, B. Lane, G. W. Bassel, P. Prusinkiewicz, R. S. Smith, and D. Weijers. Genetic Control of Plant Development by Overriding a Geometric Division Rule. *Developmental Cell*, 29(1):75–87, 2014.

Chapter 6

Conclusion and perspectives

The role of mechanics in morphogenesis has been recognized about a century ago, but a systematic investigation of its interaction with biochemical signals and growth is much more recent. In this thesis, we investigated some examples of coupling between growth and mechanics in the context of plants and yeasts. These organisms are well-suited for mechanical studies because of the tremendous forces involved in their development, under the action of their high internal pressure on their very stiff cell wall.

The first work we presented here showed that the establishment and stabilization of polarity in fission yeast spores relies on two feedback loops interfering with each other. In the phase of germination, growth increases the mechanical stress in the protective sheel of the spore, that in turn inhibits growth. This inhibition, via the positive feedback between growth and polarity, destabilize the polarisome that desassembles and reassembles at a different location. The outer spore wall breaks when the stress acting on it is too large, thus releasing its inhibition, and allowing to the second loop to stabilize the axis of growth. This work raises the question of the biochemical

nature of this second feedback. Mechanism of stretch-activation, such as the one found in the oscillatory growth of pollen tubes, could be involved [8]. It has also been proved that vesicle delivery can have a destabilizing effect on polarity through dilution, in which case surface expansion would limit this phenomenon [5].

An interesting extension of this work would be to investigate whether the feedback considered here could also explain other experimental observations, in particular mutants with curved shapes and heterogeneous thickness [unpublished data]. The preliminary results in this direction were promising. The concept of a coupling between growth and polarity could also be relevant in a larger context, especially in other tip growing fungi, such as hyphae. In pollen grains, the extension of the pollen tubes takes place on a weak spot of grain wall. Thus, mechanics has an important role on the outgrowth of the tube and combining modeling and mechanical perturbations of the pollen grain could be an interesting project, not investigated so far.

In the second work, we studied another model of pattern mechanically stabilized. In the shoot apex, the pattern of auxin prefiguring the arrangement of the organs, is due to a chemomechanical feedback. Auxin soften the cells, which bear less mechanical tension. In turn, mechanics enhance the auxin efflux in the neighbouring cells, thus creating the pattern. We used this model to determine whether transport is regulated by the strain or the stress of the cell wall. The simulation of previously published experiments support the hypothesis of strain-sensing. Additionally, the strain feedback is less sensitive to noise or to variations in its parameters. This strain-sensing could be achieved by modification of the balance between endo- and exocytosis upon stretching [12].

A feature of this model is that the wavelengh does not seem to be as well defined as predicted by previous models using mechanisms of auxin feedback on its transporters [9]. The first question I would study to go further is whether growth and cell divisions can have an impact on the regularity of the patterns by the successive appearance of the peaks at the right positions [6]. An important question in the context of auxin transport is to determine whether phyllotactic and veination patterns can be explained by a common mechanism [10]. Some models, relying on flux-sensing, assuming that cells are able to measure auxin flux and orient their transporters accordingly, can produce convincing patterns but require many other assumptions [11]. Moreover the evidence is strong that mechanics is involved [3, 7, 1]. The mechanical properties of the external and internal tissues being different, in terms of stiffness and deformation [4], mechanics could explain the different behavior of the transporters. Measuring and modeling the precise mechanics of the shoot apex in three dimensions would give some major insights but is a challenging project.

Finally, in the last chapter of this manuscript, we investigated the impact of mechanical stress on the cell divisions, an inevitable consequence of growth. We showed that at the boundary between the meristem and an organ primordium, the cell divisions do not follow the predictive rule that rely on the geometry of the cells. This boundary is characterized by a higher tensile stress in its direction, resulting both from its anisotropic curvature and its lower growth rate. A mechanical model that incorporates this curvature- and growth-derived stresses is able to reproduce this disagreement by assuming that the divisions are oriented by the maximal mechanical tension rather than the short axis of the cell. Upon cell ablations, the reorientation of stress

in the simulations and of the divisions in real tissues confrim our hypothesis. Microtubules are able to orient along the directions of mechanical stress [2] and are fundamental actors of the division machinery. Consequently they could be involved in this phenomenon.

Intuitively, these anisotropic divisions in the boundary seem to increase the mechanical anisotropy of the tissue, by making new walls in a preferential direction. Thus it would generate another layer of control over the shaping of the shoot apex, jointly with the cellulose anisotropic deposition and auxin patterns. To study this hypothesis, I would simulate the appearance of a boundary between two fast-growing groups of cells and observe the dynamics of the crease formation depending on the rule choosen for the cell divisions. But this project would require 3D simulations, a major change with respect to the current model. Experiments could be performed by looking at the dynamics of the boundary formation in mutants whose divisions orientation is noisier. However it could be difficult to find mutants with defects only in the cell division orientation.

References

[1] Siobhan A. Braybrook and Alexis Peaucelle. Mechano-Chemical Aspects of Organ Formation in Arabidopsis thaliana: The Relationship between Auxin and Pectin. *PLoS ONE*, 8(3):e57813, March 2013.

[2] Olivier Hamant, Marcus G. Heisler, Henrik Jönsson, Pawel Krupinski, Magalie Uyttewaal, Plamen Bokov, Francis Corson, Patrik Sahlin, Arezki Boudaoud, Elliot M. Meyerowitz, and others. Developmental patterning by mechanical signals in Arabidopsis. *science*, 322(5908):1650–1655, 2008.

[3] Marcus G. Heisler, Olivier Hamant, Pawel Krupinski, Magalie Uyttewaal, Carolyn Ohno, Henrik Jönsson, Jan Traas, and Elliot M. Meyerowitz. Alignment between PIN1 Polarity and Microtubule Orientation in the Shoot Apical Meristem Reveals a Tight Coupling between Morphogenesis and Auxin Transport. *PLoS Biology*, 8(10):e1000516, October 2010.

[4] U. Kutschera and K.J. Niklas. The epidermal-growth-control theory of stem elongation: An old and a new perspective. *Journal of Plant Physiology*, 164(11):1395–1409, November 2007.

[5] Anita T. Layton, Natasha S. Savage, Audrey S. Howell, Susheela Y. Carroll, David G. Drubin, and Daniel J. Lew. Modeling Vesicle Traffic Reveals Unexpected Consequences for Cdc42p-Mediated Polarity Establishment. *Current Biology*, 21(3):184–194, February 2011.

[6] P. K. Maini, T. E. Woolley, R. E. Baker, E. A. Gaffney, and S. S. Lee. Turing's model for biological pattern formation and the robustness problem. *Interface Focus*, 2(4):487–496, August 2012.

[7] Naomi Nakayama, Richard S. Smith, Therese Mandel, Sarah Robinson, Seisuke Kimura, Arezki Boudaoud, and Cris Kuhlemeier. Mechanical Regulation of Auxin-Mediated Growth. *Current Biology*, 22(16):1468–1476, August 2012.

[8] Enrique R. Rojas, Scott Hotton, and Jacques Dumais. Chemically Mediated Mechanical Expansion of the Pollen Tube Cell Wall. *Biophysical Journal*, 101(8):1844–1853, October 2011.

[9] Patrik Sahlin, Bo Söderberg, and Henrik Jönsson. Regulated transport as a mechanism for pattern generation: Capabilities for phyllotaxis and beyond. *Journal of Theoretical Biology*, 258(1):60–70, May 2009.

[10] K. van Berkel, R. J. de Boer, B. Scheres, and K. ten Tusscher. Polar auxin transport: models and mechanisms. *Development*, 140(11):2253–2268, June 2013.

[11] Michael Luke Walker, Etienne Farcot, Jan Traas, and Christophe Godin. The Flux-Based PIN Allocation Mechanism Can Generate Either Canalyzed or Diffuse Distribution Patterns Depending on Geometry and Boundary Conditions. *PLoS ONE*, 8(1):e54802, January 2013.

[12] Marta Zwiewka, Tomasz Nodzyński, Stéphanie Robert, Steffen Vanneste, and Jiří Friml. Osmotic Stress Modulates the Balance between Exocytosis and Clathrin-Mediated Endocytosis in Arabidopsis thaliana. *Molecular Plant*, 8(8):1175–1187, August 2015.